Feasibility of Ultrasonic Phased Array Inspection on as-Forged Components

by

Jorge Franklin MANSUR RODRIGUES FILHO

MANUSCRIPT-BASED THESIS PRESENTED TO ÉCOLE DE TECHNOLOGIE SUPÉRIEURE IN PARTIAL FULFILLMENT FOR THE DEGREE OF DOCTOR OF PHILOSOPHY
Ph.D.

MONTREAL, DECEMBER 5TH, 2022

ÉCOLE DE TECHNOLOGIE SUPÉRIEURE
UNIVERSITÉ DU QUÉBEC

© Copyright 2022 reserved by Jorge Franklin Mansur Rodrigues Filho

© Copyright reserved

It is forbidden to reproduce, save or share the content of this document either in whole or in parts. The reader who wishes to print or save this document on any media must first get the permission of the author.

BOARD OF EXAMINERS

THIS THESIS HAS BEEN EVALUATED

BY THE FOLLOWING BOARD OF EXAMINERS

Mr. Pierre Bélanger, Thesis Supervisor
Department of Mechanical Engineering, École de technologie supérieure

Mr. François Blanchard, President of the Board of Examiners
Department of Electrical Engineering, École de technologie supérieure

Mr. Ricardo Zednik, Member of the jury
Department of Mechanical Engineering, École de technologie supérieure

Mr. Nicolas Quaegebeur, External Evaluator
Université de Sherbrooke

THIS THESIS WAS PRESENTED AND DEFENDED

IN THE PRESENCE OF A BOARD OF EXAMINERS AND PUBLIC

ON NOVEMBER 30TH, 2022

AT ÉCOLE DE TECHNOLOGIE SUPÉRIEURE

ACKNOWLEDGMENT

It’s been a long journey. Sometimes it feels like we arrived just yesterday, and finishing the Ph.D. was miles away. But four years have passed, and we finally reached the conclusion. And even though the solitude is so present in the doctoral studies, I’ve learned that big achievements are only possible thanks to other people: the scientists, our teachers, and mainly our loved ones. These are my thanks to all of you.

First, I thank my teachers back in Brazil that taught me how we can make a better world through education. Your struggles to make our education better with little resources has paid off. And here in Canada, for making this work possible, my many thanks to my supervisor Professor Pierre for all opportunities and all his support throughout these years.

A huge thanks to my friends, you made life softer and funnier every day. Thanks Lucas and Bhupesh for being true comrades in the lab, I’m going to miss our nice talks and bad coffee at Tim’s. My friends back in Brazil, Daniel, Guimaroto, Japa, Léo, Ralph, Salgado, Vinicim, obrigado a todos por estarem sempre por perto com as calls, as jogatinas e as resenhas.

À minha família, obrigado por estarem comigo. Aos meus avós que sei que estão muito orgulhosos, pois sempre me ensinaram a ser trabalhador e honesto. Obrigado mãe, por me ensinar o valor dos estudos e por seu carinho e proteção. Aos meus irmãos, por serem companheiros e amigos, me apoiando sempre, vocês são meus exemplos, amo vocês.

Bel, meu amor, muito obrigado por estar ao meu lado. Você tornou esse Ph.D. possível, essa conquista é nossa. Desde o dia em que apoiou nossa vinda, até os seus sacrifícios, trabalho duro, e seguradas nas pontas. O doutorado mostrou que há uma mulher muito forte, parceira e determinada dividindo a vida comigo. Isso me enche de orgulho e me dá muita força. Aprendo muito com você todos os dias. Enfim, para mim o maior fruto não é o título e sim a vida que ganhamos, cheia de amor, carinho e risadas. Fizemos o tempo passar mais rápido e essa jornada ser incrível.

Faisabilité de L'inspection Ultrasonique Multi-éléments sur des Composants Comme Forgés

Jorge Franklin MANSUR RODRIGUES FILHO

RESUME

Dans le cadre de l'inspection par ultrasons de composants de moteurs d'avions, ce travail étudie la faisabilité d'effectuer des contrôles non destructifs par ultrasons sur des pièces forgées. En partenariat avec Pratt and Whitney Canada (P&WC), une étude a été proposée sur les cas de ces pièces que nécessitant un niveau d'inspection extrêmement élevée. Par conséquent, le défi de l'inspection par ultrasons de pièces aux géométries complexes a été étudié et développé dans trois travaux. Tout d'abord, la fiabilité de la *total focusing method* (TFM) a été étudiée en termes de distance de sonde quand appliquée aux pièces avec des profils concaves et convexes. Des artefacts se sont produits à certaines combinaisons profil-position de sonde, provoquant la réduction de l'amplitude et de la résolution de l'image. Ainsi, une méthode d'optimisation de la position de sonde (PSOM) a été introduite pour atténuer ces effets. En conséquence, des améliorations considérables de la TFM ont été démontrées à la position optimale. L'image TFM d'un spécimen convexe démontrée un indicateur *array performance indicator* (API) amélioré et le *signal-to-artifact ratio* (SAR) a gagné jusqu'à 13 dB. Enfin, l'image sous une surface concave a gagné jusqu'à 33 dB en SAR. La deuxième étude visait à optimiser l'imagerie des défauts sous les pièces à surfaces concaves. Une stratégie de *beamforming* a été proposée pour atténuer le problème de mauvaise pénétration des ultrasons. Dans cette méthode, la réfraction était compensée en focalisant le faisceau ultrasonore sur des points à la surface de l'échantillon. En utilisant moins de transmissions, le calcul du faisceau a montré un gain de 12 dB par transmission, et l'imagerie d'un trou de 1 mm a présenté une amélioration d'environ 11 dB du *signal-to-noise ratio*. Le troisième article présente un nouveau TFM global (gTFM) pour scanner un spécimen complexe représentant une maquette de forgeage de disque aérospatial. Ce spécimen contenait 30 trous percés latéralement comme cibles de sensibilité et une géométrie de profil composée de multiples surfaces concaves et convexes. Cette étude a combiné les deux travaux précédents à travers un modèle numérique de l'inspection afin d'optimiser le *scan plan*. De plus, la sonde multiélément à ultrasons a été balayée autour de l'échantillon à l'aide d'un bras robotisé, et toutes les acquisitions ont été combinées pour générer les images TFM globales. La comparaison de différents plans de balayage a montré que le plan optimal, avec la position de la sonde adaptée au profil de surface, entraînait la meilleure image des SDH. Cela représente une augmentation de 40 % du rapport contraste/bruit moyen (CNR), une réduction de 70 % de l'erreur de position (seulement 0,1 mm) et une réduction de 33 % d'API. La couverture d'inspection était efficace, avec seulement sept positions de sonde nécessaires pour représenter la section transversale complète de l'échantillon. Enfin, les résultats de la recherche sur les pièces forgées de P&WC sont présentés. L'alliage de Ni a été caractérisé et évalué à l'aide de tests par ultrasons standard et multiéléments. Ensuite, une inspection d'alésage à l'aide de TFM a été proposée et validée comme alternative pour augmenter la sensibilité de l'inspection. Un défaut causé lors de la fabrication a été évalué et dimensionné à l'aide d'un CT-scan, d'un test par ultrasons standard et d'un TFM. Ce dernier a présenté les meilleurs résultats avec une erreur de taille inférieure à 10 %. Pour compléter l'étude, une expérience de comparaison de sensibilité a été conçue pour P&WC.

Mots-clés: Essais ultrasonores multiéléments, TFM, FMC, pièces complexes, robotisation

Feasibility of Ultrasonic Phased Array Inspection on as Forged Components

Jorge Franklin MANSUR RODRIGUES FILHO

ABSTRACT

In the context of ultrasonic inspection of aircraft engine components, this work investigates the feasibility of performing ultrasonic non-destructive testing on as-forged parts. In partnership with Pratt and Whitney Canada (P&WC), a case study on fan disk forgings that require an extremely high inspection standard was proposed. Therefore, the challenging ultrasonic inspection of parts with complex geometries was researched and developed in three complementary works. First, the reliability of the total focusing method (TFM) applied to specimens with concave and convex profiles was studied in terms of the probe standoff. Artifacts with high amplitude and resolution loss occurred at some profile-standoff combinations. So, a probe standoff optimization method (PSOM) was introduced to mitigate such effects. As a result, considerable TFM improvements were demonstrated at the optimal standoff. The TFM image of a convex specimen had its array performance indicator (API) improved and the signal-to-artifact ratio (SAR) gained up to 13 dB. Lastly, the image under a concave surface gained up to 33 dB in signal-to-artifact ratio. The second study aimed at optimizing the imaging of defects below parts with concave surfaces. A beamforming strategy was proposed to mitigate the poor ultrasound penetration problem. In this method, the refraction was compensated by focusing the ultrasonic beam on points on the specimen's surface. Using fewer transmissions, the beam computation showed a gain of 12 dB per transmission, and the imaging of a 1 mm side drilled hole presented an improvement of approximately 11 dB in signal-to-noise ratio. The third article presents a novel global TFM (gTFM) to scan a complex specimen representing an aerospace disk forging mock-up. This specimen contained 30 side-drilled holes as sensitivity targets and a profile geometry comprised of multiple concave and convex surfaces. This study combined both previous works through a digital twin of the inspection to optimize the scan plan. Moreover, the ultrasonic phased array probe was scanned around the specimen using a robotic arm, and all acquisitions were combined to generate the global TFM images. The comparison of different scan plans showed that the optimal one, with the probe position adapted to the surface profile, resulted in the sharpest image of the SDHs. This represents a 40% increase in the mean contrast-to-noise ratio (CNR), a 70% reduction in position error (only 0.1mm), and a 33% reduction in the array performance indicator (API). The inspection coverage was efficient, with only seven probe positions needed to depict the complete cross-section of the specimen. Finally, the results of the research on P&WC forgings are presented. The Ni-alloy was characterized and assessed using standard and phased array ultrasonic testing. Then a bore inspection using TFM was proposed and validated as an alternative to increase the inspection sensitivity. A flaw caused in manufacturing was evaluated and sized using a CT scan, standard ultrasonic testing, and TFM. The latter presented the best results with a size error below 10%. To complete the study, an experiment for comparison of sensitivity was designed for P&WC.

Keywords: Phased array ultrasonic testing, TFM, FMC, complex specimens, robotization

TABLE OF CONTENTS

Page

INTRODUCTION 1

CHAPTER 1 RESEARCH BACKGROUND 5
1.1 Industrial motivation 5
1.2 State-of-the-art 9
  1.2.1 Ultrasonic testing 9
  1.2.2 Physics of Ultrasonic Testing 10
  1.2.3 Phased array ultrasonic testing 13
  1.2.4 Phased array ultrasonic testing on components with non-flat surfaces 16
  1.2.5 Full matrix capture (FMC) 18
  1.2.6 Total focusing method (TFM) 19
1.3 Research scope and introduction to articles 22

CHAPTER 2 PROBE STANDOFF OPTIMIZATION METHOD FOR PHASED ARRAY ULTRASONIC TFM IMAGING OF CURVED PARTS 25
2.1 Abstract 25
2.2 Introduction 26
2.3 Materials and Methods 28
  2.3.1 Total Focusing Method Imaging 28
  2.3.2 Probe Standoff Optimization Method 30
  2.3.3 Experimental Analysis 34
  2.3.4 Data Post-Processing and Metrics 37
2.4 PSOM and Experimental Results 39
2.5 Discussion 46
2.6 Conclusion 48

CHAPTER 3 A BEAMFORMING STRATEGY TO IMPROVE THE ULTRASONIC PHASED ARRAY INSPECTION BELOW CONCAVE SURFACES 51
3.1 Abstract 51
3.2 Introduction 52
3.3 Proposed beamforming strategy 52
3.4 Experimental setup and results 53
3.5 Conclusion 55

CHAPTER 4 GLOBAL TOTAL FOCUSING METHOD THROUGH DIGITAL TWIN AND ROBOTIC AUTOMATION FOR ULTRASONIC PHASED ARRAY INSPECTION OF COMPLEX COMPONENTS 57
4.1 Abstract 57

4.2 Introduction 58
4.3 Materials and methods 60
  4.3.1 Global Total Focusing Method (gTFM) 60
  4.3.2 Complex specimen gTFM optimization 62
  4.3.3 Case study: the specimen design.. 64
  4.3.4 Experimental setup.. 65
  4.3.5 Complex specimen scan plan comparison 68
  4.3.6 Analysis of gTFM imaging performance.. 69
4.4 Results and discussion 70
  4.4.1 gTFM renderings 70
  4.4.2 Flat specimen gTFM rendering.. 70
  4.4.3 Complex specimen gTFM rendering – strategy 1.................................... 72
  4.4.4 Complex specimen gTFM rendering – strategy 2.................................... 72
  4.4.5 Complex specimen gTFM rendering – strategy 3.................................... 73
  4.4.6 Complex specimen gTFM rendering – strategy 4.................................... 73
  4.4.7 Complex specimen gTFM rendering – strategy 5.................................... 74
  4.4.8 Complex specimen gTFM imaging quality 76
4.5 Conclusion 81
4.6 Acknowledgment 82

CHAPTER 5 INDUSTRIAL APPLICATION 83
5.1 Case study – PAUT of aerospace turbine disk forgings 83
  5.1.1 Forging characterization 83
  5.1.2 UT and PAUT sensitivity.. 86
  5.1.3 PAUT bore inspection.. 90
  5.1.4 Real flaw evaluation 93
  5.1.5 Final feasibility experiment 99

CONCLUSION 103

RECOMMENDATIONS 107

LIST OF BIBLIOGRAPHICAL REFERENCES..109

LIST OF TABLES

Page

Table 2-1 Specimen surface curvature parameters and probe standoffs. 35

Table 2-2 Probe and material parameters. 36

Table 4-1 SDH index and coordinates on stainless steel forging section 65

Table 4-2 Probe position indexes used in the experiments – number of standoffs and range 67

Table 4-3 Scan plans analyzed - Probe position and characteristics 69

Table 4-4 Inspection time from experimental results using different approaches 79

Table 5-1 Ni-alloy forged specimens' physical properties 84

Table 5-2 Geometric parameters of P&WC calibration blocks 86

LIST OF FIGURES

Page

Figure 1-1 The P&WC turbine disk forging manufacturing and NDE process schematic...6

Figure 1-2 P&WC Waspalloy sample micrography showing equiaxed microstructure and the presence of a crack 6

Figure 1-3 The ultrasonic testing of the 5M disk forging – calibration process and immersion UT scan plan. 7

Figure 1-4 (a) Ultrasonic testing scheme (Reproduced from (Schmerr, 2015)). (b) Ultrasonic testing A-scan example...10

Figure 1-5 (a) Longitudinal and shear waves particle motion pattern. (b) Refraction, transmission, and reflection of bulk waves at the solid-liquid interface. (Adapted from: (Cheeke, 2012))........11

Figure 1-6 Schematics of the ultrasonic beam main characteristics (OLYMPUS NDT, 2004)...13

Figure 1-7 The PAUT's ability to focus and steer the wavefront using delays. (Adapted from OLYMPUS NDT, 2004) 14

Figure 1-8 The PAUT probe design dimensions. $W_{passive}$ – Passive aperture; n – number of elements; e – element width; g – element spacing or kerf; p – pitch. (Adapted from OLYMPUS NDT, 2004) 15

Figure 1-9 Examples of possible element arrays for PAUT probes. (Adapted from OLYMPUS NDT, 2004) 16

Figure 1-10 Full matrix capture representation. Adapted from (SUTCLIFFE M., 2012) 18

Figure 1-11 Schematic of the total focusing method (TFM)..20

Figure 1-12 Example of TFM applied to a specimen with a curved surface. (Adapted from: (M. Sutcliffe et al., 2013))...21

Figure 1-13 Imaging of FBH under different curved surface radii; (Adapted from:(Brown et al., 2017)) 22

Figure 2-1 Schematic of the total focusing method applied to an immersed part with s(x) top surface profile. The waves travel from the emitter e to a pixel and then to the receiver r through the paths which respect the Fermat's principle. The same applies for a point reflector T(x,z), where paths d have different refraction angles for each combination of e and r. 28

Figure 2-2 PSF example. The power represents the image intensity at a given point. *PSF(x)* is defined at *z*, where the power is maximum. Main lobe width and side lobe levels are found as illustrated. 32

Figure 2-3 Flowchart of the Probe Standoff Optimization Method algorithm. A *PSF(x)* calculation and discrimination are conducted to find the standoff with the best trade-off between the lateral resolution and the artifact level. 33

Figure 2-4 Schematic of the sinusoidal concave and convex specimens inspected by immersion phased array ultrasonic testing. The probe is centered relative to the surface. Three SDH are positioned inside the specimens and are analyzed by the TFM sub-image shown. 34

Figure 2-5 Schematic of the experimental setup used to validate the optimization calculations. The setup was assembled using 3D-printed plastic holders. 37

Figure 2-6 PSF(x) calculated for a target positioned 10 mm deep inside the parts: (**a**) Flat specimen F0 at two probe standoffs *h* = 20 and 130 mm; (**b**) Convex specimen Cx15 at two probe standoffs *h* = 20 and 130 mm; (**c**) Concave specimen Cc15 at two probe standoffs *h* = 40 and 100 mm. 40

Figure 2-7 PSOM and experimental results from the SDH at 10 mm depth inside each specimen: (**a**) SLL obtained from *PSF(x)* at each standoff *h*; (**b**) MLW versus *h*; (**c**) TFM images at different probe standoffs *h* in each of the five specimens; (**d**) SAR versus standoff; (**e**) API versus standoff. The numbers I, II, III and IV indicate the optimal probe standoffs selected by the PSOM. 42

Figure 2-8 PSOM and experimental results from the SDH at 40 mm depth inside each specimen: (**a**) SLL obtained from *PSF(x)* at each standoff *h*; (**b**) MLW versus *h*; (**c**) TFM images at different probe standoffs *h* in each of the five specimens; (**d**) SAR versus standoff; (**e**) API versus standoff. The numbers I, II, III and IV indicate the optimal probe standoffs selected by the PSOM. 43

Figure 2-9 PSOM and experimental results from the SDH at 70 mm depth inside each specimen: (**a**) SLL obtained from *PSF(x)* at each standoff *h*; (**b**) MLW versus *h*; (**c**) TFM images at different probe standoffs *h* in each of the five specimens; (**d**) SAR versus standoff; (**e**) API versus standoff. The numbers I, II, III and IV indicate the optimal probe standoffs selected by the PSOM. 45

Figure 2-10 TFM image of the three side drilled holes and the specimens' surfaces: (**a**) Concave specimen Cc15 at the probe standoff *h* = 40 mm; (**b**) Concave specimen Cc15 with the PSOM applied to each flaw; (**c**) Benchmark flat specimen F0 at the probe standoff *h* = 40 mm. 46

Figure 3-1 Scheme of proposed beamforming strategy; (a) Single element transmission on flat part; (b) Single element transmission on concave part; (c) Proposed beamforming on concave part. 53

Figure 3-2 (a) Experimental setup; (b) Comparison of beam characteristics for FMC and beamforming strategy 54

Figure 3-3 TFM images of SDH with 1 mm diameter below a concave surface. Images generated using different transmission strategies. 55

Figure 4-1 Schematic of gTFM workflow **(a)** Curvature sectioning of the arbitrary specimen; **(b)** Fixed grid of pixels definition, TFM calculation, and probe positioning; **(c)** Probe positioning relative to curvatures and standoffs; **(d)** gTFM image summation process 62

Figure 4-2 **(a)** Schematic of the probe standoff optimization method (PSOM); **(b)** Schematic of the beamforming strategy to compensate for concave curvature effects on the beam transmission 63

Figure 4-3 **(a)** Drawing of flat aluminum specimen; **(b)** Drawing of stainless-steel complex part representing an aerospace forging mock-up 65

Figure 4-4 Schematic of the experimental setup for application of the gTFM on the specimens 66

Figure 4-5 Schematic of CAD profile upload, discretization, and probe placement. The probe reference system, in the face of the probe, is moved around to the designated targets. 68

Figure 4-6 gTFM of flat aluminum specimen and schematic of the probe positions used to generate each image in the global summation 71

Figure 4-7 gTFM of complex stainless-steel specimen when using a poor scan plan; schematic of the probe positions used to generate each image in the global summation 74

Figure 4-8 gTFM of complex stainless-steel specimen when using a constant standoff scan plan; schematic of the probe positions used to generate each image in the global summation..............................75

Figure 4-9 gTFM of complex stainless-steel specimen when using a scan plan with a range of standoffs; schematic of the probe positions used to generate each image in the global summation 76

Figure 4-10 gTFM of complex stainless-steel specimen when using a scan plan with optimized standoffs (PSOM); schematic of the probe positions used to generate each image in the global summation..77

Figure 4-11 gTFM of complex stainless-steel specimen when using a scan plan with optimized standoffs (PSOM) and beamforming strategy in post-processing; schematic of the probe positions used to generate each image in the global summation..............................79

Figure 4-12 Quantitative comparison of gTFM renderings using CNR, API, and position error as metrics. The strategy number is related to the gTFM images of the complex component presented before. **(a)** Mean contrast-to-noise ratio of all SDHs. **(b)** Mean API of all SDHs. **(c)** Average position error of all SDHs. **(d)** Comparison of CNR and API of SDH number 18 for different strategies. **(e)** Mean CNR of SDHs below concave curvatures. **(f)** Mean CNR of SDHs below convex curvatures. 80

Figure 5-1 Experimental acoustic attenuation of Ni-alloy forged specimens. 84

Figure 5-2 Surface roughness measurement and comparison between 5M and 5F forgings...85

Figure 5-3 C-scan of calibration blocks (Top-view) generated using single-element UT..87

Figure 5-4 Sensitivity of the UT inspection in terms of probe misalignment. 88

Figure 5-5 TFM reconstruction of calibration blocks (side-view) generated using PAUT. 89

Figure 5-6 Equivalency between FBH with 0.79 mm diameter and SDHs of different diameters. 90

Figure 5-7 5M forging bore inspection design and resulting experimental TFM image......92

Figure 5-8 5F forging bore inspection design and resulting experimental TFM image......93

Figure 5-9 Schematic of real flaw inspection - 5M region with anomaly extraction – PAUT of the 5M cube......94

Figure 5-10 TFM image of calibration block for sizing error estimation......95

Figure 5-11 3D TFM rendering of the real flaw acquired through PAUT on the OD surface......95

Figure 5-12 3D rendering of the real flaw acquired through PAUT on the T surface......96

Figure 5-13 (a) CT scan image of the top surface showing the indication length of 0.1284 inches. (b) CT scan image of the outer diameter surface showing the indication height of 0.4329 inches......97

Figure 5-14 Classic UT C-scan of the outer diameter surface showing an indication with 0.262 inches in length and 0.368 inches in width......97

Figure 5-15 Destructive testing of the 5M cube. Polishing steps and micrography of the crack......98

Figure 5-16 Proof-of-concept for as-forged inspection. gTFM image of the 5F forging mock-up......99

Figure 5-17 gTFM on 5F forging. Image generated from the data acquired in a CIVA® simulation......100

Figure 5-18 Schematic of the 5M and 5F specimen preparation for the final feasibility experiment......101

LIST OF ABBREVIATIONS AND ACRONYMS

API	Array performance indicator
CNR	Contrast-to-noise ratio
DAC	Distance amplitude compensation
FBH	Flat-bottom hole
FMC	Full matrix capture
gTFM	Global total focusing method
MLW	Main lobe width
NDE	Nondestructive evaluation
NDT	Nondestructive testing
OD	Outer diameter
P&WC	Pratt & Whitney Canada
PAUT	Phased array ultrasonic testing
PSF	Point spread function
PSOM	Probe standoff optimization method
PWI	Plane wave imaging
SAR	Signal to artifact ratio
SAUL	Surface adaptive ultrasound
SDH	Side-drilled hole
SLL	Side lobe level
SNR	Signal-to-noise ratio
TFM	Total focusing method
UT	Ultrasonic testing

LIST OF SYMBOLS AND UNITS OF MEASUREMENT

A	Active aperture
A_{er}	A-scan in sequence er
c_l	Speed-of-sound
dB	Decibel
D_e	Element directivity
d_e^P	Distance from an emitter to a given pixel
E	Young’s modulus
e	Element width
e	Emitter
g	kerf
g/cm3	Grams per cubic centimeter
Gb	Gigabytes
G_e	Geometric attenuation
h	Probe standoff
I_{max}	Maximum amplitude pixel
m/s	Meters per second
mm	millimeter
n	Number of elements
p	pitch
r	Receiver
R_p	Pressure reflection
t	Time-of-flight

T_e	Transmission coefficient
T_p	Pressure transmission
V_L	Longitudinal waves propagation velocity
V_S	Shear waves velocity
$W_{passive}$	Passive aperture
Z	Acoustic impedance
λ_{Al}	Wavelength in aluminum
ν	Poisson ratio
ρ	Density
$\sigma_{signal2}$	Variance of the pixel intensities
θ_i	Angle of incidence
θ_r	Angle of reflection
θ_l	Angle of longitudinal refraction
θ_s	Angle of shear refraction
δ	Dirac's delta function
μ_{signal}	Mean of the pixel intensities

INTRODUCTION

The ultrasonic inspection of aircraft engine components is a vital manufacturing step in the aerospace industry. Especially in the case of fan disk forgings, as they require an extremely high non-destructive evaluation (NDE) standard. The forging process may introduce flaws into the parts, requiring a careful inspection through immersion ultrasonic testing with focused single-element probes. This ensures that no flaws exist above the high sensitivity limit required by the Federal Aviation Administration. For this reason, the ultrasonic inspection is conducted only after the specimen has been machined into a sonic shape containing only flat surfaces. However, the machining of this intermediary stage is challenging, as these forgings are made of hard alloys. Additionally, if a flaw is identified, all the resources spent to produce the sonic shape are wasted. Thus, this process is not only time-consuming but also prohibitively expensive.

Based on this problem, this project was conceived in partnership with Pratt and Whitney Canada (P&WC) to research and develop innovations on the NDE of their disk forgings. The idea was to verify if the recent developments in phased array ultrasonic testing (PAUT) could be applied to improve the inspection of the forgings in their as-forged state. Even having the manufacturing and testing process already consolidated, there was a demand for verification of whether the sensitivity and efficiency could be increased in any way. And more importantly, if it is feasible to do the inspection of the as-forged parts, in a stage before the sonic machining. This would greatly reduce the environmental and economic impact of disk forging manufacturing.

From an academic point of view, this represents a big challenge, as the inspection of parts with complex shapes remains a difficult task. The curves and the irregular shapes cause poor ultrasonic penetration and a complex sound path, highly degrading the inspection performance. Even though the PAUT imaging of artificial flaws under curved surfaces has been demonstrated in the literature, the surface profile still brings limitations. This turns out to be a topic of interest in the NDE scientific community since parts with complicated geometries are common to several branches of the industry. Therefore, this work also aimed at generalizing the research to any complex specimen, thus contributing to the development of PAUT methods to perform a reliable inspection in such cases.

In the following chapters, the deliverables and results of this work are presented and organized in three parts. In the first part, the industrial motivation and background are presented in depth, revealing the actual manufacturing process and the problems involved. Then, the state-of-the-art in ultrasonic testing is summarized, starting from basic concepts, important throughout the work, up to the latest developments in PAUT of complex specimens. The second part of this work presents the articles written while investigating this problem.

The first article investigated how image artifacts arise from a combination of parameters (e.g., curved profiles, probe aperture, standoff, etc.). And, how these parameters could be integrated in an inspection workflow to avoid errors in the inspection. Thus, the paper demonstrated how the performance of the phased array immersion inspection could be optimized based on the probe standoff. So, a Probe Standoff Optimization Method (PSOM) is presented for the total focusing method (TFM). Using the point spread function (PSF), it calculates the best probe standoff before the inspection. The image quality was compared with the PSOM predictions, to verify if they agreed with the results of the experimental phased array imaging of parts with concave and convex top surfaces. Finally, the improvement of the imaging performance through the optimization process was validated.

Having identified the concave surfaces as the most challenging to inspect in the first paper, the second article aimed at improving the inspection in this case. These curved surfaces cause imaging errors, resulting in poor performances. The ultrasound penetration is lower on this type of interface because a large number of incident waves have angles beyond the critical value for transmission. This lower coverage results in a lower signal-to-noise ratio. Additionally, refraction causes mode conversion and ultrasound paths that contribute to the generation of image artifacts. To mitigate these negative effects, this work proposed a beamforming strategy. The method consists of using sub-apertures to focus on certain points of the specimen’s interface. In such a way that the angle of incidence allows for maximum ultrasound penetration. In conclusion, the details of the method are presented along with the experimental setup and results that show how the method improved the imaging quality.

Then, the third article combines findings of the first two papers in a concluding study. This work proposed a novel method for the PAUT of complex specimens. It combined robotic automation with the TFM while using a digital twin of the inspection setup to apply the PSOM to optimize the scan plan. By combining all probe positions in the image rendering, a global TFM (gTFM) strategy was proposed. All this is in the context of aerospace forging manufacturing, as the method was verified through the inspection of a mock-up designed based on the P&WC disk forging. So, this study finally aimed at showing that it is possible to avoid the machining step and directly inspect the complex-shaped as-forged state.

Finally, the third part of this work contains the industrial application of this research work. In this part, all the studies of the P&WC forgings are presented. Starting from the material characterization, several results of both the standard ultrasonic testing and the PAUT are presented. The sensitivity of both inspection modalities was verified and even the analysis of a real flaw was done and presented. And a final feasibility experiment design was delivered to P&WC to compare the standard ultrasonic testing with the PAUT of the forging stages. Afterward, conclusions from this research are drawn and recommendations for future work are presented.

CHAPTER 1

RESEARCH BACKGROUND

1.1 Industrial motivation

Ultrasonic inspection of aircraft compressors and fan disk forgings lies among the most critical NDE processes in the aerospace industry (Margetan, 2007). These parts have their integrity investigated for abnormalities in the microstructure in two stages during manufacturing: before the forging, while as a billet, and after the forging. The bulkiness and density of these parts do not allow for the use of x-ray, so the NDE must rely on ultrasonic testing. The inspections are carried out to ensure that the resulting engine parts have no flaws above the sensitivity limit. And since these parts operate at high thermo-mechanical stresses, the sensitivity of the evaluation must be as high as possible. Thus, minimizing to practically zero the chance of catastrophic failures, as the consequences would be dramatic (Howard et al., 2007). Based on the microstructure of the materials and deep investigation of possible manufacturing defects, the Federal Aviation Administration (FAA) set those sensitivity limits as the ultrasonic testing response obtained from flat bottom holes (FBH) ranging from 1.2 to 0.4 millimetres in diameter (Margetan, 2007). These artificial flaws are equivalent to a disk-shaped void. To identify such small flaws, the inspection uses single crystal ultrasonic probes with a fixed spherical focus and a centre frequency ranging from 5 to 10 MHz. Moreover, the inspection must ensure full coverage of the forging cross-section.

In this context, Pratt and Whitney Canada (P&WC) proposed a case study of one of their disk forgings. The manufacturing process is depicted in the schematic shown in Figure 1-1. It all starts with the billet made of a Ni-alloy named Waspalloy. This billet is then ultrasonically inspected according to the FAA guidelines and if approved it is forged into a shape called 5F. The 5F shape represents the as-forged stage. Even though the billet had its integrity approved, the forging process may introduce discontinuities or anomalies in the metallic matrix of the part. As the billet is hot pressed, voids and cracks parallel to the plane of the grain flow can emerge from a lack of fusion in the metal. These defects are rare because of the recrystallization process done to control the grain size, which ensures an equiaxed and uniform microstructure. This is shown in Figure 1-2, where the micrography of a Waspalloy sample illustrates the equiaxed microstructure obtained through the forging of the billet, but also a crack, an unwanted result of this process.

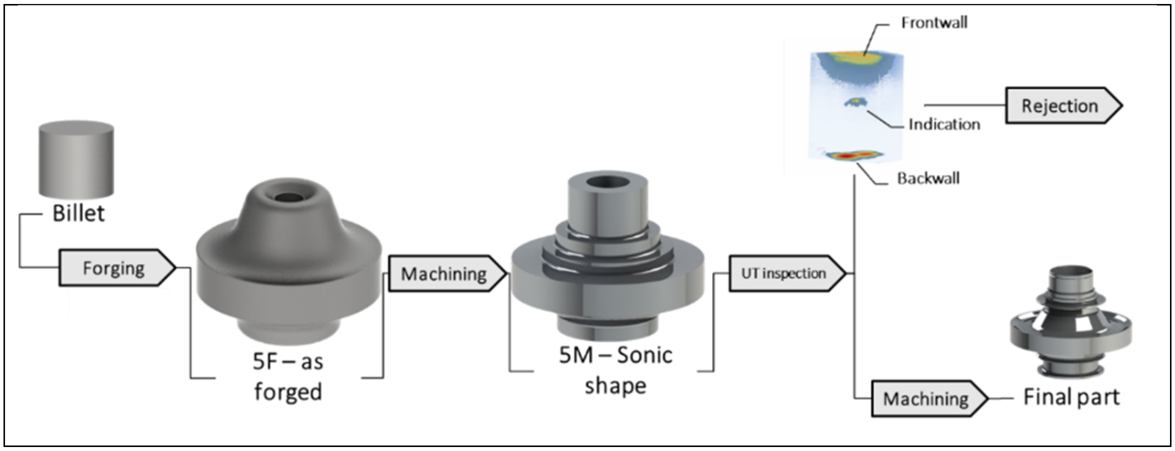
Frontwall
Rejection
Indication
Backwall
Billet
Forging
Machining
UT inspection
5F – as forged
5M – Sonic shape
Machining
Final part

Figure 1-1 The P&WC turbine disk forging manufacturing and NDE process schematic

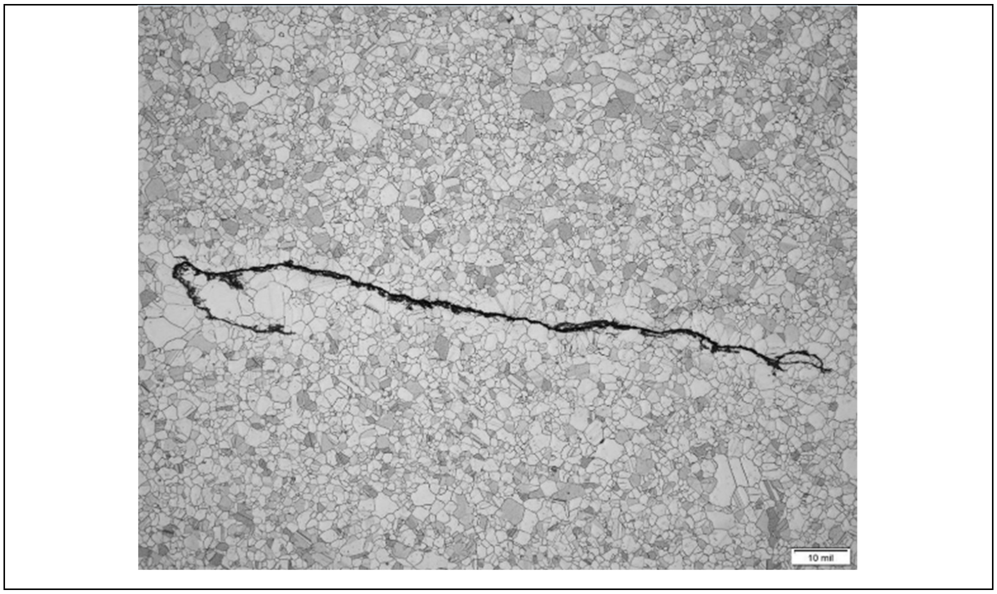

Figure 1-2 P&WC Waspalloy sample micrography showing equiaxed microstructure and the presence of a crack

Therefore, since no flaw can be accepted in the final part, a second ultrasonic inspection must be conducted. So, following the process depicted in Figure 1-1, the 5F is then machined to a sonic shape, called 5M. This shape ensures full inspection coverage of the forging while enabling multi-direction ultrasound incidence in the same section. The latter is important because of the directional nature of the possible cracks, as they present a higher probability of detection from certain angles. Moreover, this intermediary sonic machining ensures precise geometries containing flat and smooth surfaces. This results in excellent ultrasound penetration and known wave paths, allowing a signal-to-noise ratio over the FAA sensitivity limit.

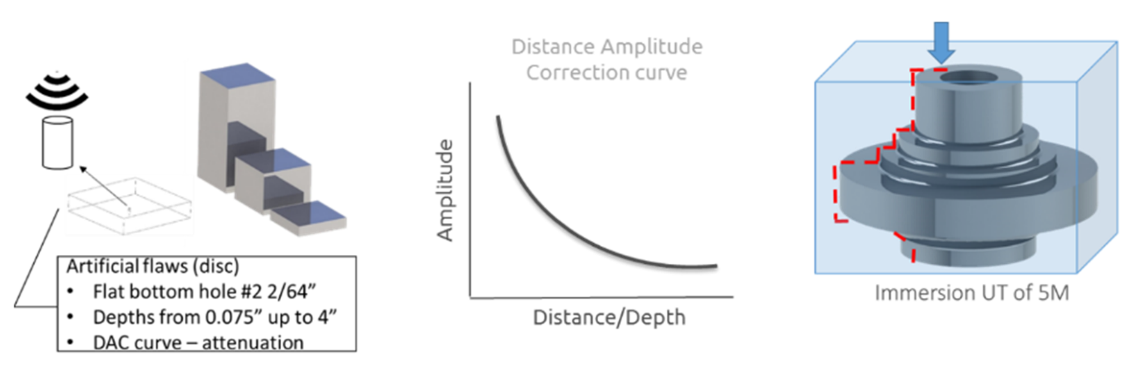
Artificial flaws (disc)
Flat bottom hole #2 2/64”
Depths from 0.075” up to 4”
DAC curve – attenuation
Distance Amplitude Correction curve
Amplitude
Distance/Depth
Immersion UT of 5M

Figure 1-3 The ultrasonic testing of the 5M disk forging – calibration process and immersion UT scan plan

After the sonic machining is done, ultrasonic testing (UT) shown in Figure 1-3 is conducted. To search for these potential defects, the ultrasonic testing of the sonic shape is done using focused single-element probes in an immersion setup. The first step is the calibration of the ultrasonic response using the calibration blocks of the same Ni-alloy. These blocks have one FBH of 0.8 millimetres in diameter at different heights. The goal is to set the limit of minimum pulse amplitude at each depth, so any indication above this limit is flagged and considered an anomaly. For this purpose, a distance amplitude compensation curve (DAC) is constructed to compensate for the attenuation effect on the ultrasonic pulse signal. Finally, the ultrasonic test is conducted with the probe scanned along the planned positions shown by the red dashed line in Figure 1-3. Then the signals from the ultrasonic test are combined into B-scans or C-scans, and by using gates, any reflection with 70% of the FBH amplitude, or more, is considered an indication of a flaw.

After the inspection, as illustrated in Figure 1-1, if the 5M part is approved by the UT it is then machined to its final shape. The problem is, however, that if a flaw is identified, all the resources spent to produce the sonic shape are wasted. This process is not only time-consuming but also prohibitively expensive. The Ni-alloy has a high hardness and thus the machining process is extremely challenging and costly, due to the fast wear of the cutting tools.

Nonetheless, this process is done in this fashion because this standard UT inspection is a consolidated way to ensure the integrity of aerospace turbine forgings. Still, the aerospace industry seeks improvement in this area. That's why this partnership with P&WC brought the proposition of the big question this project aims to answer:

Is it possible to avoid this intermediary sonic machining step?

This would have a great impact on the reduction of waste associated with the machining process. But at the same time, this would mean that the ultrasonic inspection must be conducted on the 5F or as-forged shape. Thus, this represents an important academic challenge, as the ultrasonic inspection of complex components remains a difficult task. This is a topic of interest for the NDE scientific community since the curves and the irregular shapes in the complex component cause poor ultrasonic penetration and a complex sound path. As a result, the performance of the inspection is highly degraded, and the calibration is not straightforward. So, the non-flat surface profile of these parts scatters and refracts the ultrasonic waves in a way that renders it unfeasible to inspect with the classical single-element UT.

Given this challenge, this research project envisioned the strong development of ultrasonic phased arrays in the last 20 years as an opportunity to tackle this problem. Phased array ultrasonic testing (PAUT) reached a maturity level that places it as a real substitute for the classic UT methods. PAUT can greatly increase the efficiency of the inspection, with greater capacity and versatility, better sensitivity, better signal-to-noise-ratio, and fewer errors associated with the operator. And most importantly, it may be feasible to inspect the parts with complex shapes, having strong curvatures and rough surfaces. As it has been demonstrated in the literature, artificial flaws under curved surfaces could be imaged accurately. Still, the surface profile causes problems and the experiments showed important inspection limitations. So, the main research task of this project is to verify and develop PAUT methods capable of performing a reliable 5F inspection. All while investigating the possible benefits of the PAUT to the 5M inspection, advancing the reliability and efficiency of this crucial process. In the following sections, the state-of-the-art of PAUT is presented as the base where this research will be constructed. Finally, the aim is also to contribute with methods that are of general application to the inspections of complex parts, being useful to other industries facing similar challenges, such as additively manufactured metals.

1.2 State-of-the-art

This section presents relevant concepts to the NDE of complex parts. Starting from the basic concepts of ultrasound propagation up to state-of-the-art PAUT. Advanced imaging algorithms are presented along with the main developments done in the context of PAUT of complex-shaped specimens. In this sense, specific contributions made to the ultrasonic inspection of aerospace forgings are also explored.

1.2.1 Ultrasonic testing

Ultrasonic inspection is a NDE method broadly used for medical and industrial applications. This is because UT represents a cheaper and safer alternative, than x-rays for example, to assess the interior condition of an opaque object. UT method consists of a probe that excites, with ultrasonic frequency, mechanical waves that will propagate within the specimen under analysis. Then, the interaction of the propagating wave with variations in the acoustic impedance of the medium causes some of the energy to be reflected. The back-propagated waves, called echoes, are used to imply what feature of the part is causing the reflection.

Figure 1-4(a) shows a scheme representing the UT of a solid specimen with a flaw. The probe is usually composed of a piezoelectric crystal that converts electrical signals into mechanical vibration and vice versa (Schmerr, 2015). In the classical UT, only one element generates and receive the mechanical pulses. This excitation generates an elastic wave front in the medium that travels and interacts with the changes in the medium, which in this case is a spherical reflector. The echoes from these features are then read as electrical signals and displayed as a graph called A-scan, as illustrated in Figure 1-4(b). This diagram contains the intensity and arrival delay of each echo, from which it is possible to estimate the position of each feature. Hence, this technique allows the identification of discontinuities within the part.

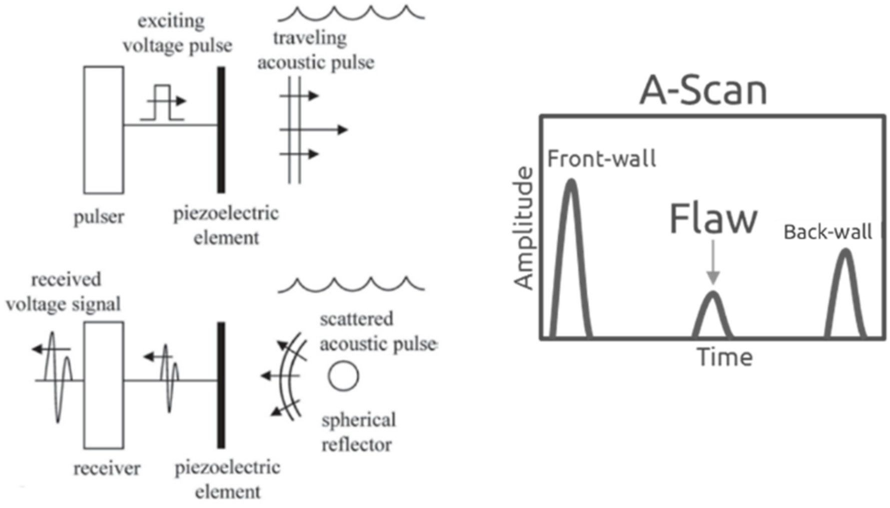
exciting
voltage pulse
traveling
acoustic pulse
pulser
piezoelectric
element
received
voltage signal
scattered
acoustic pulse
spherical
reflector
receiver
piezoelectric
element
A-Scan
Front-wall
Flaw
Back-wall
Amplitude
Time

(a) (b)

Figure 1-4 (a) Ultrasonic testing scheme
(b) Ultrasonic testing A-scan example
Adapted from Schmer (2015, p. 75)

1.2.2 Physics of Ultrasonic Testing

UT is based on the elastic wave propagation phenomena. These mechanical waves can be defined as a travelling perturbation that causes an oscillatory motion on the particles of a medium around its initial position. This disturbance is generated when an external force or vibrational motion is applied, creating an oscillatory elastic deformation front that travels at a given propagation velocity. The elastic properties of the medium, the nature of the excitation, and the medium geometry define the type of wave and its propagation velocity.

The most important type of wave in the context of this work is the bulk acoustic wave. This type of wave propagates through the volume of a medium. There are two types of bulk waves, longitudinal and shear waves. As shown in Figure 1-5(a), longitudinal waves cause the particles to oscillate in a direction parallel to their direction of propagation, while shear waves cause a motion perpendicular to the propagation direction. Moreover, shear waves only propagate in solids, as non-viscous fluids cannot support shear forces. Another important concept is the wave behaviour at the solid-liquid interface, as it occurs in immersion UT. As illustrated in Figure 1-5(b), depending on the angle of incidence and media properties, a longitudinal wave will be refracted, reflected, and converted into a shear wave (Cheeke, 2012).

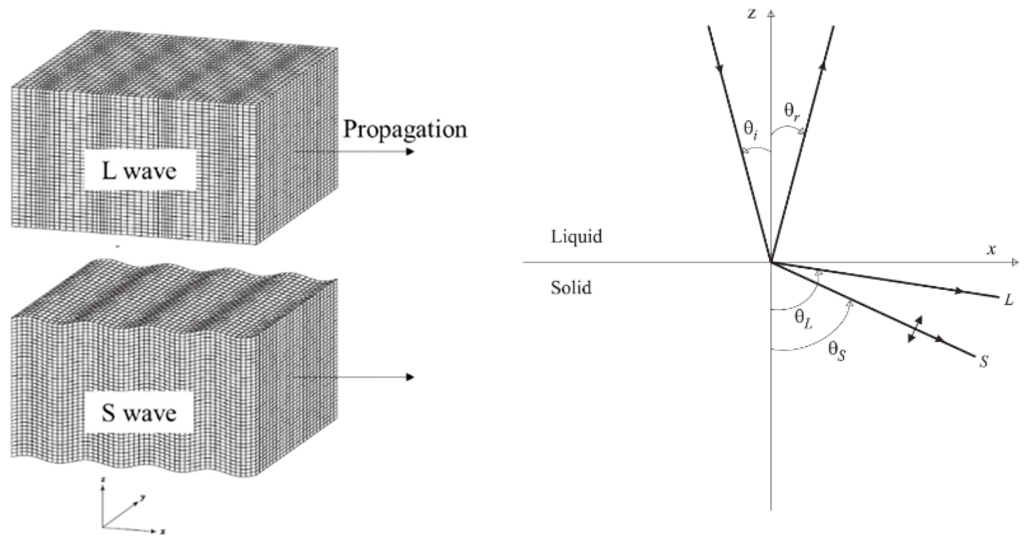

(a) (b)

Figure 1-5 (a) Longitudinal and shear waves particle motion pattern (b) Refraction, transmission, and reflection of bulk waves at the solid-liquid interface
Adapted from Cheeke (2012, p. 35)

These are important features of wave behaviour because UT takes advantage of the reflection to infer internal abnormalities. And more importantly, on the inspection of curved parts, the interface will cause refraction patterns that create a complex wave path. Thus, it is important to define the speeds-of-sound and acoustic impedance of the testing materials to estimate these patterns. The propagation velocity of these waves can be estimated using Hooke's law to relate the material properties and particle displacement. After simplification, the longitudinal waves have a propagation velocity V_L and shear waves a velocity V_S, which are given by equation 1.1. For a homogeneous and isotropic solid, these equations relate Young's modulus (E) with the density (ρ) and the Poisson ratio (ν) of the medium (Cheeke, 2012).

$$V_L = \sqrt{\frac{E(1-\nu)}{\rho(1+\nu)(1-2\nu)}};\ V_S = \sqrt{\frac{E}{2\rho(1+\nu)}} \tag{1.1}$$

Adapted from Cheeke (2012, p. 89)

The restriction of the sound wave propagation to a finite speed is an intrinsic characteristic of the medium, called acoustic impedance. This property defines how the energy is transmitted through and between different mediums and is used to account for wave reflection, refraction, and transmission mechanisms. The acoustic impedance (Z) is measured as the product of the wave propagation velocity versus the density of the medium, as given by equation 1.2 (Cheeke, 2012).

$$Z = \rho V \tag{1.2}$$

Adapted from Cheeke (2012, p. 90)

So, at normal incidence, the pressure transmission (T_p) and reflection (R_p) coefficients can be defined as:

$$T_p = \frac{2Z_2}{Z_1 + Z_2} \tag{1.3}$$

$$R_p = \frac{Z_2 - Z_1}{Z_1 + Z_2} \tag{1.4}$$

Adapted from Cheeke (2012, p. 101)

While at oblique incidence, the well known Snell's law can be applied (Cheeke, 2012):

$$\frac{sin\theta_i}{V_1} = \frac{sin\theta_r}{V_1} = \frac{sin\theta_l}{V_L} = \frac{sin\theta_s}{V_S} \tag{1.5}$$

Adapted from Cheeke (2012, p. 113)

Which is a simplification of Fermat’s principle that states that a wave travels through an interface by the path of stationary time-of-flight.

Still, these assumptions for wave propagation depend on the capacity for wave generation. The generation of the ultrasonic waves by the piezoelectric components can be modelled as the union of several point sources. When a point source is excited in a medium, it generates a spherical bulk wavefront. As shown in Figure 1-6, the superposition effect of the various sources creates an interference pattern, forming the ultrasonic beam. This beam can be divided into two regions, the near field, and the far field. At the end of the near field, the natural focus of the probe is localized. Furthermore, the ultrasonic beam has a diffraction effect as it propagates into the medium. All these parameters are defined by the frequency, bandwidth, and geometry of the piezoelectric crystal.

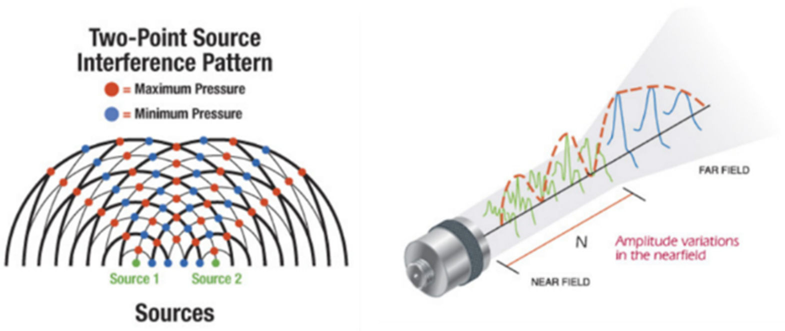
Two-Point Source
Interference Pattern
● = Maximum Pressure
● = Minimum Pressure
Source 1
Source 2
Sources
FAR FIELD
N
Amplitude variations
in the nearfield
NEAR FIELD

Figure 1-6 Schematics of the ultrasonic beam main characteristics
Adapted from Olympus NDT (2004, p. 26)

1.2.3 Phased array ultrasonic testing

The phased array ultrasonic technology has reached its maturity in the twenty-first century, being already commercialized by different companies. Sectors of the industry such as aerospace, oil and gas, nuclear, and others already rely on this technology to non-destructively inspect their parts. Phased array ultrasonic testing (PAUT) is regularly employed given its improved inspection quality and flexibility over single element transducers (Drinkwater & Wilcox, 2006). PAUT uses multiple ultrasound transduction elements to generate images of the components under inspection. Different acquisition methods can be applied to generate the desired type and pattern of ultrasonic waves within the analyzed component. Then the back-propagated waves from features inside the part can be converted into images through data processing methods. The result is a more reliable technique that drastically reduces errors from the operator, common in conventional UT.

PAUT can be seen as a concatenation of several mono-element transducers inside a single probe. Hence, the PAUT probe contains a given number of individually connected piezoelectric elements. By controlling the emission-reception pattern of each one of these elements, it is possible to perform several different inspection methods. This is because with the PAUT it is possible to steer and focus the ultrasonic beam to different directions and depths inside the inspected part. The beamforming is generated by a controller unit. A pattern is applied as time delays between the excitation of each piezoelectric element. Figure 1-7 illustrates how the delays applied to the probe can modify the wave-front direction and focus.

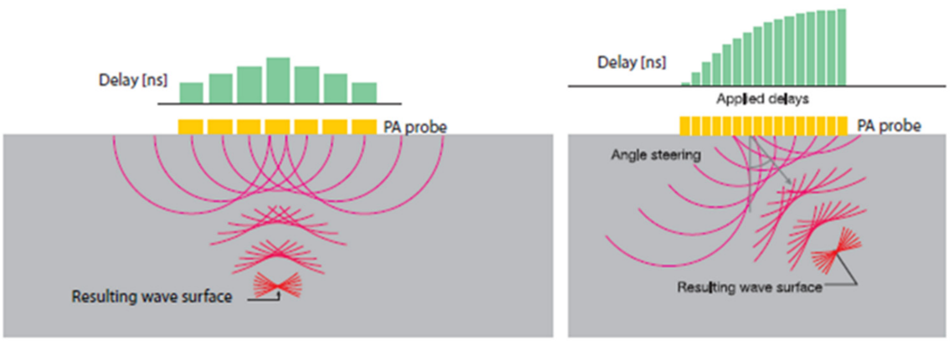

Figure 1-7 The PAUT's ability to focus and steer the wavefront using delays
Adapted from Olympus NDT (2004, p. 34)

With this capacity, real-time images from the component’s interior can be rendered while inspecting several areas with a single probe position. And not only the area below the probe aperture, by using the beam steering capacity (Drinkwater & Wilcox, 2006).

In general, the transducer arrays are limited to below 256 transmit–receive independent channels. This represents the maximum number of elements that can be used simultaneously. The design of the PAUT transducers follows a few rules that determine the main dimensions. Figure 1-8 shows a schematic containing all the dimensional features of a linear phased array probe.

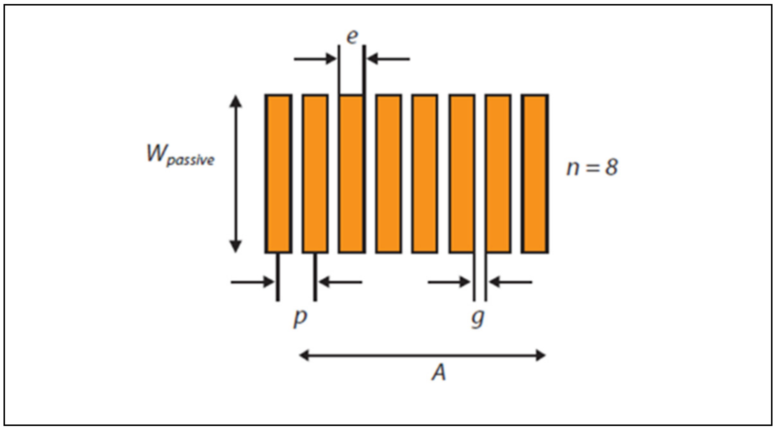

Figure 1-8 The PAUT probe design dimensions.
$W_{passive}$ – Passive aperture; n – number of elements;
e – element width; g – element spacing or kerf; p – pitch
Adapted from Olympus NDT (2004, p. 54)

One of the main parameters, the element width (e), is selected based on the wavelength of the wave mode of interest propagating in the inspected part. To avoid unwanted ultrasonic grating lobes, the design rule dictates an element width smaller than half a wavelength. Also, the general guide is to keep the centre-to-centre distance between two elements or pitch (p) smaller than 67 percent of the wavelength. This determines the spacing between the elements (g). The number of elements (n) and the pitch determine the active aperture (A) of the transducer. Finally, the length of the elements, called passive aperture ($W_{passive}$), should be bigger than 8 times the pitch to keep a small beam width. This is important to resolve small reflectors inside a part (OLYMPUS NDT, 2004).

Ultrasonic array transducers can be classified as one-dimensional (1-D), two-dimensional (2-D), or annular. In the case of 1-D arrays, the array elements are typically long in the passive direction to create a focal point in elevation. Figure 1-9 illustrates different configurations for array transducers. Linear arrays are the most applied because of their ease of design, manufacture, versatility, and relatively low cost (Drinkwater & Wilcox, 2006).

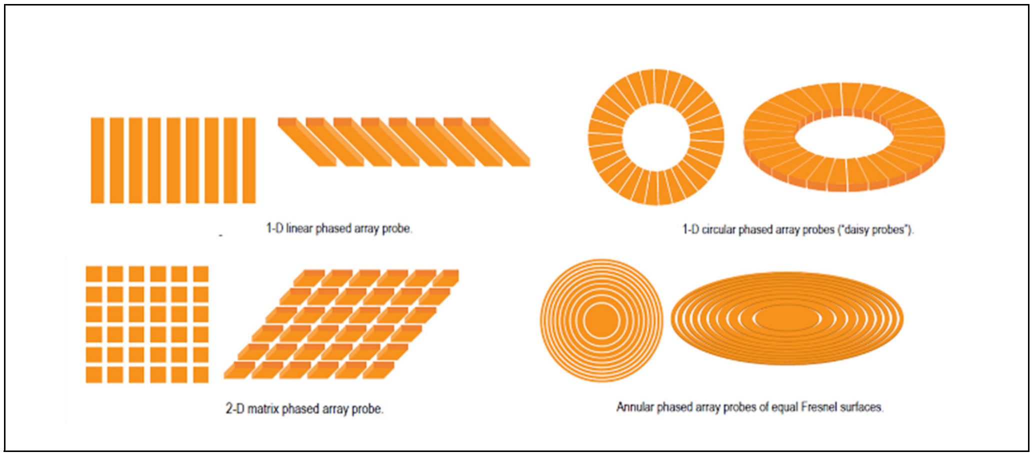
1-D linear phased array probe.
1-D circular phased array probes ("daisy probes").
2-D matrix phased array probe.
Annular phased array probes of equal Fresnel surfaces.

Figure 1-9 Examples of possible element arrays for PAUT probes
Adapted from Olympus NDT (2004, p. 64)

Different forms of beamforming and data acquisition were proposed for PAUT industrial applications in the literature. The most relevant in the context of this work will be presented in the sections below.

1.2.4 Phased array ultrasonic testing on components with non-flat surfaces

Extensive research has been conducted on the ultrasonic NDE of components with complex geometries. Some studies have focused on the probe-surface interaction, ensuring a perfect adaptation using flexible probes (Chatillon, Cattiaux, Serre, & Roy, 2000; Hunter, Drinkwater, & Wilcox, 2010) and shape sensing fibres (Lane, 2014). These were successful proofs of concept that the imaging of internal defects is improved when the probe is adapted to the surface curvature. Through another approach, researchers worked on adaptable coupling mediums, such as a water-filled membrane (Russell, Long, & Cawley, 2010) and even encasing the part in ice (Simonetti & Fox, 2019). These were shown to also improve the ultrasonic inspection of the complex specimens. However, both approaches are too complex and expensive, giving water immersion the upper hand on the choice of being an alternative to be further explored. In water immersion inspection, no custom wedges or special probes are needed, minimizing the inspection complexity and cost.

Techniques to improve the PAUT of complex components using water immersion were first studied by (Mahaut, Roy, Beroni, & Rotter, 2002). These improvements were obtained through the beamforming of the ultrasonic waves using delay laws. This approach adapts the ultrasonic beams to the surface shape, compensating for the distortions caused by it, and allowing better defect characterization. Similarly, the surface-adapted ultrasound or SAUL was proposed, where the researchers proposed using several ultrasound firings, updating the delay law at each step until the beam was adapted to the surface shape (Hopkins et al., 2013). These online inspection approaches received less attention with the introduction of full matrix capture or FMC. The FMC allowed advanced imaging algorithms to be developed and applied with more flexibility to these complex structures.

Among these imaging methods for complex structures, the total focusing method (TFM) is the most prominent (Hunter et al., 2010; Sébastien Robert, Casula, Roy, & Neau, 2013; M. Sutcliffe et al., 2013). Alternatives were also demonstrated, such as plane wave imaging (PWI) (Rachev, Wilcox, Velichko, & McAughey, 2020) and virtual source aperture techniques (Hoyle, Sutcliffe, Charlton, & Rees, 2018) to post-process the FMC of nonplanar parts into sharp subsurface images. More recently, even volumetric imaging through doubly curved interfaces using a matrix probe was demonstrated (McKee, Bevan, Wilcox, & Malkin, 2020). The results showed a correct reconstruction of the artificial flaws beneath the complex surface geometries. However, the imaging performance for characterization and sizing of these defects, even for surfaces that were curved very slightly, was very sensitive to an incorrect surface compensation. Finally, since all of these were inspired by the TFM, this work will focus its efforts on optimizations and applications of the latter.

1.2.5 Full matrix capture (FMC)

The spike in computational power in recent years allowed the development and vast application of a method that can be placed as the most versatile in PAUT, the full matrix capture (FMC). This method is becoming more popular because it has the advantage of containing all ultrasonic data from the inspection. So, any imaging or beamforming method can be executed online or in post-processing of the FMC data. The only drawback is the large amount of data to be stored and processed, which is compensated by its flexibility (Holmes, Drinkwater, & Wilcox, 2005). As illustrated in Figure 1-10, this ultrasonic testing method consists of firing only one element of the probe for each sequence, while recording all the elements in the array. The emitter (e) excites non-focused waves, while the receivers (r) capture the back propagated waves. Hence, considering a probe with N elements, the method consists of executing N emission sequences, each with N reception channels. The output is an NxN matrix of time-domain signals or A-scans (A_{er}) that contains all combinations of transmitting and receiving elements (A_{11}, A_{12}, …, A_{1N}, A_{21},…, A_{N1},…, A_{NN}).

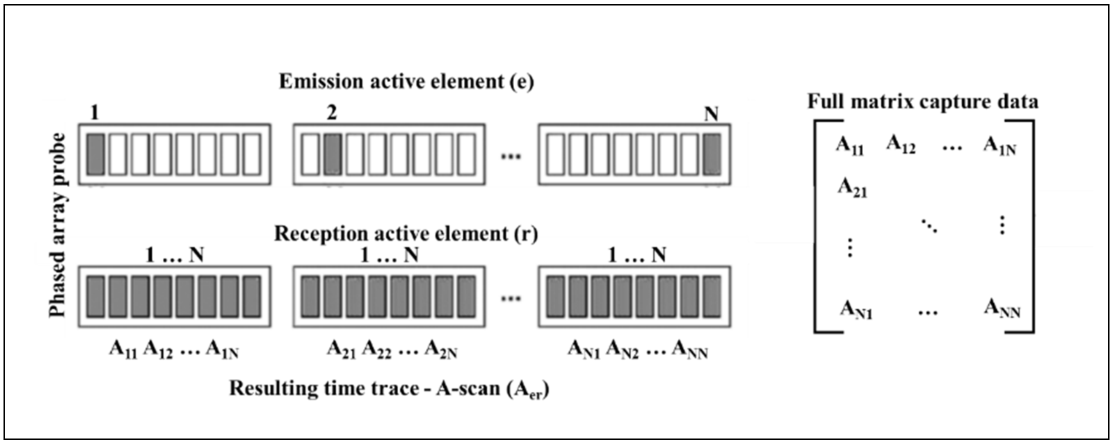
Emission active element (e)
1
2
N
Phased array probe
Reception active element (r)
1 … N
1 … N
1 … N
A11 A12 … A1N
A21 A22 … A2N
AN1 AN2 … ANN
Resulting time trace - A-scan (Aer)
Full matrix capture data
A11 A12 … A1N
A21
AN1 … ANN

Figure 1-10 Full matrix capture representation
Adapted from Sutcliffe M., et al. (2012, p. 2)

The FMC acquisition allows the use of several post-processing techniques to render images internal images of the engineering components. On the most relevant, researchers have proposed plane wave imaging, or PWI, which uses the composition of plane waves in different angles of incidence to generate focused images of the component's cross-section (L. Le Jeune, Robert, Lopez Villaverde, & Prada, 2016). On another front, some works proposed the use of virtual sources, generated by delaying sub-apertures of the array, to generate the internal images (Hoyle et al., 2018). However, these methods are derivations of the most prevalent one, called the total focusing method (TFM) (Holmes et al., 2005). The TFM is still considered the "gold standard" in image quality by the NDE community. The other methods have shown slight image improvements in certain situations, but the quality is still comparable to the TFM.

1.2.6 Total focusing method (TFM)

The total focusing method (TFM) was introduced as an imaging strategy where the beam is focused on every point in the target region. This approach has been suggested by several authors (McNab & Stumpf, 1986; Oralkan et al., 2002; Pompei & Wooh, 2002) but was not immediately applied to industrial NDE systems. The high number of transmitting delay sequences and the computational power required prohibited the use of the technique. However, (Holmes et al., 2005) introduced the possibility of applying the total focusing method approach as a delay-and-sum post-processing strategy by using the FMC. Such strategy was applied to an aluminum block containing an EDM notch and the results showed that the TFM surpassed the performance from both plane and focused B-scans, with a better signal-to-noise ratio.

The TFM method is illustrated in Figure 1-11. Here all the time-domain data from the full matrix capture is used to reconstruct an image from a region inside the test specimen. First, the region of interest is divided into a grid of pixels. Then, the position of the transducer array is used to calculate the direct distance (d_e^P) from an emitter to a given pixel (P), and the distance (d_r^P) from this pixel to a receiver. This distance is divided by the wave propagation velocity (V_L) to calculate the time-of-flight (t). Finally, the amplitude intensity I(P) at a given pixel is equivalent to the coherent summation of all the time-domain signals S_{er}, converted into complex form through a Hilbert transform, at the calculated time-of-flight:

$$I(x_P, z_P) = \left| \sum_{e}^{N} \sum_{r}^{N} S_{er} \left(\frac{\sqrt{(x_e - x_P)^2 + {z_P}^2} + \sqrt{(x_r - x_P)^2 + {z_P}^2}}{V_L} \right) \right|. \tag{1.6}$$

Which is equivalent to synthesizing a focus at every point in the grid (Holmes et al., 2005).

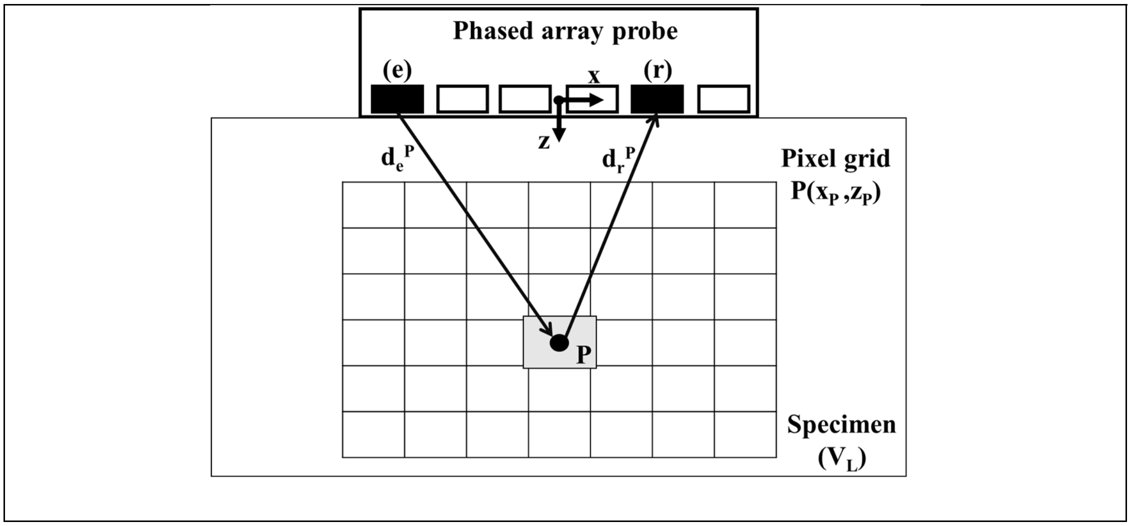

Figure 1-11 Schematic of the total focusing method (TFM)

The advantage of this approach is the use of all available information in the FMC data, which increases sensitivity to small defects and enhances resolution and inspection coverage. If the signal-to-noise ratio is an issue, it has been shown that a solution can be obtained through averaging or the use of encoded signals such as Golay sequences (Holmes et al., 2005).

Additionally, the TFM was demonstrated to be also applicable in immersion inspection of parts with complex geometries (Hunter et al., 2010). Figure 1-12 shows an example of this imaging. In this case, the waves travel through a dual-layered media, and the refraction must be considered in the calculation of the times of flight. Thus, the interface geometry and position relative to the probe must be known. This adds up to the computational cost of the post-processing, but work has been done to improve the efficiency of the method, allowing real-time rendering of the images for both known (Mark Sutcliffe, Weston, Dutton, Cooper, & Donne, 2012) and unknown geometries (M. Sutcliffe et al., 2013).

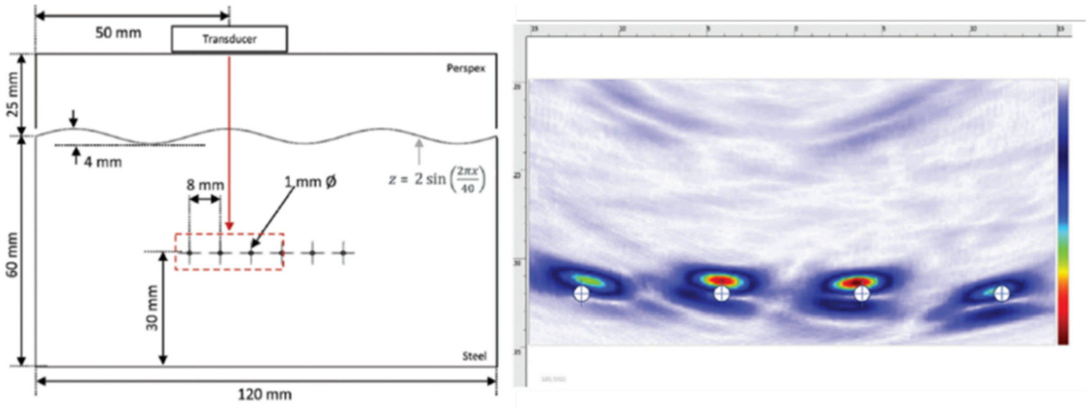

Figure 1-12 Example of TFM applied to a specimen with a curved surface
Adapted from Sutcliffe M., et al. (2013, p. 5)

In the case of unknown surface geometries, several methods of surface reconstruction using ultrasonic data have been demonstrated (S. Robert, Calmon, Calvo, Jeune, & Iakovleva, 2015). The most successful is the use of the TFM, but considering only the first layer of the material, to reconstruct a focused image of the specimen's surface (M. Sutcliffe et al., 2013). In addition, (Zhang, Drinkwater, & Wilcox, 2014) presented a method of surface discretization to reduce the number of surface points in the TFM calculation without losing imaging performance. However, the curved interfaces in these components cause beam distortions that led to a loss of sensitivity and coverage, lowering the inspection capacity for defect detection and characterization (Mahaut et al., 2002). Even with demonstrated methods for proper surface identification (Kerr, Pierce, & Rowe, 2016; Matuda, Buiochi, & Adamowski, 2019) or perfect surface adaptation, the imaging performance still suffers if strong curvatures are present in the profile (Malkin, Franklin, Bevan, Kikura, & Drinkwater, 2018). Therefore, optimizations and adaptations must be researched to ensure the reliability of the inspection of complex components.

Moreover, in the specific case of the TFM applied to aerospace forgings there is a shortage of research works. The work presented by (Brown, Dobson, Pierce, Dutton, & Collison, 2017) brought a discussion on the use of TFM in the immersion inspection of titanium disks. As shown in Figure 1-13, a brief comparison of the influence of the curved surface radius on the imaging sensitivity of a flat bottom hole was presented. As expected, the imaging performance varied according to the radius, but also with the type of curve, whether it is concave or convex. This reinforces the need for this application for further investigation.

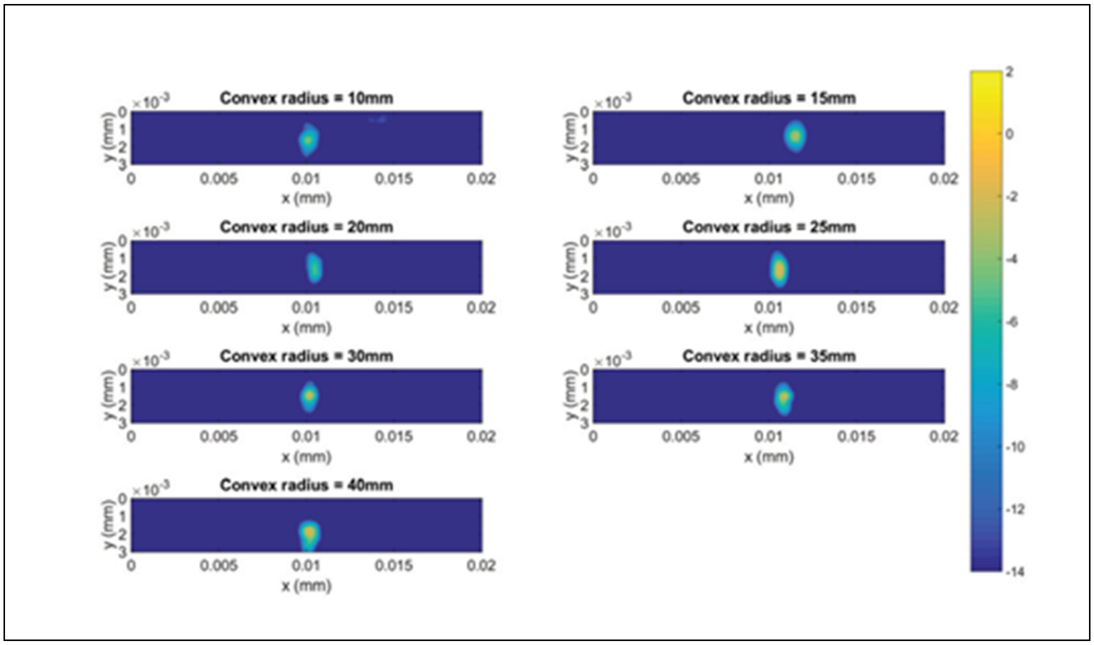

Figure 1-13 Imaging of FBH under different curved surface radii
Adapted from Brown et al. (2017, p. 8)

1.3 Research scope and introduction to articles

The scope of this research project envisioned filling the gaps that are holding the broad industrial adoption of the PAUT for the inspection of complex components. Therefore, the aim was to research and develop improvements in the reliability of the inspection through optimizations and novel approaches tailored to the case study of components with curved profiles. More specifically, having identified the FMC and the TFM as the most advanced and promising alternatives, this project investigated the limits of the performance of these methods. Since its feasibility depends on the knowledge and mitigation of the detrimental effects caused by the curved surfaces to the imaging performance. All in all, allowing the generalization of the findings to other industries but also answering the question of the aerospace as-forged inspection feasibility. And not only that but also shows that the PAUT can greatly improve the sensitivity of the inspection even if keeping the sonic shape is the preferred solution.

Having this defined, the first paper demonstrates how the performance of the phased array immersion inspection could be optimized based on the probe standoff, in combination with the part surface profile and flaw depth. Hence, a Probe Standoff Optimization Method (PSOM) was presented, which uses the point spread function (PSF) to calculate the best probe standoff before the inspection. The total focusing method was implemented through a dual-layer media on aluminum specimens and the resulting image quality was verified and compared with the PSOM predictions. The aim was to verify if the PSOM could predict the experimental phased array imaging performance of parts with concave and convex top surfaces, to ensure optimal imaging performance.

However, it was observed that even high-quality image rendering algorithms such as the TFM allied to the PSOM still suffered from the effects of concave interfaces. The ultrasound penetration and focusing capacity were poor on this type of interface, causing image reconstruction artifacts. Therefore, the second paper proposed a beamforming strategy to mitigate these negative effects and improve image quality. The method consisted of a beamforming strategy that uses sub-apertures to focus on certain points of the interface. These points were selected in such a way that the angle of incidence allows for maximum ultrasound penetration.

Finally, the third paper combined both these works with cutting-edge technology to propose a novel approach to the inspection of complex specimens. By combining robotic automation with the ultrasonic phased array TFM imaging, the method used a digital twin of the inspection setup to optimize the scan plan. And by using all probe positions in the image rendering, a global TFM (gTFM) strategy was proposed. The method was verified with a mock-up of aerospace forging with a complex profile. This case study was selected to work as a proof of concept for the feasibility of PAUT on as-forged specimens. So, the aim is to show that it is possible to avoid this machining step by enabling the inspection of the complex-shaped as-forged state.

CHAPTER 2

PROBE STANDOFF OPTIMIZATION METHOD FOR PHASED ARRAY ULTRASONIC TFM IMAGING OF CURVED PARTS

J. F. Mansur Rodrigues Filho and P. Bélanger

Department of Mechanical Engineering, École de Technologie Supérieure,
1100 Notre-Dame West, Montreal, Quebec, Canada H3C 1K3

Paper published in *Sensors*, October 2021

2.1 Abstract

The reliability of the ultrasonic phased array total focusing method (TFM) imaging of parts with curved geometries depends on many factors, one being the probe standoff. Strong artifacts and resolution loss are introduced by some surface profile and standoff combinations, making it impossible to identify defects. This paper, therefore, introduces a probe standoff optimization method (PSOM) to mitigate such effects. Based on a point spread function analysis, the PSOM algorithm finds the standoff with the lowest main lobe width and side lobe level values. Validation experiments were conducted and the TFM imaging performance compared with the PSOM predictions. The experiments consisted of the inspection of concave and convex parts with amplitudes of 0, 5 and 15 λ_{Al}, at 12 standoffs varying from 20 to 130 mm. Three internal side-drilled holes at different depths were used as targets. To investigate how the optimal probe standoff improves the TFM, two metrics were used: the signal-to-artifact ratio (SAR) and the array performance indicator (API). The PSF characteristics predicted by the PSOM agreed with the quality of TFM images. A considerable TFM improvement was demonstrated at the optimal standoff calculated by the PSOM. The API of a convex specimen's TFM was minimized, and the SAR gained up to 13 dB, while the image of a concave specimen gained up to 33 dB in SAR.

Keywords: TFM; PSF; phased array; ultrasound; standoff; curved surfaces

2.2 Introduction

Interest in the ultrasonic inspection of components with complex shapes is rising rapidly. Research in phased array ultrasonic testing have shown that defects can be identified even under curved surfaces (Hunter et al., 2010; Mahaut et al., 2002; M. Sutcliffe et al., 2013). This possibility explains the increased interest in the technique among different industries, including aerospace and automotive. Since their forgings, castings, composites, and more recently, their 3D printed metals (Honarvar & Varvani-Farahani, 2020), will benefit greatly from a non-destructive inspection of their final and complex shape. An example of the traditional handling can be seen in the case of some aerospace forgings, where a sonic machining with a flat surface is required just for the ultrasonic inspection (Brown et al., 2017), which increases the production cost. The complexity of predicting the ultrasound path and coverage is among the difficulties that have traditionally discouraged the ultrasonic inspection of forged parts with curved and variable profiles.

However, this complexity is mitigated with the phased arrays, since they allow the control the beam profile and direction, along with a broad selection of post-processing techniques (Drinkwater & Wilcox, 2006). Additionally, to handle the non-flat surface profiles, studies have successfully demonstrated the possibility of using shaping sensing fibers (Lane, 2014), flexible array transducers (Chatillon et al., 2000; Hunter et al., 2010; Russell et al., 2010), and even the use of ice as a coupling medium (Simonetti & Fox, 2019). Still, water immersion along with adaptive methods has been the preferred approach of the scientific community in recent years. This approach enables an efficient imaging of the part and removes the need for wedges customized to the surface shape (Mark Sutcliffe et al., 2012; Zhang et al., 2014). Additionally, the adaptive ultrasonic phased array inspection methods require no prior knowledge of the surface profile of the specimen under inspection (Kerr et al., 2016; Matuda et al., 2019). On this approach, ultrasound transmission and imaging strategies had their capabilities demonstrated in the literature: the use of plane waves imaging methods (L Le Jeune, Robert, & Prada, 2016; Rachev et al., 2020), the real-time Dynamic Depth Full Focusing (Cruza, Camacho, Mateos, & Fritsch, 2019), the use of Virtual Source Apertures (Hoyle et al.,

2018) and the Total Focusing Method (TFM) (M. Sutcliffe et al., 2013). All which can be obtained through the post-processing of the Full Matrix Capture (FMC) (Holmes et al., 2005). Moreover, the TFM is of special interest due to its status of gold standard in terms of image quality (Camacho, Atehortua, Cruza, Brizuela, & Ealo, 2018). Nevertheless, the reliability of such inspections still demands further investigation. Strong artifacts were observed in the images of some cases, probably caused by the influence of the surface profile (Brown et al., 2017; Malkin et al., 2018; Zhang et al., 2014). Even when using the surface-adapted total focusing method (TFM), limitations were observed when imaging under sharp curvatures (Malkin et al., 2018).

In a rather complex scenario, it is not only the part's surface profile that will affect the outcome of the ultrasonic inspection, but also, a combination of all the parameters involved, such as the probe and material properties (Schmerr, 2015). Hence, it is fundamental that further works investigate how the aforementioned limitations and image artifacts arise from these combinations of parameters (e.g., curved profiles, probe aperture, standoff, etc.). Additionally, more importantly, investigations should be performed to determine how these parameters can be designed to avoid errors in the inspection.

In this context, this paper demonstrates how the performance of the phased array immersion inspection can be optimized based on the probe standoff, in combination with the part surface profile and flaw depth. Hence, a Probe Standoff Optimization Method (PSOM) is presented, which uses the point spread function (PSF) to calculate the best probe standoff prior to inspection. Throughout the paper, the total focusing method implemented through a dual-layer media has its resulting image quality verified and compared with the PSOM predictions. The aim is to verify if the PSOM predictions agree with the results of the experimental phased array imaging of parts with concave and convex top surfaces, as well as to confirm how the optimization process improves the imaging performance.

2.3 Materials and Methods

2.3.1 Total Focusing Method Imaging

The total focusing method (TFM) is a delay-and-sum imaging algorithm that uses the full matrix capture (FMC) data acquisition scheme. Delay functions allow us to synthetically focus on every point of a region of interest inside the inspected part (Holmes et al., 2005; Long, Russell, & Cawley, 2012). Figure 2-1 illustrates how the method is applied to the inspection of an immersed part having a surface profile described by *s(x)*.

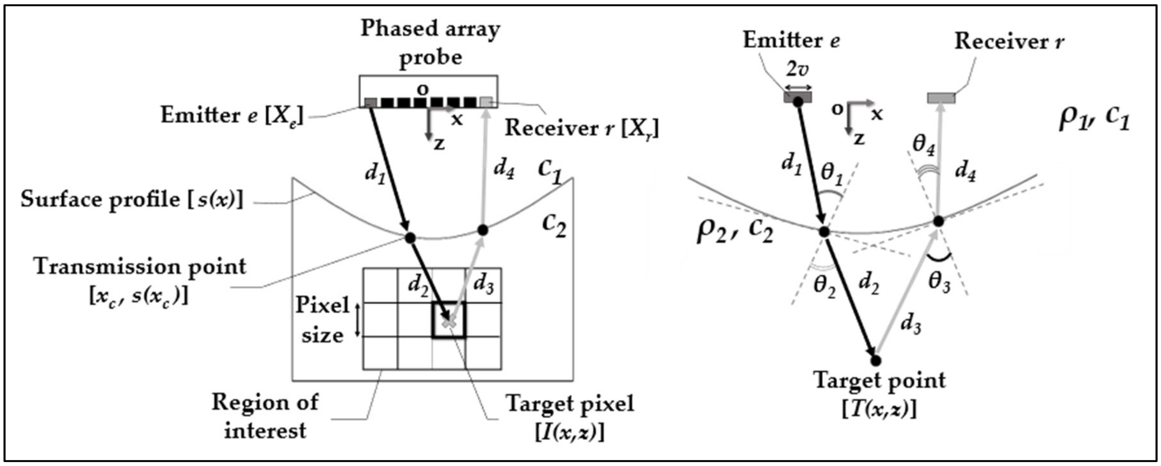
Phased array probe
o
x
z
Emitter e [X_e]
Receiver r [X_r]
d_1
d_4
c_1
c_2
Surface profile [s(x)]
Transmission point [x_c, s(x_c)]
Pixel size
d_2
d_3
Region of interest
Target pixel [I(x,z)]
Emitter e
2v
Receiver r
o
x
z
ρ_1, c_1
θ_4
d_4
d_1
θ_1
ρ_2, c_2
θ_2
d_2
θ_3
d_3
Target point [T(x,z)]

Figure 2-1 Schematic of the total focusing method applied to an immersed part with s(x) top surface profile. The waves travel from the emitter e to a pixel and then to the receiver r through the paths which respect the Fermat's principle. The same applies for a point reflector T(x,z), where paths d have different refraction angles for each combination of e and r

In this case, for probe elements *e* (emitter) and *r* (receiver), the target pixel *I(x,z)* in the region of interest has an amplitude given by the A-scan *S(e,r,t)* of the FMC data at the time advance $t = t_e + t_r$. Here, t_e is equal to the ultrasonic wave time-of-flight from *e* to *I(x,z)* and t_r is the time-of-flight from *I(x,z)* back to *r*. By summing all the combinations of elements acting as emitter–receiver *e* and *r*, the pixel amplitude can be written as:

$$I(x,z) = \left|\sum_{e}\sum_{r} S(e,r,t_e + t_r)\right|. \tag{2.1}$$

As there are two different wave propagation velocities c_1 and c_2 in each medium, refraction occurs. Consequently, the wave path from the element to the pixel is represented by two straight lines with distances d_1 and d_2 (or d_3 and d_4), as shown in Figure 2-1. Thus, the time-of-flight can be written as:

$$t_e = \frac{d_1}{c_1} + \frac{d_2}{c_2}\ ;\ t_r = \frac{d_4}{c_1} + \frac{d_3}{c_2}, \tag{2.2}$$

$$t_e = \frac{\sqrt{(x_c - X_e)^2 + (s(x_c))^2}}{c_1} + \frac{\sqrt{(x - x_c)^2 + (z - s(x_c))^2}}{c_2} \tag{2.3}$$

$$t_r = \frac{\sqrt{(x_c - X_r)^2 + (s(x_c))^2}}{c_1} + \frac{\sqrt{(x - x_c)^2 + (z - s(x_c))^2}}{c_2} \tag{2.4}$$

Nevertheless, to calculate the times-of-flight t_e and t_r, the correct paths should be selected based on the Fermat's principle. In practice, this task consists of finding the transmission point (x_c, $s(x_c)$), on the surface $s(x)$, that yields a stationary time-of-flight:

$$\frac{dt_e}{dx_c} = 0\ ;\ \frac{dt_r}{dx_c} = 0 \tag{2.5}$$

Moreover, the calculation of the times-of-flight for each pixel–element pair can be done only once since reciprocity is valid. That means that the time-of-flight from a pixel to an element is the same when it acts as an emitter or as a receiver. Throughout the paper, the surfaces were discretized using $\lambda_{water}/5$ between samples, and a grid search method was used to find, between all surface points, the one that satisfies the condition in eq. (2.5).

To image each specimen, an internal region of interest was discretized into a grid of pixels. In each case, the grid of points was centered relative to the target center in the x-direction. Finally, the spacing between each point on the grid, or the pixel resolution, was set to 0.2 x 0.2 mm.

2.3.2 Probe Standoff Optimization Method

The reliability of the ultrasonic phased array total focusing method (TFM) imaging of parts with curved geometries also depends on the probe standoff. This is because some combinations of surface profile and standoff interfere in the phased array focusing capacity. Therefore, strong artifacts arise, and resolution is lost in the imaging process, to the point that it is impossible to identify any defect indications with certainty. This paper, therefore, introduces a probe standoff optimization method (PSOM) to avoid these poor combinations. The main objective of the algorithm is to indicate the best probe standoff for a given set of curved surface geometry, defect location, probe and material parameters. Specifically, the algorithm improves the reliability of the imaging, ensuring the correct selection of standoff prior to the inspection. Moreover, it also may be used to predict the performance of the imaging. The imaging performance of an ultrasonic phased array may be predicted by the calculation of its point spread function (PSF). The PSF measures the array response to a point reflector (Drinkwater & Wilcox, 2006). This response is directly related to the phased array imaging performance. In an immersion inspection, the PSF is dependent on the array characteristics, media properties, interface shape and probe standoff. Therefore, the PSOM algorithm uses PSF characteristics to estimate the probe standoff that yields the optimal TFM image.

Many researchers have developed complete and accurate methods for the simulation of the array response, and hence the estimation of the PSF (Chiao & Thomas, 1994; Drinkwater & Wilcox, 2006; Lingvall, Olofsson, & Stepinski, 2003). Based on these methods, a simplified PSF calculation was conducted in the present study. Since the aim of the PSOM is to find the best PSF of the TFM imaging using a single wave mode, a full simulation is not needed. Moreover, this work applied a PSF calculation that takes advantage of the outputs of the TFM described in Section 2.3.1. Thus, the pulse response of a point target $T(x,z)$ inside the part is estimated by shifting and modifying a tone-burst, by using the probe parameters and the TFM outputs. This simplification results in a lower computational cost while maintaining a valid estimate of the system's PSF.

First, the probe parameters, surface profile *s(x)*, materials, point target *T(x,z)* and standoff must be defined. As shown in Figure 2-1, by applying the same TFM procedure described in Section 2.3.1, the paths from e to *T(x,z)* and to r are found. Then, the PSF estimation is based on the ray paths d_1, d_2, d_3, d_4, the angles θ_1, θ_2, θ_3, θ_4, and times-of-flight t_e and t_r. The times-of-flight t_e and t_r are used to shift a Dirac's delta function. This delta function is then used to delay a tone-burst *P[t]* by a convolution operation:

$$P[t] * \delta[t + t_e + t_r] = P[t + t_e + t_r]. \tag{2.6}$$

Throughout the paper, *P[t]* is a Hann windowed tone-burst with 4 cycles and centered at 5 MHz. The convolution of *P[t]* yields the signal response estimate *u(e,r,t)* for this element combination:

$$u(e, r, t) = P[t + t_e + t_r]. \tag{2.7}$$

Now, it is necessary to account for the signal attenuation due to element directivity, the divergence of the ultrasonic wave and the transmission loss due to impedance mismatch:

$$U(e, r, t) = u(e, r, t) \cdot G_e \cdot D_e \cdot T_e \cdot G_r \cdot D_r \cdot T_r\ , \tag{2.8}$$

where G_e is the geometric attenuation, D_e is the element directivity and T_e is the transmission coefficient in the emission and G_r is the geometric attenuation, D_r is the element directivity and T_r is the transmission coefficient in the reception (Schmerr, 2015), defined as:

$$G_e = \frac{1}{\sqrt{d_1 + d_2}};\ \ G_r = \frac{1}{\sqrt{d_3 + d_4}}, \tag{2.9}$$

$$D_e = sin\,c\left(\frac{2v\pi f}{c_1} \cdot sin(\theta_1)\right);\ D_r = sin\,c\left(\frac{2v\pi f}{c_1} \cdot sin(\theta_4)\right), \tag{2.10}$$

$$T_e = \frac{2\rho_2 c_2 \cdot \cos(\theta_1)}{\rho_1 c_1 \cdot \cos(\theta_2) + \rho_2 c_2 \cdot \cos(\theta_1)};\ \ T_r = \frac{2\rho_1 c_1 \cdot \cos(\theta_3)}{\rho_2 c_2 \cdot \cos(\theta_4) + \rho_1 c_1 \cdot \cos(\theta_3)}. \tag{2.11}$$

Here, $2v$ is the length of the piezo element and f is the central frequency of the probe. In addition, ρ_1 and c_1 are, respectively, the density and the longitudinal wave speed of the first medium, ρ_2 and c_2 the density and the longitudinal wave speed of the second medium.

With this calculation done for all possible combinations of emitter *e* and receiver *r*, the FMC due to the point target *T(x,z)* is estimated. Then, using the procedure described in Section 2.3.1, the times-of-flight of the pixels around the target are calculated. By using these values, *U(e,r,t)* is translated into a TFM image. The image intensity caused by a point reflector is the PSF of the imaging system:

$$PSF(x,z) = \left|\sum_e \sum_r U(e,r,t_e + t_r)\right| \tag{2.12}$$

Which is exemplified by Figure 2. Here, the power represents the image intensity at a given *(x,z)* point. The maximum intensity is found at the exact point target position *T(x,z)*. Moreover, since the lateral resolution is the scope of this analysis, the *PSF(x,z)* can be studied only at this *z* point, with it being reduced to *PSF(x)*. In the *PSF(x)*, as shown in Figure 2-2, the algorithm discriminates two important characteristics: the side lobe level (SLL) and the main lobe width (MLW). The SLL is found by a peak search method which looks for the highest value after the maximum in the *PSF(x)*. On the other hand, the MLW is found by the -6 dB drop method. The MLW is the distance $x_q - x_p$ between two points, where the *PSF(x)* is equal to the maximum subtracted by -6 dB:

$$PSF(x_q) = PSF(x_p) = Max - 6dB;\ MLW = x_q - x_p\,. \tag{2.13}$$

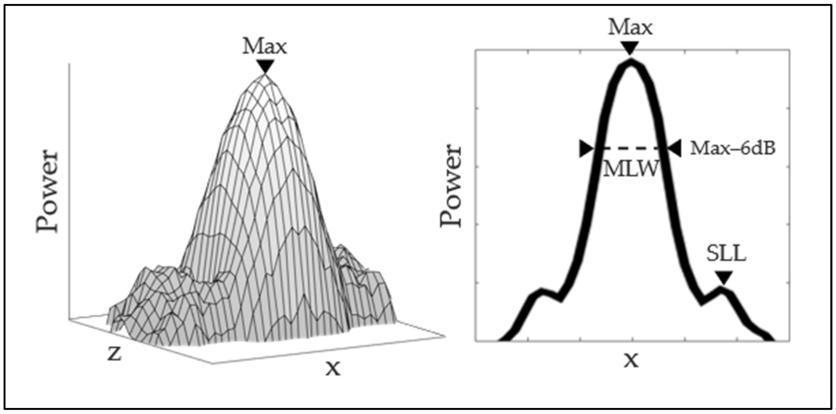

Figure 2-2 PSF example. The power represents the image intensity at a given point. *PSF(x)* is defined at *z*, where the power is maximum. Main lobe width and side lobe levels are found as illustrated

The reasoning behind the choice of these two parameters lies in the image formation. The sharpness and precision of the TFM synthetic focus, which is ultimately the PSF, define the TFM image quality. Since the image is a convolution of the real target and the PSF, the MLW gives an estimate of the lateral resolution, while the SLL indicates the level of aberrations in the image (Ilovitsh, Ilovitsh, & Ferrara, 2019). Hence, the PSOM algorithm searches for the best trade-off between the lateral resolution and the artifact level.

Now that the PSF calculation has been described, the flowchart of the algorithm is presented in Figure 2-3. The first step of the PSOM is to define all input parameters for the calculation. Then, having the standoff test range, the algorithm starts the PSF calculation at a given standoff, which is varied at each iteration. With the TFM procedure, the times-of-flight and path parameters are calculated. In the sequence, the FMC is estimated based on these values and then translated into the image of the *PSF(x,z)*. The peaks are found, and the SLL is calculated. The SLL is measured and verified to see if it is below the defined threshold, (-20 dB here), which was verified as an acceptable image quality. If the SLL is above the threshold, the standoff is varied. Otherwise, the MLW is measured. As such, the algorithm does not waste time computing the MLW for poor image candidates. After the last standoff is used in calculation, the algorithm chooses the standoff with the lower MLW as the optimal probe standoff. The algorithm was run for all experimental parameters described in the next section.

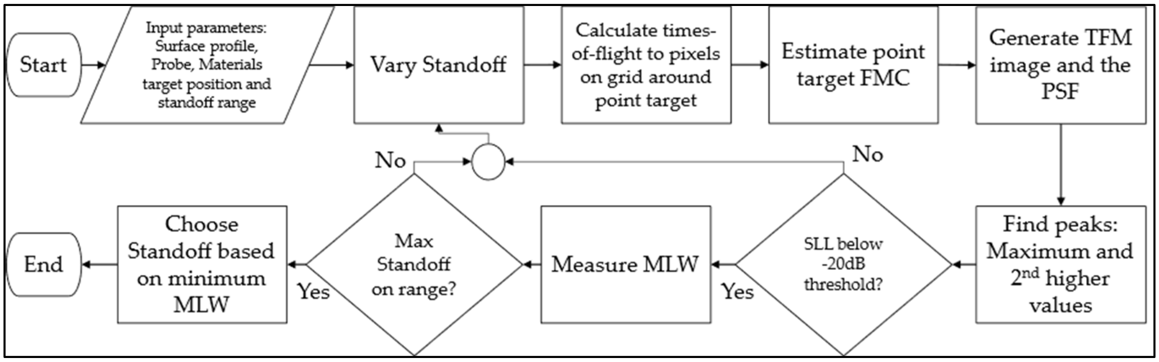
Start
Input parameters: Surface profile, Probe, Materials target position and standoff range
Vary Standoff
Calculate times-of-flight to pixels on grid around point target
Estimate point target FMC
Generate TFM image and the PSF
Find peaks: Maximum and 2nd higher values
SLL below -20dB threshold?
No
Yes
Measure MLW
Max Standoff on range?
No
Yes
Choose Standoff based on minimum MLW
End

Figure 2-3 Flowchart of the Probe Standoff Optimization Method algorithm. A *PSF(x)* calculation and discrimination are conducted to find the standoff with the best trade-off between the lateral resolution and the artifact level

2.3.3 Experimental Analysis

Experiments were carried out to verify the validity of the PSOM. First, a set of sinusoidal surface profiles was defined for the machined aluminum specimens. The sinusoidal shape was chosen to create a challenging variable wave incidence scenario, while maintaining a generic approach. Figure 2-4 presents a schematic of the specimens with sinusoidal top surfaces under immersion inspection. Here, the specimens were divided and named according to their surface curvature. The surfaces of the concave ones are described by:

$$s_{\cup}(x) = h - a + a \cdot \cos\left(\frac{\pi x}{b}\right);\ \{x \mid -{}^{b}/_{2} \leq x \leq {}^{b}/_{2}\}, \tag{2.14}$$

additionally, the convex surfaces were written as:

$$s_{\cap}(x) = h + a - a \cdot \cos\left(\frac{\pi x}{b}\right);\ \{x \mid -{}^{b}/_{2} \leq x \leq {}^{b}/_{2}\}, \tag{2.15}$$

where *h* is the probe standoff or water path, *a* is the surface cosine amplitude and *b* is the half-period of the cosine function, as shown in Figure 2-4.

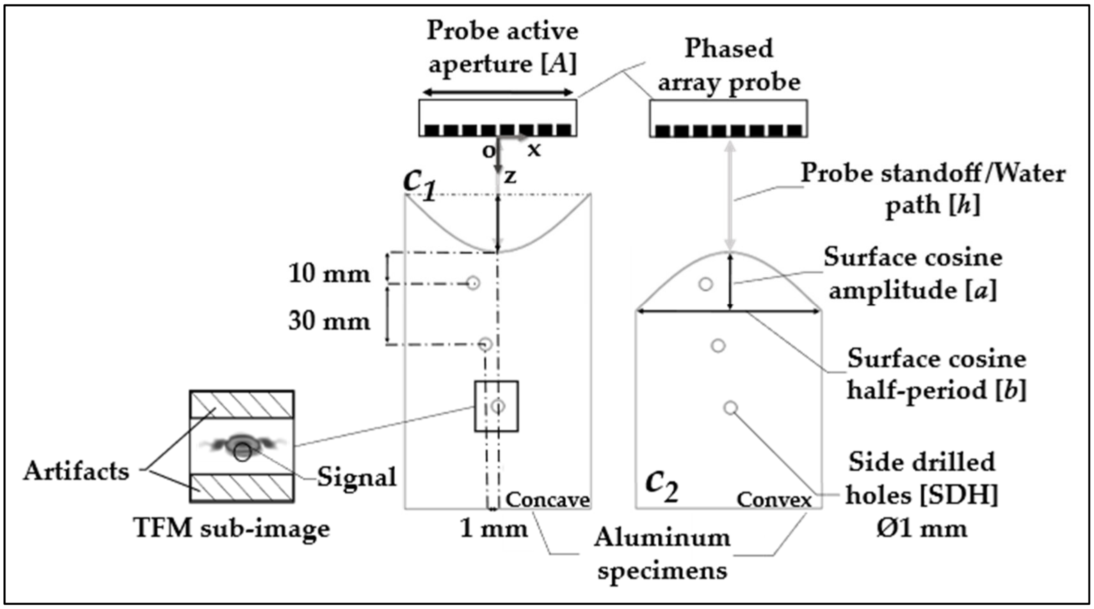
Probe active aperture [A]
Phased array probe
O
x
z
C1
Probe standoff/Water path [h]
10 mm
30 mm
Surface cosine amplitude [a]
Surface cosine half-period [b]
Artifacts
Signal
TFM sub-image
Concave
1 mm
C2
Convex
Aluminum specimens
Side drilled holes [SDH] Ø1 mm

Figure 2-4 Schematic of the sinusoidal concave and convex specimens inspected by immersion phased array ultrasonic testing. The probe is centered relative to the surface. Three SDH are positioned inside the specimens and are analyzed by the TFM sub-image shown

The specimen parameters, cosine amplitude *a,* half-period *b*, thickness *l* and probe standoff range *h*, are presented in Table 2-1. A flat surface was manufactured for the benchmark imaging, with two pairs of concave and convex surfaces to represent a weak and a strong curvature sharpness relative to the probe aperture. A set of cosine amplitudes *a* was chosen for this study, varying from zero λ_{Al}, representing a flat surface, to 15 λ_{Al}. Different curvatures enabled the analysis of how combinations of surface curvature and probe standoffs influence the inspection. The materials selected were water, for the immersion medium, and aluminum, for the specimen. The longitudinal wave velocity of the water c_1 and of the aluminum c_2 are written in Table 2-2, along with the material's respective densities ρ_1 and ρ_2. Here, λ_{Al} is the wavelength in the specimen material at the center frequency chosen for the inspection (5 MHz).

Table 2-1 Specimen surface curvature parameters and probe standoffs

Specimen	**Surface**	***a*** **(λ_{Al})**	***b*** **(mm)**	***l*** **(mm)**	***h*** **(mm)**
Cx15	Convex $s_\cap(x)$	15	60	60	{20, 30, …, 130}
Cx5	Convex $s_\cap(x)$	5	38.4		
F0	Flat $s_-(x)$	0	62		
Cc5	Concave $s_\cup(x)$	5	38.4		
Cc15	Concave $s_\cup(x)$	15	60		

With the surface profiles defined, the variation range of the probe standoff *h* was chosen. As shown in Table 2-1, *h* was varied, ranging between 20 and 130 mm, with a 10 mm step. Both the phased array probe and the specimen were centered relative to the origin O, as shown in Figure 2-4. It can be noted that *h* is defined as the distance in z from the center point of the transducer to the center of the surface profile. This ensured approximately the same propagation distance from the probe to the subsurface flaws for both concave and convex specimens.

Table 2-2 Probe and material parameters

Aperture A (mm)	**Frequency f (MHz)**	**Pitch (mm)**	**2v (mm)**
38.4	5	0.6	0.55
λ_{Al} (mm)	**Elevation (mm)**	**Bandwidth**	**Element count**
1.27	10	83%	64
c_1 (m/s)	**ρ_1 (g/cm^3)**	**c_2 (m/s)**	**ρ_2 (g/cm^3)**
1480	1	6470	2.77

In this study, the side-drilled holes were positioned within the specimens according to the schematics presented in Figure 2-4. Three side-drilled holes (SDH) with a diameter of 1 mm were selected as the inspection targets. The size of the flaws was designed to be smaller than λ_{Al} at 5 MHz, but still above the theoretical sizing limit of a half-wavelength. In addition, different defect depths, ranging from 10 to 70 mm, were designed to evaluate the effect of the surface shape on penetration loss. Finally, the defects were laterally offset by 1 mm between one another to avoid shadowing.

As can be seen in Figure 2-5, the experimental setup comprised a Verasonics Vantage 64 LE array controller and a 64-element 5 MHz Olympus 5L64I phased array probe. The parameters of the latter are shown in Table 2-2. For each specimen, the setup was assembled using 3D-printed plastic holders and an aluminum plate with holes. This setup worked as a standard to fasten both the specimen and the phased array transducer in the correct centered positions and *h* range.

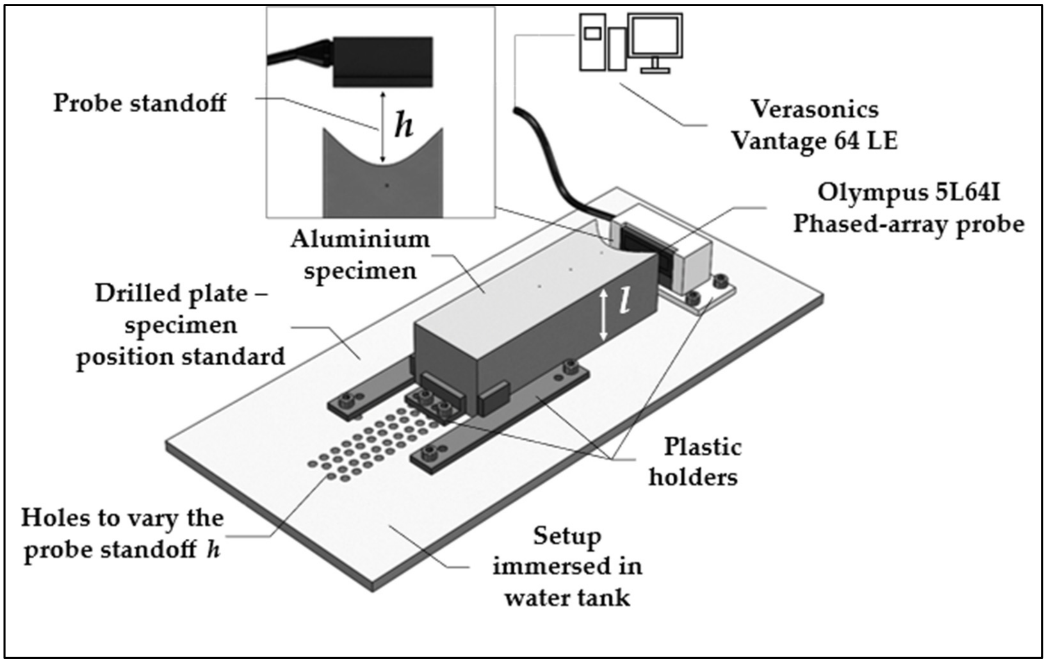
Probe standoff
h
Verasonics
Vantage 64 LE
Olympus 5L64I
Phased-array probe
Aluminium
specimen
Drilled plate –
specimen
position standard
l
Plastic
holders
Holes to vary the
probe standoff h
Setup
immersed in
water tank

Figure 2-5 Schematic of the experimental setup used to validate the optimization calculations. The setup was assembled using 3D-printed plastic holders

With the assembled setup immersed in a water tank, FMC were acquired for all probe standoffs h. The standoff was increased by changing the position of the specimen's holder to a lower hole on the aluminum plate, as shown in Figure 2-5. A 25-volt four-cycle Hann windowed burst centered at 5 MHz was used as the input signal. Acquisition was done at a sampling frequency of 62.5 MHz and 30 averages were performed. In addition, a bandpass filter with cut-off frequencies of 3 and 7 MHz was applied to the resulting time traces. All the FMC data was extracted and post-processed on an TFM algorithm written in Matlab®.

2.3.4 Data Post-Processing and Metrics

The FMC data was post-processed using the total focusing method (TFM) procedure described in Section 2.3.1. In this case, the image reconstruction using the TFM accounted for the known surface profiles and did not require their prior identification. This assumption was made because this work aims to investigate the isolated effect of the surface profile and the probe standoff on imaging. A quantitative analysis of the TFM images was then carried out, with a separate analysis conducted for each SDH, as in in Figure 2-4. Two metrics were selected to evaluate the images: the signal-to-artifact ratio (SAR) and the array performance indicator (API) (Holmes et al., 2005).

The TFM images were generated using the longitudinal mode and accounting only for direct paths. Hence, the reflection coming from the top face of the side-drilled holes is the stronger indication expected in the images. However, due to the curvatures on the surfaces, a loss of coherence and focusing capacity may occur, thus creating image aberrations and making it hard to identify defects. For this reason, the SAR was introduced as a metric to measure the level of these image artifacts, accounting for changes in the reflector amplitude relative to the level of aberrations. For each reflector, the sub-image area was divided into two regions, one containing the signal and the other, the possible surrounding artifacts, as shown in Figure 2-4.

This region was selected large enough to contain the echoes from the longitudinal waves reflecting on the top or internal surfaces of the SDH and possible creep waves. The maximum amplitude value I_{max} in the signal region represents the signal on the SAR calculation in eq. 2.16. Consequently, the remaining pixels in the sub-image area represent the control region for the level of artifacts, as shown by the hatched region in Figure 2-4. These pixels have an intensity $I_{artifacts}$. In the experiments, random and structural noises are present, which reduces the SAR. The SAR was calculated by taking the I_{max} and dividing it by the root mean square of $I_{artifacts}$. This ratio was put on a decibel scale to yield the SAR:

$$SAR = 20 \log_{10}\left(\frac{I_{max}}{\sqrt{<I^2_{\text{artifacts}}>}}\right) \tag{2.16}$$

On the other hand, the API was chosen to evaluate how the lateral resolving capacity of the imaging system would be affected by the combination of inspection parameters. The pixels (I_{-6dB}), with intensities equal to the maximum and up to 6 dB below the maximum intensity (I_{max} – 6 dB $\leq I_{-6dB} \leq I_{max}$), were considered as the area A_{-6dB} of the reflector in the image. Hence, the number of pixels within this range multiplied by the image resolution of 0.2 x 0.2 mm yielded the area size A_{-6dB}. The API was calculated for each sub-image using eq. 2.17. For each case, the ratio between the area (A_{-6dB}) and the square of the wavelength ($\lambda^2_{\mathrm{Aluminum}}$) was calculated:

$$API = \frac{A_{-6dB}}{\lambda_{Al}^{2}} \tag{2.17}$$

2.4 PSOM and Experimental Results

First, some numerical predictions are presented through the PSFs generated using the PSOM. Figure 2-6 contain the PSF comparison between different surfaces and standoffs for the SDH positioned 10 mm deep into the parts. It is shown how the PSF behaves in the two extremes of the range, *h* = 20 and 130 mm, for the F0 specimen in Figure 2-6(a) and for the Cx15 specimen in Figure 2-6(b). Additionally, in Figure 2-6(c), the PSF is shown for the Cc15 specimen at *h* = 40 and at 100 mm standoffs to illustrate a poor and a high imaging performance.

Little variation is observed in Figure 2-6(a) for the F0 specimen, with a slight increase in MLW and reduction in SLL. However, since the SLL is below -20 dB, no imaging artifacts will appear in the imaging. On the other hand, the Cx15 specimen, Figure 2-6(b), presents a large MLW increase over the same range. While the performance is comparable to the F0 benchmark at *h* = 20 mm, the loss of lateral resolution is latent at the 130 mm standoff. Finally, the Cc15 in Figure 2-6(c) presents a different behavior. At the 40 mm standoff, the SLL is as high as -9 dB, which indicates a very poor focus. Consequently, it is expected that the image of a reflector would be greatly compromised by artifacts. Meanwhile, at *h* = 100 mm, the SLL drops to -22 dB, indicating a much better focus definition.

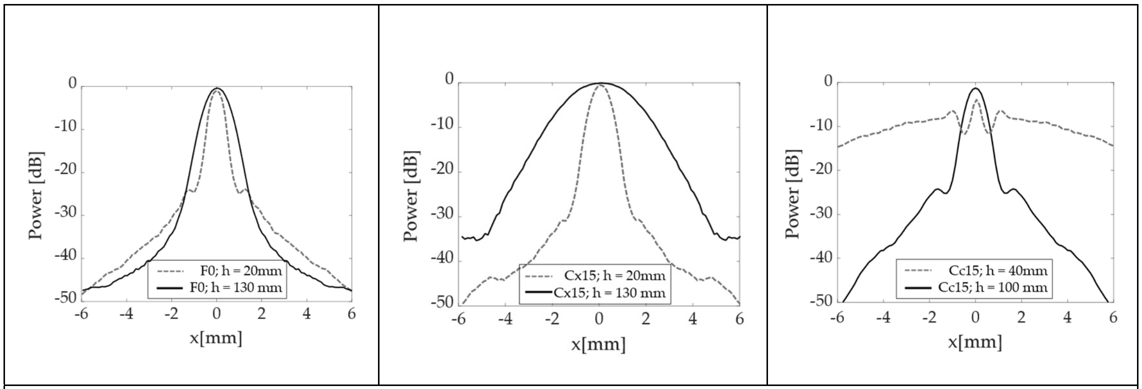

(**a**) (**b**) (**c**)

Figure 2-6 PSF(x) calculated for a target positioned 10 mm deep inside the parts: (**a**) Flat specimen F0 at two probe standoffs *h* = 20 and 130 mm; (**b**) Convex specimen Cx15 at two probe standoffs *h* = 20 and 130 mm; (**c**) Concave specimen Cc15 at two probe standoffs *h* = 40 and 100 mm

In the following, the SLL and MLW are plotted as a function of all probe standoffs *h*, respectively, in Figure 2-7(a) and (b), Figure 2-8(a) and (b), Figure 2-9(a) and (b). Although the algorithm does not compute the MLW below the -20 dB threshold, it is still presented as a way of verifying the agreement between the PSF and the experimental TFM images. Figure 2-7 contains the results for the SDH positioned at 10 mm inside the part, while Figure 2-8 and Figure 2-9 contain the results for the 40 and 70 mm deep SDHs. A dotted line is used to show the SLL threshold at -20 dB in all SLL plotting. In all the graphs, the results are overlayed for all specimens tested as in Table 2-1, as follows: Concave (Cc5 and Cc15), Convex (Cx5 and Cx15) and Flat (F0). Finally, the numbers I (Cx15), II (Cx5), III (Cc5) and IV (Cc15) are used to indicate the values of SLL and MLW of the optimal probe standoff selected by the PSOM. The PSOM algorithm run time on Matlab® 2021a for each combination of flaw position and surface profile was approximately 400 s, considering 12 different probe standoffs. The setup used for these computations had 32 Gb of RAM and an Intel® Core™ i7- 8086k CPU @4.00GHz.

To verify these predictions, the results of the validation experiments are also presented in Figure 2-7(c), Figure 2-8(c) and Figure 2-9(c), where the TFM images of the side-drilled holes are composed into matrices. In these TFM matrices, the top surface shape, referenced by the specimen number in Table 2-1, is identified in the vertical axis and the probe standoff *h* varies along the horizontal axis. In addition, the TFM images of a specimen with a flat top surface are plotted on the middle line, to serve as the image quality standard. The black circles in the middle of each image represent the real side-drilled hole position and size. Again, each matrix, from Figure 2-7 to Figure 2-9, refers to each defect depth studied. Consistently, the same numbers I, II, III and IV refer to the optimal probe standoff in the TFM image grid. It is important to mention that the probe standoff *h* = 20 mm was suppressed for the defects at 70 mm, due to the interference of the front-wall reflections.

The quality of the qualitative TFM images shown is described by the graphs presented in Figure 2-7(d) and (e) to Figure 2-9(d) and (e). The SAR and the API are presented as a function of the probe standoff *h* for the Concave (Cc5 and Cc15), Convex (Cx5 and Cx15) and Flat (F0) top surfaces studied. The SAR is plotted in Figure 2-7(d) to Figure 2-9(d). Similarly, Figure 2-7(e) to Figure 2-9(e) show the API. Again, the optimal probe standoff values of SAR and API are indicated by the numbers I, II, III and IV.

A good agreement is observed as the behavior predicted by the *PSF(x)* estimation is repeated in the experiments. In each case, from Figure 2-7 to Figure 2-9, the TFM images of the flat benchmark F0, and their SARs and APIs, are practically constant for most standoffs *h* analyzed. Meanwhile, the convex and concave cases each present a different behavior as a function of the change of the probe position relative to the surface.

Analyzing the images from defects under the Cx5 and Cx15 surfaces in Figure 2-7(c) to Figure 2-9(c), the area of pixels with intensities between 0 and -6 dB (A_{-6dB}) gets larger as the standoff *h* increases. Quantitatively, the graphs in Figure 2-7(d) and (e) to Figure 2-9(d) and (e) demonstrate a consistent SAR drop and an API increase as a function of an increase in the standoff *h*, for all defect depths, in the case of convex top surfaces. This confirms the *PSF(x)* trends of MLW increasing with *h*. Therefore, the PSOM indicates the minimum standoff in all convex cases, where SLL is below the threshold and the MLW is minimized. At the standoffs I and II, the SAR is maximum, and the API is minimum.

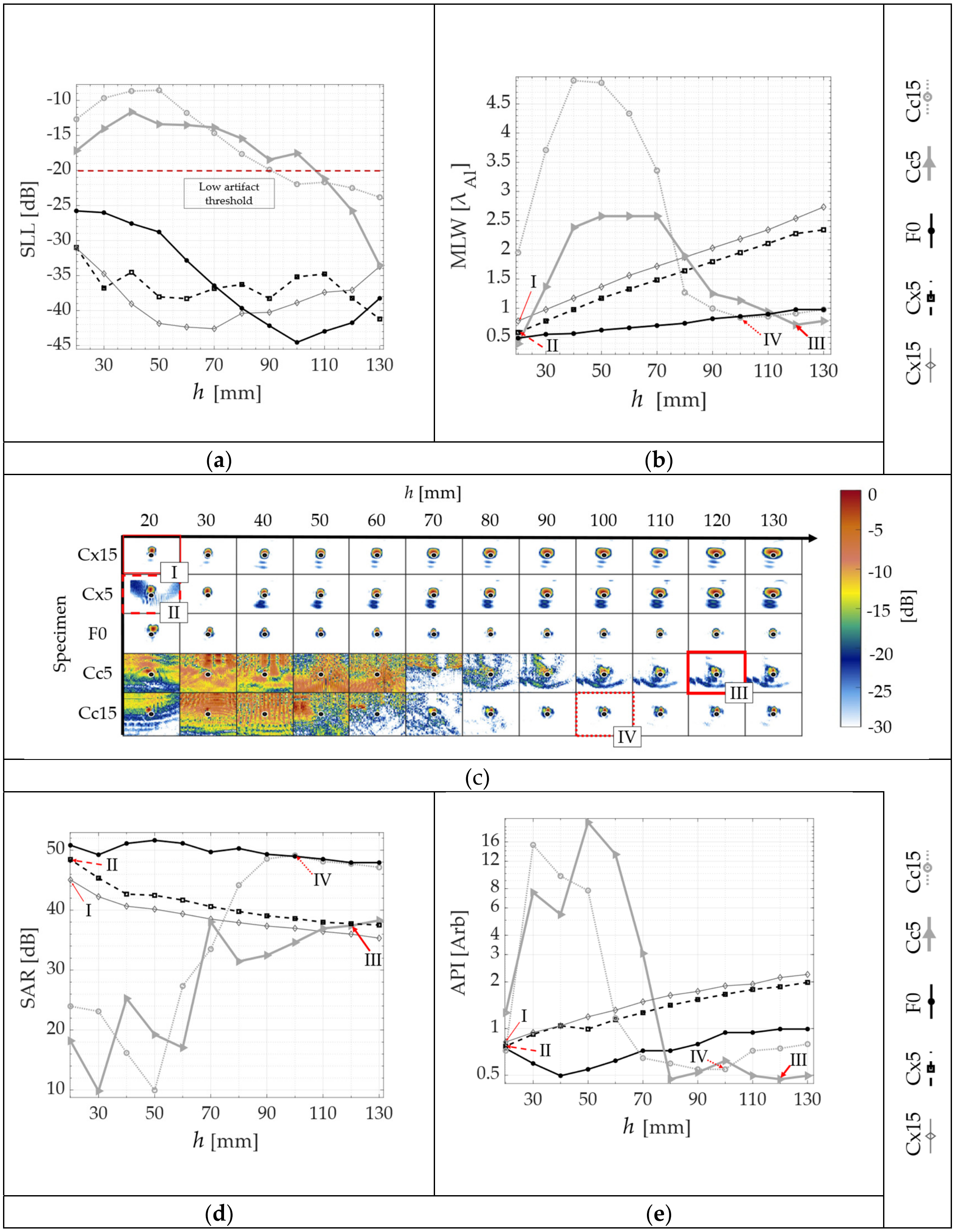

Figure 2-7 PSOM and experimental results from the SDH at 10 mm depth inside each specimen: (**a**) SLL obtained from *PSF(x)* at each standoff *h*; (**b**) MLW versus *h*; (**c**) TFM images at different probe standoffs *h* in each of the five specimens; (**d**) SAR versus standoff; (**e**) API versus standoff. The numbers I, II, III and IV indicate the optimal probe standoffs selected by the PSOM

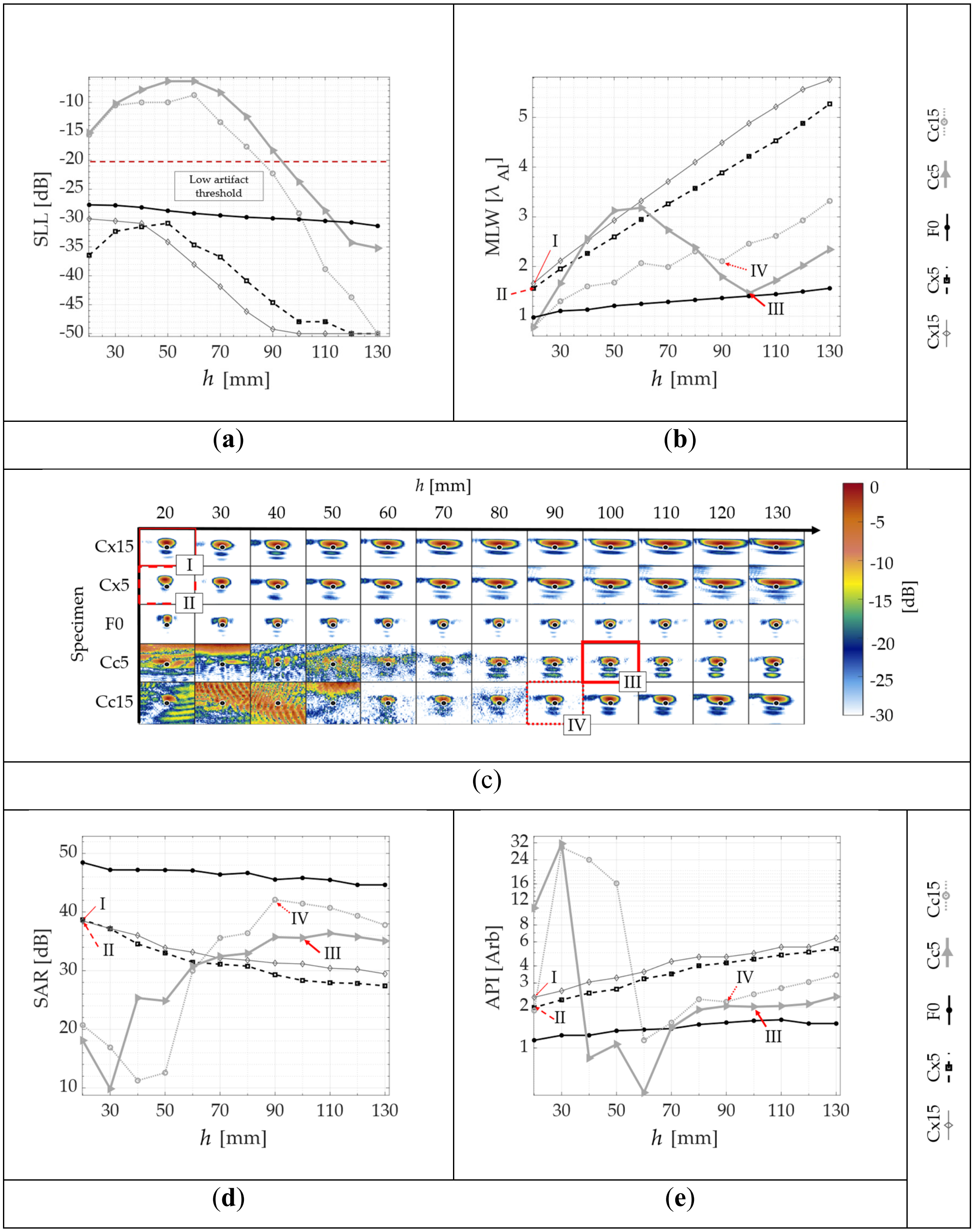

Figure 2-8 PSOM and experimental results from the SDH at 40 mm depth inside each specimen: (**a**) SLL obtained from *PSF(x)* at each standoff *h*; (**b**) MLW versus *h*; (**c**) TFM images at different probe standoffs *h* in each of the five specimens; (**d**) SAR versus standoff; (**e**) API versus standoff. The numbers I, II, III and IV indicate the optimal probe standoffs selected by the PSOM

Furthermore, the images generated below the Cc5 and Cc15 profiles, presented in Figure 2-7(c) to Figure 2-9(c), show a different behavior. The TFM images are full of reconstruction artifacts at certain probe standoffs *h*. At these probe positions, it becomes impossible to identify the presence of the reflector inside the specimen. The SLL verified from Figure 2-7(a) to Figure 2-9(a) agree with the TFM results, being above the threshold for all these standoffs. Hence, the PSOM discarded these standoffs, and based on the minimum MLW, selected the optimal standoffs III and IV in all defect depths. At the optimal points III and IV, the SAR and the API have values consistent with the trade-off between the resolution and artifact level. In some cases, the maximum SAR occurs for an also high API, and, therefore, a lower resolution is chosen while keeping the artifact level in the image low.

Finally, the images presented in Figure 2-10(a) to (c) present a comparison to verify the overall performance of the PSOM for the three side drilled holes. In these TFM images, the surface profile reconstructed through the imaging process is shown for reference. The amplitude of all three images was normalized by the front wall amplitude in Figure 2-10(c), which contains the image of the flat specimen benchmark F0. In all Figure 2-10(a) to (c), the black circles represent the real size and positions of the SDHs. Figure 2-10(a) contains the TFM image of the concave specimen Cc15 at the probe standoff $h = 40$ mm. Additionally, in Figure 2-10(a), strong artifacts are present blurring the image, which makes it impossible to identify any indications of the internal flaws. However, in Figure 2-10(b), the TFM of the same specimen Cc15 was reconstructed using the PSOM for each flaw. When using the PSOM, all three flaws have their indications resolved in the image, similarly to what is observed in the flat benchmark in Figure 2-10(c). This illustrates the relevance of the algorithm and the design of the optimal probe standoff. The flaw resolving capacity of the TFM applied to curved specimens is directly related to the optimization process proposed.

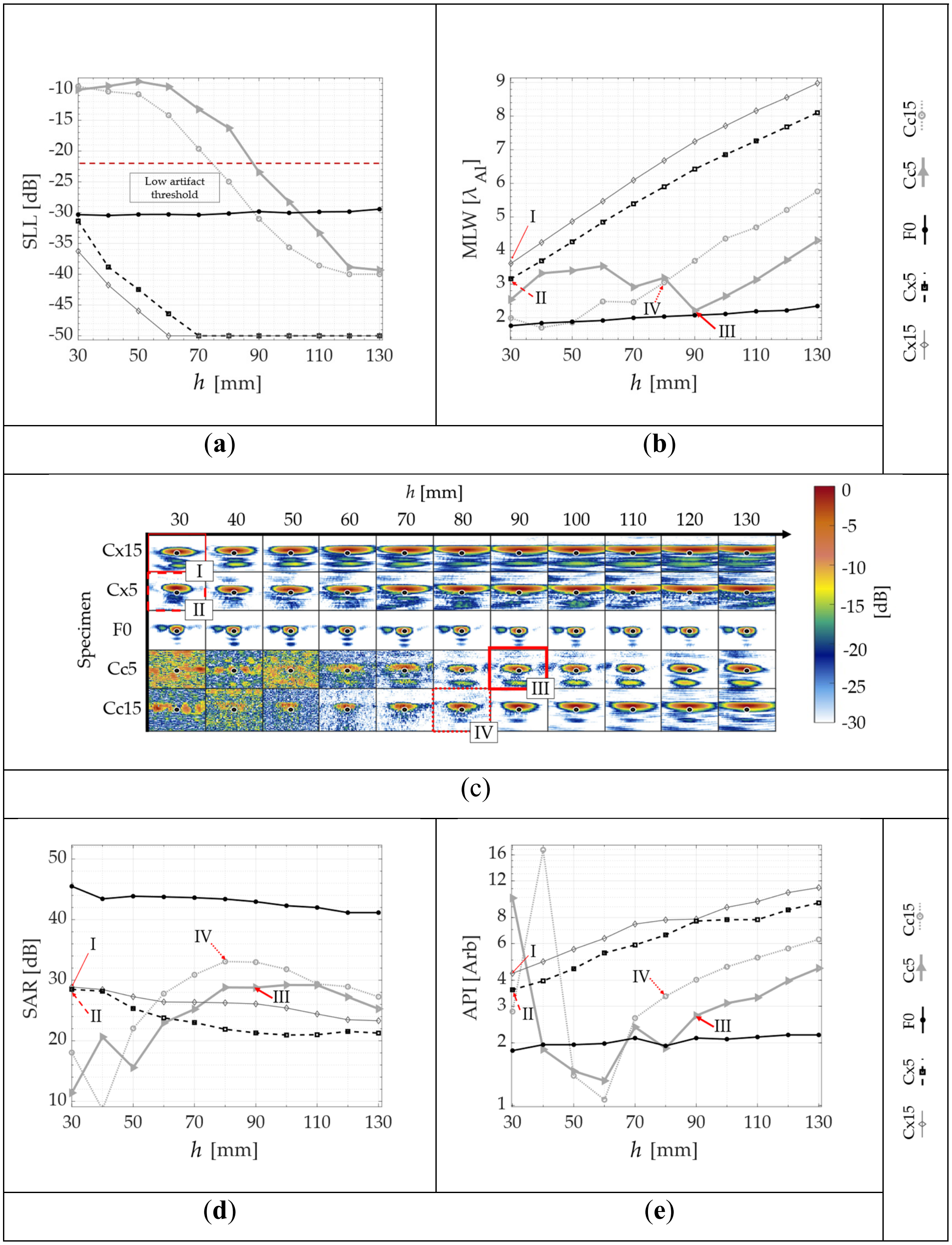

(**a**) (**b**)

(c)

(**d**) (**e**)

Figure 2-9 PSOM and experimental results from the SDH at 70 mm depth inside each specimen: (**a**) SLL obtained from *PSF(x)* at each standoff *h*; (**b**) MLW versus *h*; (**c**) TFM images at different probe standoffs *h* in each of the five specimens; (**d**) SAR versus standoff; (**e**) API versus standoff. The numbers I, II, III and IV indicate the optimal probe standoffs selected by the PSOM

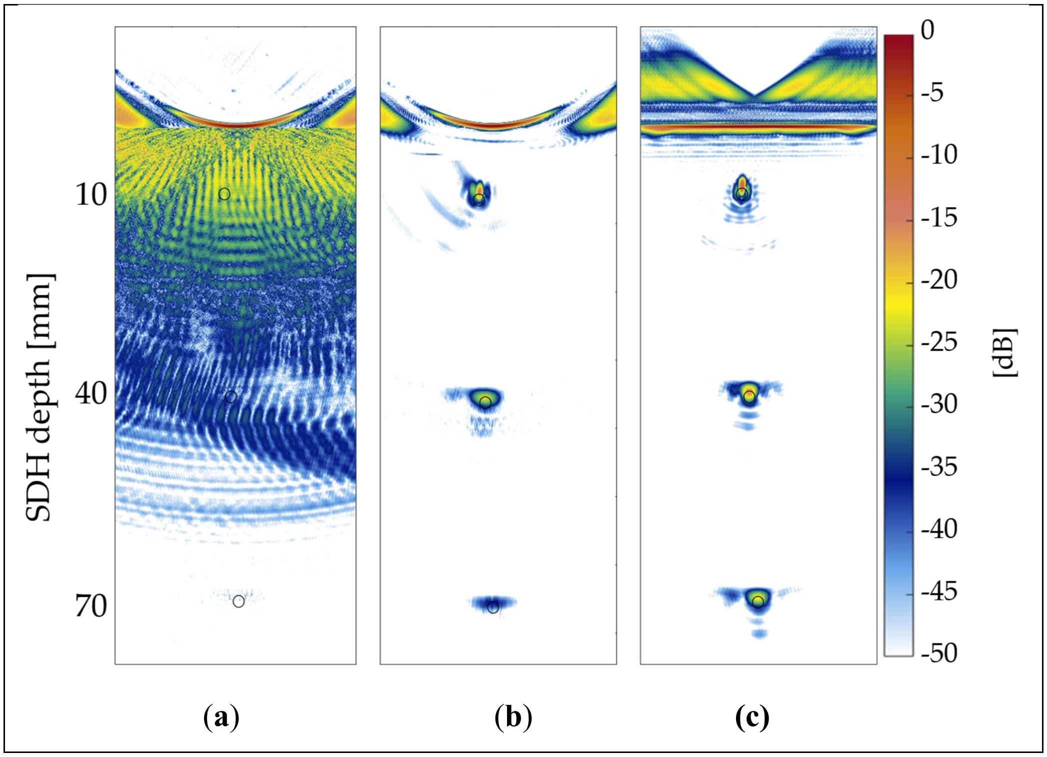

Figure 2-10 TFM image of the three side drilled holes and the specimens' surfaces: (**a**) Concave specimen Cc15 at the probe standoff *h* = 40 mm; (**b**) Concave specimen Cc15 with the PSOM applied to each flaw; (**c**) Benchmark flat specimen F0 at the probe standoff *h* = 40 mm

2.5 Discussion

The explanation behind the results obtained resides in the nature of the TFM. This imaging method is a synthetic focusing procedure that beamforms the FMC signal into fully focused images. This means the phased array is delayed to focus on every point in a region of interest. Thus, the image quality depends on the physical capacity of the array to generate a focus inside the specimen. In an immersion setup, this focus will be influenced by the curvature of the interface and its distance from the probe. In the case of curved surfaces, the interface will act as a lens, changing the focus shape. Moreover, even though the algorithm forces the focusing to occur on a given point, physically, the directivity of the probe elements limits the capacity of the array to generate a sharp focus.

Ultimately, to focus on a given point, the waves will sometimes travel through paths with angles of refraction that are in directions of low emission/reception power on the probe. That is exactly what the PSOM ultimately accounts for: the effect of varying the wave paths and angles of refraction on the focus capacity. The imaging quality will be determined by the SLL levels and the resolution by the MLW. The optimization algorithm selects the standoff that generates a focus with a low SLL and minimizes the MLW, and these two parameters are directly related to the image quality metrics, API and SAR. The SLL indicates the level of lateral lobes in the focus that cause artifacts, and finally, the level of SAR, while the MLW indicates the resolution of the focus for a single point, and, therefore, is directly related to the API in the TFM images. The latter is confirmed by the results, which show that the imaging performance strongly depends on the top surface curvature, the defect position, and most importantly, the probe standoff.

In each case, from Figure 2-7 to Figure 2-9, the TFM images of the flat benchmark, as well as their SARs and APIs, present negligible variations when compared to the images of curved parts. The present study demonstrated that the TFM imaging of defects inside concave parts Cc5 and Cc15 achieves a better performance at an optimal probe standoff *h*. This can be found prior to the inspection using the presented PSOM. In the case of Figure 2-7, at the optimal *h* indicated by IV, the image SAR gained 33 dB when compared to a poor standoff. If the PSOM is not applied, the strong image artifacts that occur at some standoffs and concave surface curvature combinations will make it impossible to identify defects. Additionally, the best trade-off between the resolution and image quality was obtained using the proposed method. This means that the optimal standoff presented the maximum SAR at the cost of a slightly increased API. After the optimal standoff, the API has an ascending tendency while the SAR values drop. It is important to note that depending on the application, the standoff selection criteria may be modified, favoring lateral resolution for cases with close defects or favoring SAR for highly attenuating materials.

Additionally, from the results, it is verified that the TFM images of convex Cx5 and Cx15 specimens lose performance as the standoff is increased. This agrees with the *PSF* prediction, where the MLW demonstrates how the focal point loses lateral resolution with an increase in the standoff. Hence, the PSOM indicates the standoff with the minimum MLW for all convex cases, since the SLL was lower than the threshold. For example, in Figure 2-9, the optimal standoff I presents an API slightly above 4, which is higher than the benchmark of 2, showing the influence of the curvature on the loss of resolution. Still, if a standoff of 130 mm is used, the Cx15 will have a drop in resolution of about 11 API. Finally, Figure 2-10(a) to (c) illustrated the relevance of the algorithm and the importance of designing the optimal probe standoff. Without the PSOM, the flaw identification reliability of the TFM on curved specimens becomes compromised.

2.6 Conclusion

This study demonstrated how the performance of the phased array immersion inspection could be optimized based on the probe standoff, using an optimization method (PSOM). The PSOM capacity to calculate the best probe standoff was verified through the good agreement between its predictions and the results of the experimental phased array imaging of parts with concave and convex top surfaces. The results confirmed that the optimization process greatly improves the imaging performance of curved parts.

The TFM imaging of defects inside concave and convex sinusoidal parts achieved a better performance at an optimal probe standoff h. In the case of concave parts, the PSOM ensured the selection of an optimal standoff, which avoids the appearance of strong artifacts while keeping a good lateral resolution. In the case of convex parts, a simpler scenario was found by the PSOM, where the best standoff was the minimum without front-wall second reflections.

Nevertheless, it must be noted that the ultrasound penetration and performance suffer due to the surface profile, and that the inspection depth and image quality are reduced accordingly. Future work must focus on the calibration issues caused by the curved surface because of the variability of the imaging performance. For example, the algorithm may be used as a fast tool to predict the resolution based on the surface profile. In addition, this work analyzed convex and concave surfaces separately. However, in real applications, it is common to find complex surfaces formed of combinations of concave and convex curvatures. Therefore, future works should investigate the validity of the PSOM algorithm for such surfaces.

Author Contributions: J.F.M.R. F.: conceptualization, methodology, software, validation, formal analysis, investigation, visualization, writing—original draft. P.B.: conceptualization, resources, writing—review and editing, supervision, funding acquisition.

Funding: This research received no external funding.

Data Availability Statement: Data and codes used in this study are openly available at https://pulets.ca/open-data/sensors-1394212

Acknowledgments: This work was supported by the NSERC CREATE oN-DuTy program.

Conflicts of Interest: The authors declare no conflicts of interest.

CHAPTER 3

A BEAMFORMING STRATEGY TO IMPROVE THE ULTRASONIC PHASED ARRAY INSPECTION BELOW CONCAVE SURFACES

J. F. Mansur Rodrigues Filho and P. Bélanger

Department of Mechanical Engineering, École de Technologie Supérieure,
1100 Notre-Dame West, Montreal, Quebec, Canada H3C 1K3

Paper published in *Canadian Institute for Non-Destructive Evaluation (CINDE) Journal*,
January 2022

3.1 Abstract

Parts with concave surfaces are especially difficult to inspect using ultrasound. This interface distorts the ultrasonic beam leading to image artefacts and poor ultrasound penetration. In this context, the present work demonstrates how to enhance the transmission of ultrasonic waves through concave surfaces. The proposed method consists of a beamforming strategy that compensates the refraction by using sub-apertures to focus on points on the specimen's surface. An aluminum specimen with a sinusoidal concave top surface was analyzed using a 64-element phased array in an immersion tank. On average, the beam computation showed a gain of 12 dB per transmission when the strategy proposed was compared to the Full Matrix Capture (FMC). Also, the Total Focusing Method (TFM) image quality of the proposed emission strategy was verified. The imaging of a side drilled hole (SDH) of 1 mm in diameter presented an improvement of approximately 11 dB in signal-to-noise ratio. Finally, fewer transmission events than the FMC were necessary to achieve a better TFM quality.

KEYWORDS: Phased array, TFM, FMC, Beamforming

3.2 Introduction

Through the last decades, researchers have demonstrated that immersion phased array ultrasonic testing can identify defects under curved surfaces (Cruza et al., 2019; M. Sutcliffe et al., 2013). However, these curved surfaces may cause imaging errors resulting in poor performances, thus compromising the reliability of the inspection. This type of interface distorts the ultrasonic beam in such way that can lead to image artefacts and poor ultrasound penetration. Hence, further developments are needed since the NDE of non-flat components is fundamental for condition assessment of composites, forgings, castings, and more recently the 3D printed metals. By using multi-element probes (Long et al.), the ultrasonic inspection can generate fully focused subsurface images of curved components. However, even high-quality image rendering algorithms such as the TFM (Holmes et al., 2005) suffer from the effects of concave interfaces.

The ultrasound penetration is lower on this type of interface. When compared to a flat interface, a considerable amount of the incident waves will encounter angles beyond the critical angle. Which reduces the coverage, resulting in a lower signal-to-noise ratio. Also, mode conversion is more likely to occur, causing image reconstruction artefacts. Therefore, this work proposes a beamforming strategy to mitigate these negative effects and improve the image quality. The method consists of a beamforming strategy that uses sub-apertures to focus on certain points of the interface. These points are selected in such way that the angle of incidence allows for maximum ultrasound penetration. In the following sections, the details of how this method improves the imaging, along with the experimental setup and results are presented.

3.3 Proposed beamforming strategy

Here, the developed strategy to enhance wave transmission through concave surfaces is presented. The proposed method is schematized in Figure 3-1. In the FMC scheme (Holmes et al., 2005; Long et al., 2012), for each transmission event, a single element emits an ultrasound beam through the surface. In the case of a flat interface (Figure 3-1 (a)), higher pressure is transmitted when compared to the same region below a concave interface (Figure 3-1 (b)). By taking the same element (Figure 3-1 (b)), the beam will not penetrate the same region below the concave interface because of the incidence angle. Instead, another element will insonify this area. However, with a weaker portion of its beam, due to element directivity. This lack of energy is detrimental to the resulting image. Hence, the idea of this method is to increase the energy in the refracted direction. To increase the penetration and favor the transmission, a sub-aperture of elements is used (Figure 3-1 (c)). Then, delays are applied to focus on the surface entrance point (Figure 3-1 (c)). As a result, improved pressure and beam shape are generated to cover the region of interest. Finally, as in the FMC, several sub-apertures can be used as individual transmission events, each focusing on a distinct surface point.

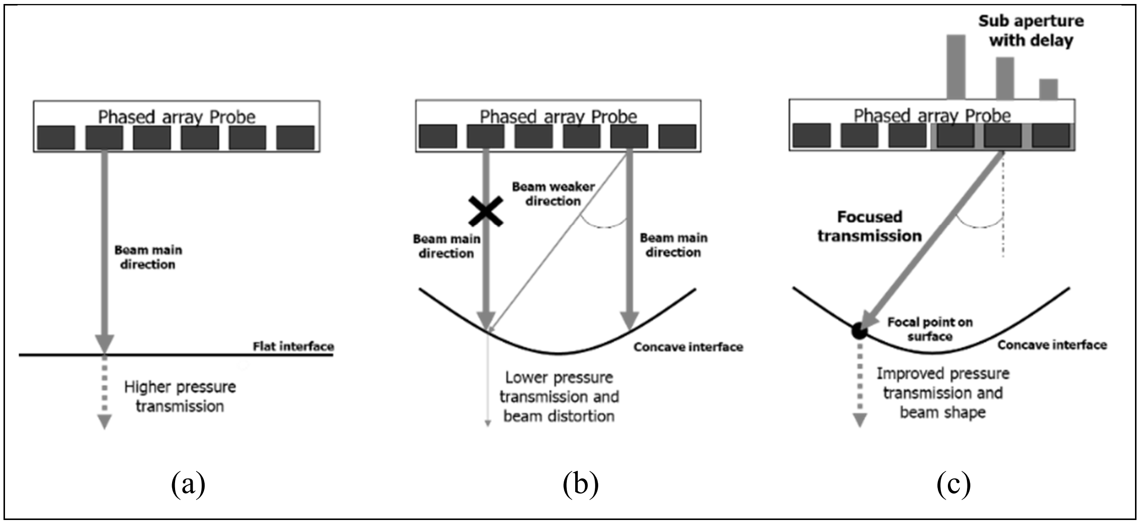
Phased array Probe
Beam main direction
Flat interface
Higher pressure transmission
Phased array Probe
Beam weaker direction
Beam main direction
Beam main direction
Concave interface
Lower pressure transmission and beam distortion
Sub aperture with delay
Phased array Probe
Focused transmission
Focal point on surface
Concave interface
Improved pressure transmission and beam shape
(a)
(b)
(c)

Figure 3-1 Scheme of proposed beamforming strategy; (a) Single element transmission on flat part; (b) Single element transmission on concave part; (c) Proposed beamforming on concave part

3.4 Experimental setup and results

The experimental setup is presented in Figure 3-2(a). An aluminum specimen with a sinusoidal concave top surface with an amplitude of 15 λ_{Al} was used for the immersion inspection analysis. The TFM quality of each emission strategy was verified in terms of the signal-to-noise ratio (SNR) by imaging a side drilled hole (SDH) of 1 mm in diameter. The SNR was calculated as described in the Fig 2(a), by dividing the maximum pixel intensity on the defect location by the rms of the noise far from the defect. The experimental setup comprised a

Verasonics Vantage 64 LE array controller and a 5L64 Olympus phased array probe. As a basis for comparison, the beam of each single element transmission, as in a full matrix capture (FMC) scheme, was analyzed for a 64-element phased array centered at 5 MHz. CIVA simulations were used to compute the beam pattern generated inside the part. Then, to verify the proposed method, the analysis of the beam generated by each sub-aperture of eight elements, focusing on a specific surface point, was done. The results in Figure 3-2(b) show that the ultrasound transmission was greatly improved by the beamforming. It can be observed that a larger region of the part was insonified. Not only the coverage was increased, an average gain of 12 dB per transmission was observed by using the proposed strategy, when compared to FMC.

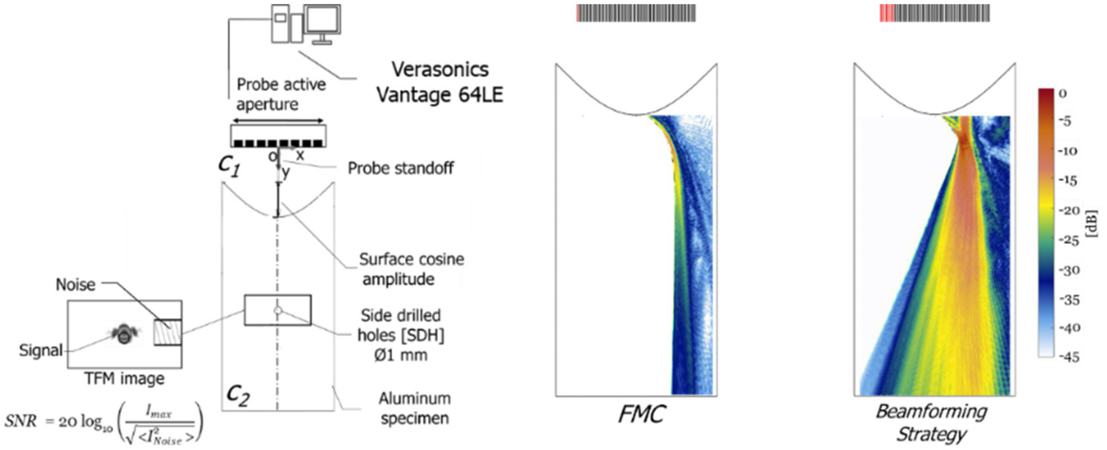
Verasonics
Vantage 64LE
Probe active
aperture
o
x
y
C_1
Probe standoff
Surface cosine
amplitude
Noise
Signal
TFM image
Side drilled
holes [SDH]
Ø1 mm
C_2
Aluminum
specimen
$SNR = 20\log_{10}\left(\frac{I_{max}}{\sqrt{<I^2_{Noise}>}}\right)$
FMC
Beamforming
Strategy
0
-5
-10
-15
-20
-25
-30
-35
-40
-45
[dB]

(a) (b)

Figure 3-2 (a) Experimental setup; (b) Comparison of beam characteristics for FMC and beamforming strategy

This improvement was translated into the TFM images. Figure 3-3 presents the images of a SDH 40 mm below the surface when using a probe standoff distance of 70 mm. The scale was kept at -50 dB so the artefacts are also visible. The first image, Figure 3-3(a), contains the rendering done using the FMC. Here, the reconstruction of the signals shows an indication of the SDH upper face reflections which agrees with the real defect position. Furthermore, there is a considerable number of artefacts in the image possibly due to poor transmission at this probe standoff. As a result, the SNR calculated was 30dB. Now, looking at the image generated using the proposed beamforming in Figure 3-3(b), it is clear that the level of artifacts is lower. In terms of SNR, 41.1 dB was calculated. Interestingly, as shown by Figure 3-3(c), even by reducing the beamforming transmission events to only 12, the image is still better than the FMC. Which means that with less than a quarter of the transmission events than the FMC, there is still a gain of 8 dB in the image SNR.

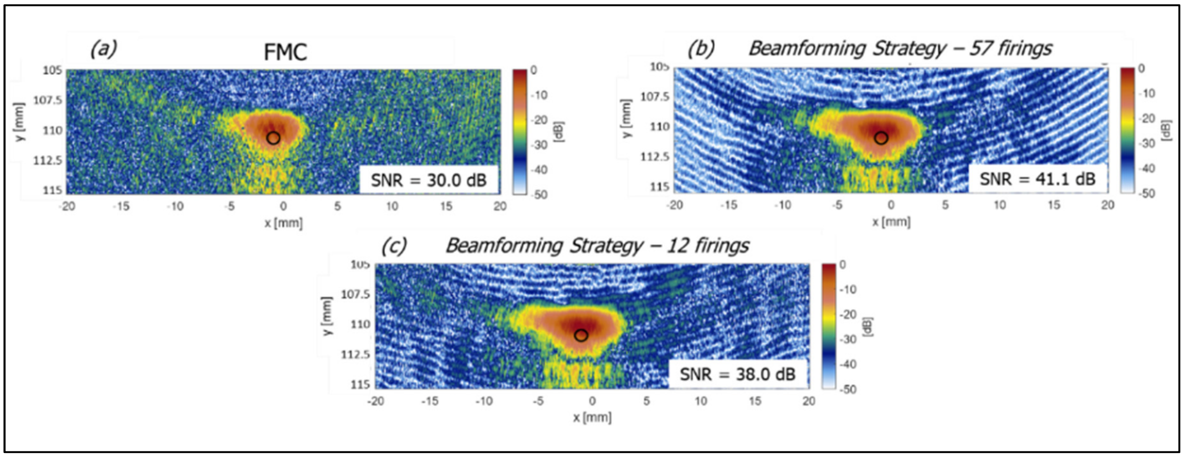

Figure 3-3 TFM images of SDH with 1 mm diameter below a concave surface. Images generated using different transmission strategies

3.5 Conclusion

In this work it was demonstrated that the ultrasound transmission must be adapted to the surface profile to yield a better TFM quality. An improvement of up to 11 dB in SNR was observed. It can also be noted that the proposed approach achieved a superior image quality with fewer transmissions, 57 or 12 versus the 64 required for the FMC. Future works will investigate the effect of other sub-apertures and surface shapes.

Acknowledgement: This study was supported by the oN-DuTy! NSERC CREATE program.

CHAPTER 4

GLOBAL TOTAL FOCUSING METHOD THROUGH DIGITAL TWIN AND ROBOTIC AUTOMATION FOR ULTRASONIC PHASED ARRAY INSPECTION OF COMPLEX COMPONENTS

J. F. Mansur Rodrigues Filho and P. Bélanger

Department of Mechanical Engineering, École de Technologie Supérieure,
1100 Notre-Dame West, Montreal, Quebec, Canada H3C 1K3

Paper submitted for publication, October 2022

4.1 Abstract

This paper tackles the challenging ultrasonic inspection of parts with complex geometries by proposing a novel global TFM (gTFM) approach. In this method, a digital twin is used to optimize and control the inspection, which consists of the probe being scanned around a complex part using a robotic arm, finally rendering a gTFM image by combining all acquisitions. To verify its validity, an aerospace disk forging mock-up, with side-drilled holes (SDH), was used. The mock-up geometry comprised multiple concave and convex surfaces. A comparison of different scan plans showed that adapting the probe position to the surface profile improved the imaging performance. Furthermore, by using a typical constant probe standoff, strong reconstruction artifacts were generated, inevitably rendering the inspection unreliable. On the other hand, by using an optimal scan plan, the gTFM image showed a sharp image of the SDHs. Compared to the other strategies, the optimal scan plan achieved a 40% increase in the mean contrast-to-noise ratio (CNR), a 70% reduction in the position error (only 0.1mm), and a reduction of 33% in the array performance indicator (API). Inspection coverage was achieved efficiently, depicting the complete cross-section of the specimen using only 7 probe positions.

Keywords: Phased array ultrasonic testing, Total Focusing Method (TFM), Robotic automation, Smart NDE

4.2 Introduction

Ultrasonic imaging in the non-destructive evaluation (NDE) of engineering components has advanced rapidly over the last two decades. In fact, ultrasonic phased arrays allow high inspection flexibility, achieved through the control of the beam using delay laws (Drinkwater & Wilcox, 2006). Moreover, full matrix capture (FMC) and data post-processing methods, such as the total focusing method (TFM), allow defect imaging with high resolution (Holmes et al., 2005). However, the ultrasonic NDE of components with complex geometries continues to be a challenge. The curved interfaces in these components cause beam distortions that lead to a loss of sensitivity and coverage, lowering the inspection capacity for defect detection and characterization (Mahaut et al., 2002).

Extensive research has been done to mitigate the problem described above. Studies have successfully shown that flexible probes (Chatillon et al., 2000; Hunter et al., 2010) and shape sensing fibers (Lane, 2014) that are capable of adapting to the surface curvature are helpful. In parallel, adaptable coupling media, such as a water-filled membranes (Russell et al., 2010), and even encasing the part in ice (Simonetti & Fox, 2019), have been shown to improve the ultrasonic inspection of complex specimens. Nevertheless, these solutions tend to be too complex or expensive, and whenever water immersion is possible, it tends to be the logical choice. In the latter, no custom wedges or special probes are needed, which eases the inspection, minimizes probe wear, and reduces costs.

As has been demonstrated in the literature, the processing of FMC data from arrays in immersion allows the efficient generation of TFM images even through unknown complex interfaces (Hunter et al., 2010; M. Sutcliffe et al., 2013; Zhang et al., 2014). As an alternative, authors have also proposed plane wave imaging (PWI) (Rachev et al., 2020) and virtual source aperture techniques (Hoyle et al., 2018) to post-process the FMC of nonplanar parts into sharp subsurface images. More recently, even volumetric imaging through doubly curved interfaces using a matrix probe has been demonstrated (McKee et al., 2020). These imaging processes are achieved by ultrasonically identifying the surface and then adapting the focusing delays to account for the refraction at the interface. Yet, even with demonstrated methods for proper surface identification (Kerr et al., 2016; Matuda et al., 2019) or perfect surface adaptation, the imaging performance still suffers if strong curvatures are present in the profile (Malkin et al., 2018). In cases where the radius of curvature is around half to one times the size of the active aperture of the probe, it has been shown that the probe standoff must be optimized to avoid reconstruction artifacts (Mansur Rodrigues Filho & Bélanger, 2021).

Especially in ultrasonic NDE, the use of robotic arms has seen a recent spike in research (Chabot, Laroche, Carcreff, Rauch, & Hascoët, 2020; Mei, Jin, Yu, Wu, & Yang, 2021; Y. J. Mei et al., 2021; Zimermann et al., 2021). This can be explained by the fact that modern robotic arms offer high repeatability as well as the possibility of using complex scan plans. The application of robotic automation and deep learning in classical ultrasonic testing has been shown to improve images of defects below complex curvatures (Y. Mei et al., 2021). In another approach, researchers have shown that using a single-element probe in a robotically controlled path allows the combination of different incident angles in the imaging of defects inside specimens with curved profiles (Y. J. Mei et al., 2021).

Therefore, this work proposes a novel approach to the inspection of complex specimens. By combining robotic automation with ultrasonic phased array TFM imaging, the method uses a digital twin of the inspection setup to optimize the scan plan, and by using all probe positions in the image rendering, a global TFM (gTFM) strategy is proposed. The method was verified with a mock-up of an aerospace forging with a complex profile. This case study was selected because aircraft fan disk parts must meet extremely high manufacturing standards and are made of expensive and hard alloys. In this cost intensive process, the parts are machined into a sonic shape just to run the ultrasonic inspection, and only after approval machined into the final shape (Howard et al., 2007). The aim is thus to show that this machining step can be avoided by enabling the inspection of the complex-shaped as-forged state.

4.3 Materials and methods

4.3.1 Global Total Focusing Method (gTFM)

The gTFM expands the capabilities of the TFM (Holmes et al., 2005) by using several probe positions around the specimen and adaptations to its surface profile. This is only possible because the gTFM combines phased array ultrasonic testing in immersion with robotic automation. This allows the application of intricate and precise scan plans.

The method can be explained through the schematics depicted in Figure 4-1. Considering an arbitrary specimen with a complex profile, as shown in Figure 4-1(a), the first step for imaging an internal flaw is to section the surface profile between concave and convex surfaces *[c]*. As such, the phased array ultrasonic probe is scanned around the part based on a global reference system *(X,Y)*, as shown in Figure 4-1(b). For each probe position, which is based on the surface profile curved section *[c]* and the standoff *[s]*, a FMC is acquired. For an array with *N* elements, with a combination of emitting *[e]* and receiving *[r]* elements, *NxN* A-scans are stored from the first to the N^{th} element as A_{ercs} ($A_{1111}(t)$, $A_{1211}(t)$, ..., $A_{1N11}(t)$, ..., $A_{2111}(t)$, ..., $A_{NN11}(t)$, ..., $A_{NNcs}(t)$).

As shown in Figure 4-1(c), the probe is positioned based on the profile sections *[c]*. Using the center point of each curved section (m_c), the probe is moved from the origin (X_o,Y_o) of the global reference system to the position given by (x',y'). At this position, the probe is centered, ensuring a parallel and symmetric distribution of the array elements relative to the surface section being scanned. This alignment is done through a rigid rotation R(θ_c) of the probe center, where the angle θ_c is found using the normal and tangent vectors ($\overrightarrow{n_c}$ and $\overrightarrow{t_c}$) at the center point (m_c). Lastly, the probe standoff *[s]* is defined as the distance from the center of the probe to m_c, and a rigid translation t(X_s,Y_s) is used to vary the standoffs:

$$\begin{pmatrix} x'_{c,s} \\ y'_{c,s} \end{pmatrix} = \mathrm{R}(\theta_c) \begin{pmatrix} X_o \\ Y_o \end{pmatrix} + \begin{pmatrix} X_s \\ Y_s \end{pmatrix} \tag{4.1}$$

As shown in Figure 4-1(b), the calculation of the TFM is done using the coordinates of the active (x_{ecs},y_{ecs}) and receiving (x_{rcs},y_{rcs}) elements, the speed of sound of the coupling medium (v_1), the speed of sound of the specimen material (v_2) and the coordinates of the surface profile (X_{jc},Y_{jc}). First, the time-of-flight is calculated using wave paths as $(d_1,\dots,d_4)$ shown in Figure 4-1(b), for each combination of active *[e]*, receiving element *[r]*, surface profile point (X_{jc}, Y_{jc}) and pixel on the grid (X_p, Y_p):

$$t_{ecs} = \frac{d_1}{v_1} + \frac{d_2}{v_2}\ ;\ t_{rcs} = \frac{d_4}{v_1} + \frac{d_3}{v_2}, \tag{4.2}$$

$$t_{ecs} = \frac{\sqrt{\left(X_{jc} - x_{ecs}\right)^2 + \left(Y_{jc} - y_{ecs}\right)^2}}{v_1} + \frac{\sqrt{\left(X_p - X_{jc}\right)^2 + \left(Y_p - Y_{jc}\right)^2}}{v_2} \tag{4.3}$$

$$t_{rcs} = \frac{\sqrt{\left(X_{jc} - x_{rcs}\right)^2 + (Y_{ic} - y_{rcs})^2}}{v_1} + \frac{\sqrt{\left(X_p - X_{jc}\right)^2 + \left(Y_p - Y_{jc}\right)^2}}{v_2} \tag{4.4}$$

Moreover, the correct times-of-flight (t_{ecs}) and (t_{rcs}) are chosen based on a grid search of the *[j]* surface profile points of the curvature *[c]* to find the point (X_{jc},Y_{jc}) that respects Fermat's principle through the stationary time-of-flight condition:

$$\frac{dt_{ecs}}{dX_{jc}} = 0\ ;\ \frac{dt_{rcs}}{dX_{jc}} = 0 \tag{4.5}$$

Then, this procedure is repeated for all pixels *[p]* in the grid. By using the A-scans and a fixed grid of *[p]* pixels, as shown in Figure 4-1(b), through the summation of all emission and reception combinations, a Hilbert transform H is applied to generate the TFM image I_{cs}:

$$I_{cs}(X,Y) = \left| H\left(\sum_{e=1}^{N} \sum_{r=1}^{N} A_{ercs}\,(t_{ecs} + t_{rcs}) \right) \right| \tag{4.6}$$

Finally, since the grid of pixels is the same for all TFM images, a composition can be made using the images generated at different probe positions through a simple summation:

$$G(X,Y) = \left| \left(\sum_{c=1}^{C} \sum_{s=1}^{S} I_{cs} \right) \right| \tag{4.7}$$

rendering the gTFM image *G,* which covers the whole specimen. This is especially important for the case of complex profiles.

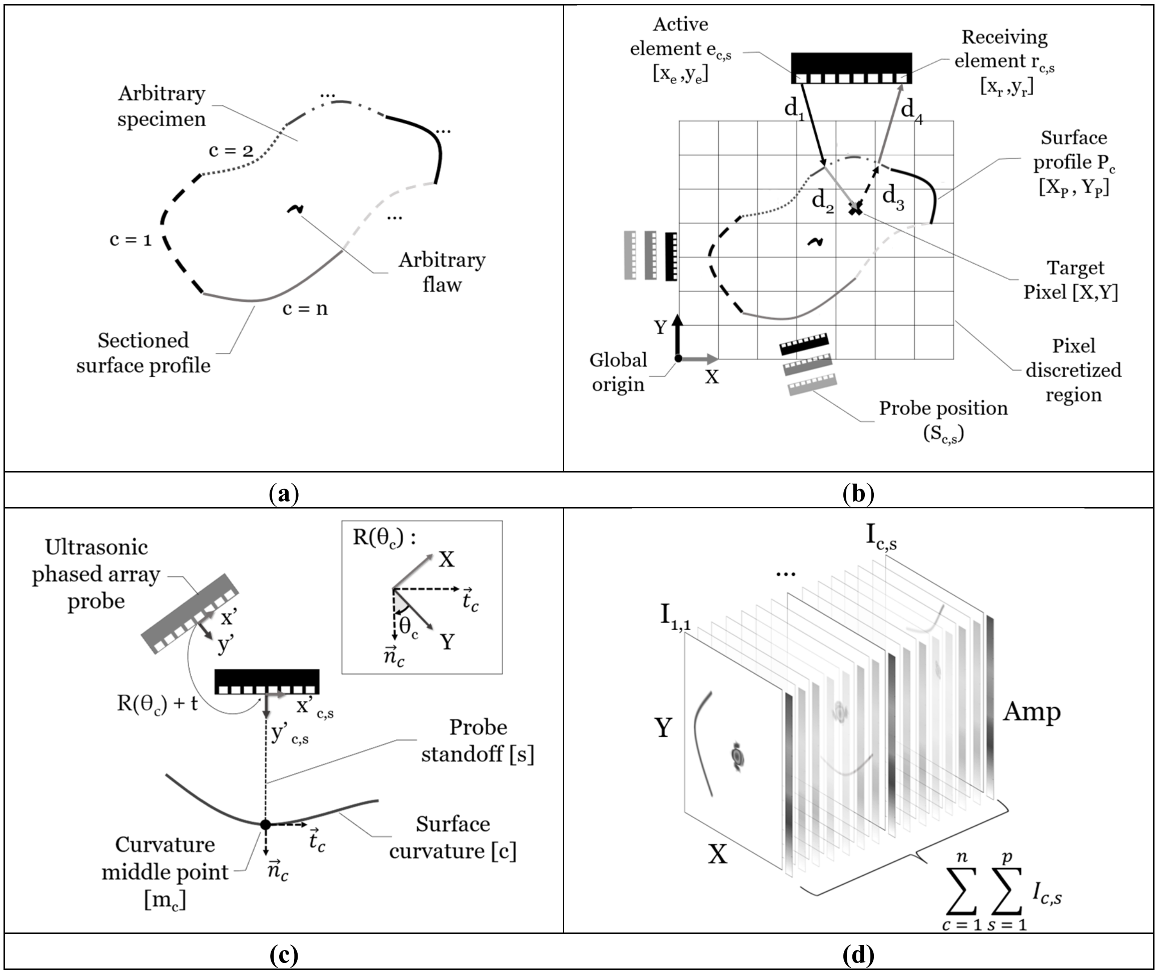
Arbitrary specimen
c = 2
c = 1
c = n
Arbitrary flaw
Sectioned surface profile
Active element $e_{c,s}$ $[x_e, y_e]$
Receiving element $r_{c,s}$ $[x_r, y_r]$
d_1
d_2
d_3
d_4
Surface profile P_c $[X_P, Y_P]$
Target Pixel [X,Y]
Y
X
Global origin
Pixel discretized region
Probe position ($S_{c,s}$)
Ultrasonic phased array probe
x'
y'
$R(\theta_c)$:
X
Y
$\vec{t}_c$
$\vec{n}_c$
θ_c
$R(\theta_c) + t$
$x'_{c,s}$
$y'_{c,s}$
Probe standoff [s]
Surface curvature [c]
Curvature middle point $[m_c]$
$I_{c,s}$
$I_{1,1}$
Y
X
Amp
$\sum_{c=1}^{n}\sum_{s=1}^{p} I_{c,s}$

(a)

(b)

(c)

(d)

Figure 4-1 Schematic of gTFM workflow **(a)** Curvature sectioning of the arbitrary specimen; **(b)** Fixed grid of pixels definition, TFM calculation, and probe positioning; **(c)** Probe positioning relative to curvatures and standoffs; **(d)** gTFM image summation process

4.3.2 Complex specimen gTFM optimization

The gTFM can be optimized according to the surface profile of the specimen, especially when the radii of curvature are in the range of half to one times the active aperture of the probe. A range of probe standoffs *[s]* may be tested for the inspection of these curved specimens, but it is possible to predict the best imaging performance using a probe standoff optimization method (PSOM) (Mansur Rodrigues Filho & Bélanger, 2021). As shown in Figure 4-2(a), the PSOM uses the array response to a point reflector, or the point spread function (PSF), to search for the best imaging performance over a range of probe standoffs. Hence, it is possible to design an optimized scan plan for each specimen through a simulation based on the digital representation of the part.

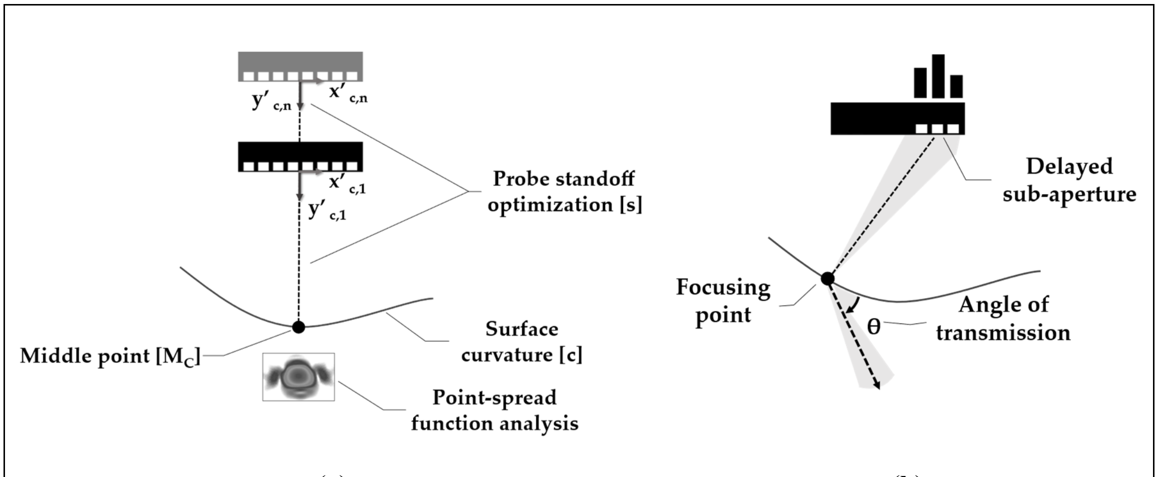
$y'_{c,n}$
$x'_{c,n}$
$x'_{c,1}$
$y'_{c,1}$
Probe standoff optimization [s]
Surface curvature [c]
Middle point [M_C]
Point-spread function analysis
Delayed sub-aperture
Focusing point
Angle of transmission
θ

(**a**) (**b**)

Figure 4-2 **(a)** Schematic of the probe standoff optimization method (PSOM); **(b)** Schematic of the beamforming strategy to compensate for concave curvature effects on the beam transmission

In this method, a simplified PSF calculation is conducted based on TFM imaging using a single wave mode. Therefore, based on the probe parameters, surface profile, and materials, the TFM delays are calculated and used to shift a toneburst. This toneburst is then modulated by the geometric attenuation, the element directivity, and the transmission coefficient to estimate the pulse response of a point target inside the part. Finally, the optimal probe standoff is selected based on the smallest main lobe width and lowest side lobe level criteria.

A beamforming strategy to compensate for concave surfaces was also applied to verify its influence on the gTFM imaging (Mansur Rodrigues Filho & Bélanger, 2022). Flaws under concave surfaces are difficult to inspect, since wave path and beam shape variations may lead to poor imaging and reconstruction artifacts. A virtual array composed of focusing sub-apertures was demonstrated to be capable of generating improved TFM imaging in these cases. This procedure can be done online or in the post-processing of the FMC matrix. As shown in Figure 4-2(b), the use of sub-apertures ensures that the desired ultrasound beam is generated inside the specimen, with its main direction insonifying the region of interest. By delaying the elements in the sub-aperture, a focal point is generated at the surface for each transmission event. All elements receive the signals for each event. The focal point in the surface is selected using Snell's law, based on the desired refraction angle in transmission. Then, the delay laws are calculated and applied to the FMC matrix. In this work, 7 elements were used to compose the sub-apertures, which led to 58 transmission events on the FMC. Additionally, the beams at each transmission were pointed at 50 mm below the center of the concave curvatures, chosen through a grid search method. Finally, the TFM was applied to the modified A-scans.

4.3.3 Case study: the specimen design

A proof of concept was conducted using two different test specimens. Initially, the simple case of an aluminum block with flat surfaces was analyzed. The specimen contained five side-drilled holes (SDH) of 1 mm in diameter. All the dimensions of this block are depicted in Figure 4-3(a). In this case, the goal was to verify whether the images obtained in multiple directions could be matched correctly into a single rendering. Moreover, the flat surfaces allowed to easily calibrate the robot's position relative to the part.

Next, a complex case was tested. The testing specimen was designed to represent a section of an arbitrary forging of an aerospace turbine disk part. It was decided to make it of stainless steel 430 to approximate the acoustic impedance of the typical materials used in the aerospace industry. The specimen's profile consisted of a combination of concave and convex curvatures. A total of 30 artificial internal defects were introduced at semi-random positions, made up of SDH of 1.5 mm in diameter. All the dimensions of this specimen are detailed in Figure 4-3(b) and the positions of the SDH are specified in Table 4-1.

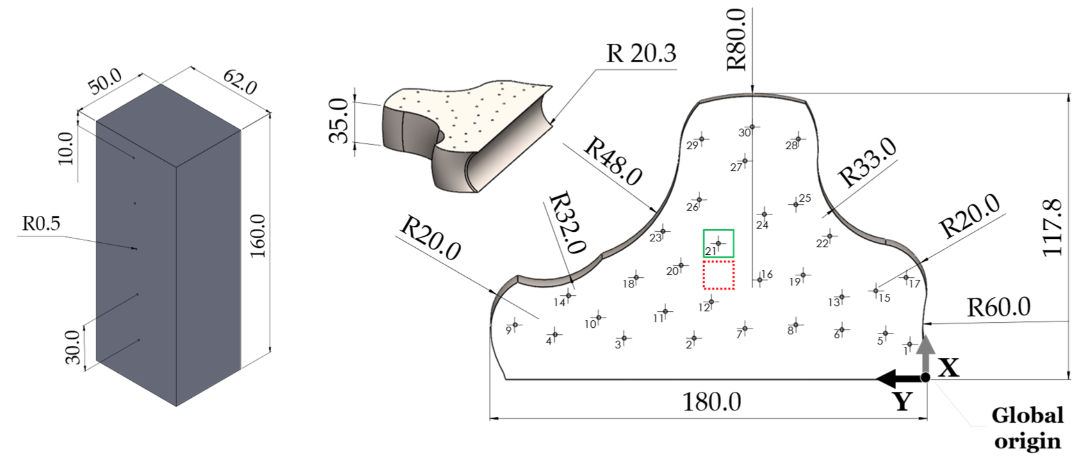
50.0
62.0
10.0
R0.5
160.0
30.0
35.0
R 20.3
R80.0
R48.0
R32.0
R20.0
R33.0
R20.0
117.8
R60.0
180.0
X
Y
Global origin
1
2
3
4
5
6
7
8
9
10
11
12
13
14
15
16
17
18
19
20
21
22
23
24
25
26
27
28
29
30

(a) **(b)**

Figure 4-3 **(a)** Drawing of flat aluminum specimen; **(b)** Drawing of stainless-steel complex part representing an aerospace forging mock-up

Table 4-1 SDH index and coordinates on stainless steel forging section

SDH index	X [mm]	Y [mm]	SDH index	X [mm]	Y [mm]	SDH index	X [mm]	Y [mm]
1	-34.5	18.12	11	-48	119	21	-76	97.12
2	-37	107.12	12	-52	100	22	-79	51.12
3	-37	136	13	-54	46.12	23	-81	120
4	-38.5	164.5	14	-54.5	159	24	-88	78.12
5	-39	28.12	15	-56.5	32.12	25	-92	65.12
6	-40.5	46.12	16	-61	80	26	-94	105
7	-41	86.12	17	-62	19.62	27	-110	86.12
8	-42.5	65.12	18	-62	131	28	-119	64.12
9	-42.5	181	19	-63	62.12	29	-119	104
10	-45.5	146.5	20	-67	112.5	30	-124	83.12

4.3.4 Experimental setup

As shown in Figure 4-4, the hardware of the experimental setup consisted of a water tank, where the tested specimens were placed in immersion. A 3D-printed plastic base was used to ease the positioning calibration between the robotic arm reference system and the specimen. The robotic arm used was a Staubli TX-90 with an ultrasonic phased array probe attached through a personalized plastic holder, as illustrated in Figure 4-4. For its part, the probe used was an Olympus 5L64I, which has 64 elements with a 0.6 mm pitch and a 5MHz central frequency. Both the robotic arm and the probe were connected to a Verasonics Vantage 64LE system.

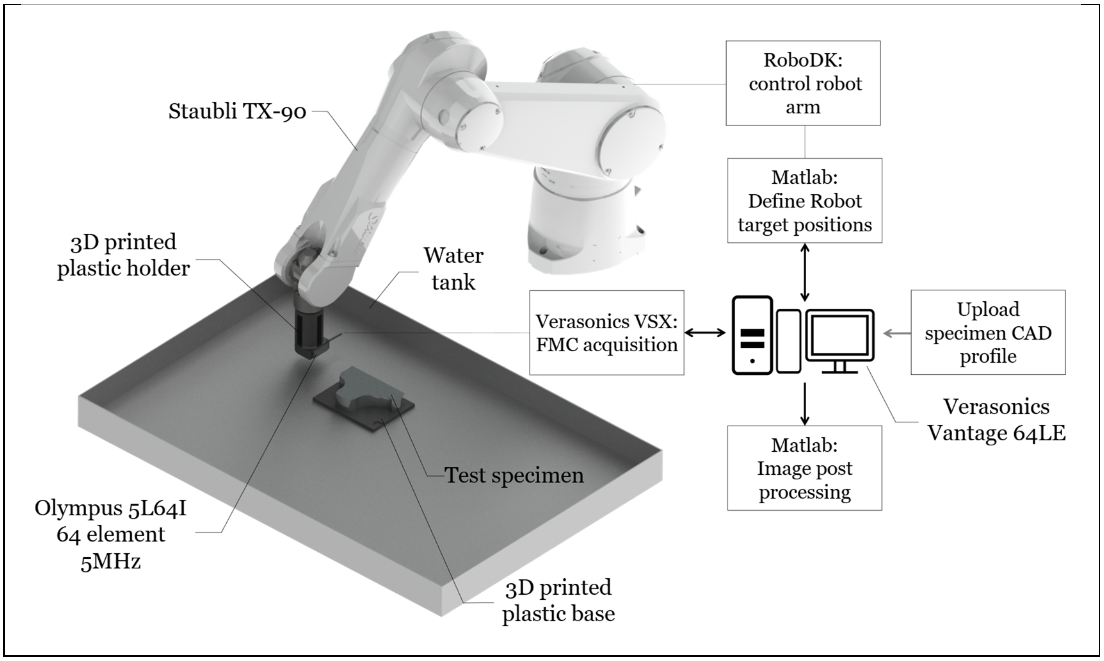
RoboDK: control robot arm
Staubli TX-90
Matlab: Define Robot target positions
3D printed plastic holder
Water tank
Verasonics VSX: FMC acquisition
Upload specimen CAD profile
Verasonics Vantage 64LE
Matlab: Image post processing
Test specimen
Olympus 5L64I 64 element 5MHz
3D printed plastic base

Figure 4-4 Schematic of the experimental setup for application of the gTFM on the specimens

As shown in the block diagram of Figure 4-4, the first step in the software side consists in using a Matlab® routine and API to upload the CAD profile of the specimens into RoboDK®. This digital twin is then used to define the steps of the real inspection by creating the targets for probe placement. As shown in Figure 4-5, these targets are generated through the discretization of the surface profile. As explained in section 4.3.1, the probe was centered relative to each concave or convex curved section and the standoff varied through a range of values, as detailed in Table 4-2. To this end, the probe reference system was placed in the center of the face of the array and the targets were generated through rotations and translations. A simulation of the robot movement was done using the digital twin of the inspection to avoid any collisions.

Table 4-2 Probe position indexes used in the experiments – number of standoffs and range

Curvature [c]	**Standoffs [s]**	**Standoff range [mm]**
Flat specimen		
[F1, F6]	1	55
Complex specimen		
1	21	[20,120]
2	8	[25,60]
3	21	[20,120]
4	-	-
5	8	[25,60]
6	-	-
7	21	[20,120]
8	17	[40,120]
9	8	[25,60]

With the targets designated, another Matlab® routine was used to conduct the experiments. In this routine, for each target in the scan plan, the robotic arm was moved, the probe placed at the designated position, and the FMC was acquired. Thirty averages were used at each FMC acquisition. After the acquisition was complete, the TFM image of each probe position was post-processed, as explained in section 4.3.1, using a Matlab® algorithm on the Vantage computer. A pixel resolution of 0.25x0.25 mm was used to render the images. Finally, with all the individual TFM images, the gTFM could be rendered.

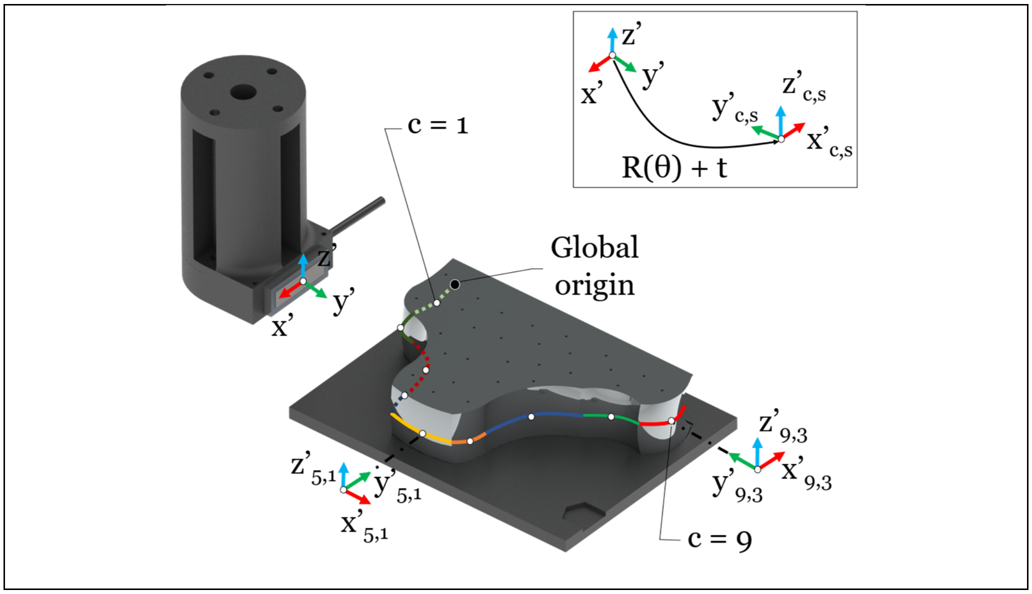

Figure 4-5 Schematic of CAD profile upload, discretization, and probe placement. The probe reference system, in the face of the probe, is moved around to the designated targets

4.3.5 Complex specimen scan plan comparison

Five different scan plans were used to verify the gTFM performance with and without optimizations. The goal was to account for the benefits of designing a scan plan with the probe position adapted to the surface profile. Table 4-3 Scan plans analyzed - Probe position and characteristics summarizes the five strategies, the probe positions used, and the main characteristics of each scan plan.

Strategy 1 was chosen to represent a poor scan plan, using only probe positions with the lowest results in the PSOM, while strategy 2 was chosen to represent a simple scan plan, with the probe standoff kept constant around all the seven concave and convex curved surfaces analyzed. In the latter, there is no prior inspection simulation for its design, which might be the approach taken in an industrial setup. Moreover, strategy 3 considers a “brute force” approach, by using the full range of standoffs tested in this experiment, with a total of 104 probe positions.

Finally, strategies 4 and 5 are the optimized scan plans. In strategy 4, for each of the seven curved surface's sections, the standoff with the best PSF performance was chosen using the PSOM. In strategy 5, the beamforming compensation for concave curvatures explained in section 4.3.2 was added to the FMC of curvatures 3, 7, and 8 of the PSOM scan plan.

Table 4-3 Scan plans analyzed - Probe position and characteristics

gTFM scan plan strategy	Probe positions $S_{c,s}$	Characteristics
1	$S_{1,21}$; $S_{2,8}$; $S_{3,7}$; $S_{5,8}$; $S_{7,12}$; $S_{8,3}$; $S_{9,8}$	Poor PSOM performance
2	$S_{1,8}$; $S_{2,7}$; $S_{3,8}$; $S_{5,7}$; $S_{7,8}$; $S_{8,4}$; $S_{9,7}$	Constant standoffs
3	$S_{1,1}$; …; $S_{1,21}$; …; $S_{9,1}$; …; $S_{9,8}$	Full range summation
4	$S_{1,10}$; $S_{2,5}$; $S_{3,13}$; $S_{5,5}$; $S_{7,21}$; $S_{8,9}$; $S_{9,5}$	Best PSOM
5	$S_{1,10}$; $S_{2,5}$; $S_{3,13}$*; $S_{5,5}$; $S_{7,21}$*; $S_{8,9}$*; $S_{9,5}$	Best PSOM + Beamforming*
(*) Probe positions at which a sub-aperture beamforming was applied		

4.3.6 Analysis of gTFM imaging performance

Since the gTFM was tested in combination with different inspection strategies, quantitative metrics were selected to verify its overall performance. Specifically, the following were chosen to measure the imaging quality: the contrast-to-noise ratio (CNR), the array performance indicator (API), and the defects position. As shown in Figure 4-3, to analyze the CNR, a window centered with the defect (in solid green) and a window in a flawless region (in dashed red) were used for each SDH in the part. Both windows were 5x5 mm in size and placed 1.25 mm apart in the direction that ensured that the dashed red window was positioned in a flawless region. The CNR was calculated for each SDH using the following equation (Patterson & Foster, 1983):

$$CNR = \frac{\mu_{signal} - \mu_{noise}}{\sqrt{\sigma_{signal}{}^2 + \sigma_{noise}{}^2}} \tag{4.8}$$

where μ_{signal} is the mean of the pixel intensities in the window containing the SDH. Likewise, μ_{noise} is the mean of the pixel intensities inside the window placed in the flawless region. Lastly, σ_{signal}^2 and σ_{noise}^2 are the variances of the intensities in these windows.

The API was calculated using (Malkin et al., 2018):

$$API = \frac{A_{\text{-}6dB}}{\lambda^2} \tag{4.9}$$

where $A_{\text{-}6dB}$ is the area occupied by the pixels with intensities ranging from the maximum to 6 dB below the maximum and λ^2 is the square of the wavelength in the test material. Again, the API was calculated for each SDH using the window already described. Finally, the position accuracy was calculated through the difference between the expected SDH position and the position of the pixel with maximum intensity in the window around the defect.

4.4 Results and discussion

4.4.1 gTFM renderings

In all the gTFM figures, the probe positions used to inspect the parts are presented as a schematic. This schematic and Table 4-2 and Table 4-3 indicate the standoffs and probe position coordinates in the global system. Moreover, the black solid line in the gTFMs represents the expected position of the part's surface. For each probe position in the scan plan, one TFM image was generated to render the gTFM.

4.4.2 Flat specimen gTFM rendering

The first result comes from the flat aluminum specimen and is presented in Figure 4-6. Even though the gTFM framework is intended for specimens with complex profiles, this gTFM delivered an interesting proof of concept. Through the composition of six individual TFMs, the resulting image shows the indications of the part's surfaces and five SDH with excellent contrast. The speckles are 40 dB below these indications.

This is because the indications that are common throughout all images get reinforced in summation, whereas the speckle noise is random and gets suppressed in the process. Furthermore, having the probe insonifying from different directions reduces the effect of attenuation. The amplitude of all the flaws' indications is similar, which eases the image interpretation, even without procedures such as distance amplitude calibration (DAC).

A good correlation between the physical setup and the digital twin was achieved for the robot-specimen positioning. It must be noted that this is a fundamental aspect of the gTFM reconstruction since it requires precise knowledge of the probe coordinates.

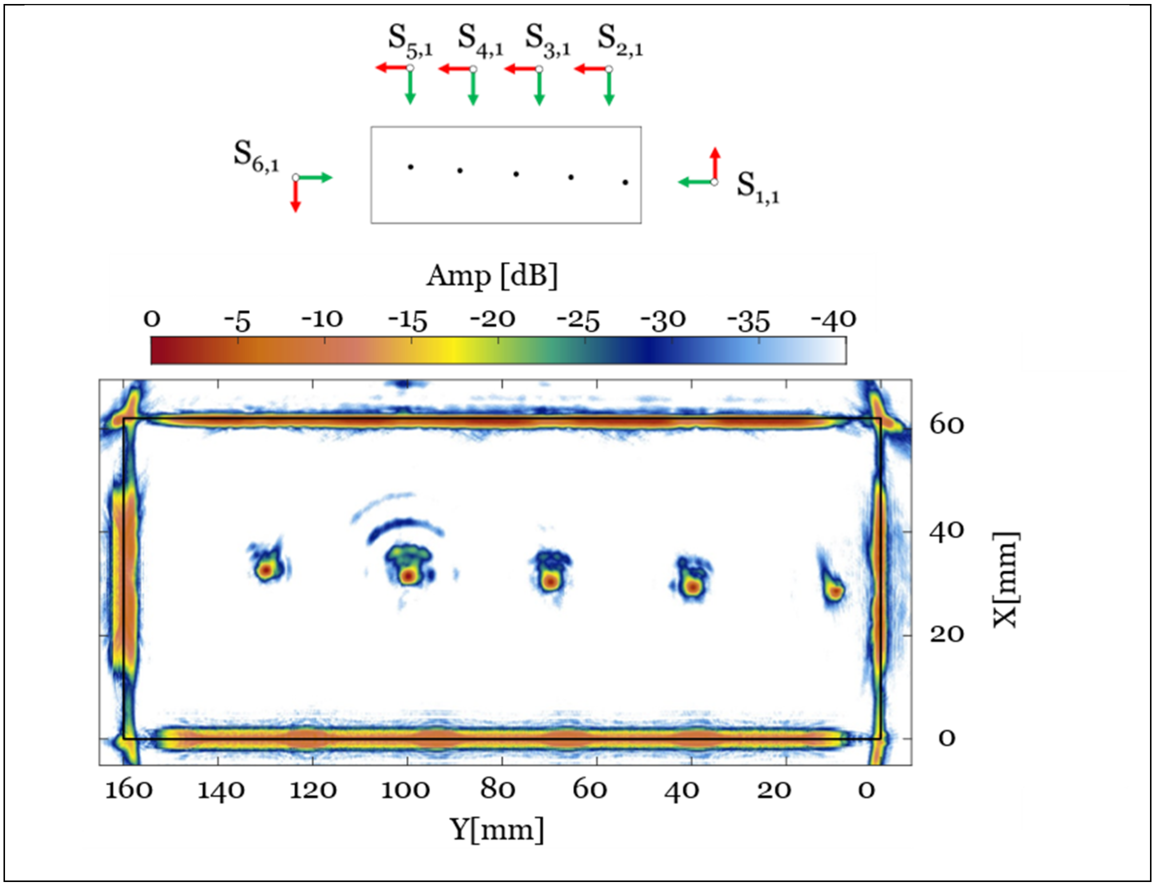

Figure 4-6 gTFM of flat aluminum specimen and schematic of the probe positions used to generate each image in the global summation

4.4.3 Complex specimen gTFM rendering – strategy 1

In the second result, the gTFM of the stainless-steel complex part inspected using strategy 1 is presented in Figure 4-7. The resulting image has a poor quality, with several reconstruction artifacts. Also, because of the surface profile and stronger attenuation, the dynamic range is reduced to 20 dB in this specimen. Even though some of the indications were derived from defects, they would be difficult to identify in a real inspection scenario. In fact, this shows that the non-optimized probe positions had a detrimental effect on the global summation.

These artifacts were mainly caused by the concave curvatures in the profile. They occurred because of the interaction of the ultrasonic beam and the interface of the specimen. When beamforming the FMC signal, the TFM algorithm forces a focus on every point in a region of interest. As well, the image quality depends on the physical capacity of the array to generate a sharp focus. However, in an immersion setup, a curved interface acts as a lens, changing the focus shape. Thus, even though the algorithm is synthetically generating a focus on a given point, physically, the probe properties may not allow the generation of a sharp focus, or in extreme cases, will allow no focus at all. In this case, the waves were refracted in directions of low sensitivity, which led to a point spread function with a high side lobe level.

4.4.4 Complex specimen gTFM rendering – strategy 2

Another gTFM of the stainless-steel complex part is presented in Figure 4-8. This image was generated using the scan plan of strategy 2. In this case, scanning with a constant probe standoff resulted in artifacts with a slightly lower amplitude and smaller size. Still, their presence compromised the image clarity, resulting in a very poor defect identification. This result is similar to what was obtained using strategy 1, even though strategy 1 deliberately had only poor probe standoffs. This shows that scanning a part with such a variable profile using a constant probe standoff is unreliable. There is a strong influence of the profile on the gTFM image quality. And since the studied profile had curves with different radii all around, keeping the same standoff resulted in some poor TFM images that disrupted the entire summation.

4.4.5 Complex specimen gTFM rendering – strategy 3

In the next gTFM image in Figure 4-9, strategy 3 was applied. By using the full range of standoffs, the artifacts are mitigated, and the amplitudes of the flaw indications are higher. It is possible to verify indications for all the SDH, with only the number 18 being dubious. In this case, the SDH indications were sharper because they were redundant throughout the range of standoffs and were reinforced by the summation process. Meanwhile, the artifacts were variable, and their amplitude was weakened by the summation process. Therefore, the amplitudes of the flaw indications became higher than the artifacts.

Nevertheless, the artifacts were still present in the summation and might interfere with the flaw identification in some regions, as can be seen in SDH number 18, which is not clear in the image due to the presence of an artifact in the background. A solution to this is presented by using the PSOM to avoid poor probe positions.

4.4.6 Complex specimen gTFM rendering – strategy 4

The following image in Figure 4-10 is the gTFM using strategy 4, the first optimized scan plan. By using the best TFM image in each probe position, the artifacts caused by the curvatures were suppressed and the indications of the SDHs were clearly visible. Removing the artifacts allowed SDH number 18 to be clearer than in the previous case.

However, due to the smaller number of redundant SDH indication images, some reconstruction artifacts coming from the flaws also became visible. These artifacts are caused by other wave modes and the geometric spread of the wave, which distorts the image far from the aperture. Still, these artifacts are not as problematic and can be suppressed using the beamforming enhancement described in section 4.3.2.

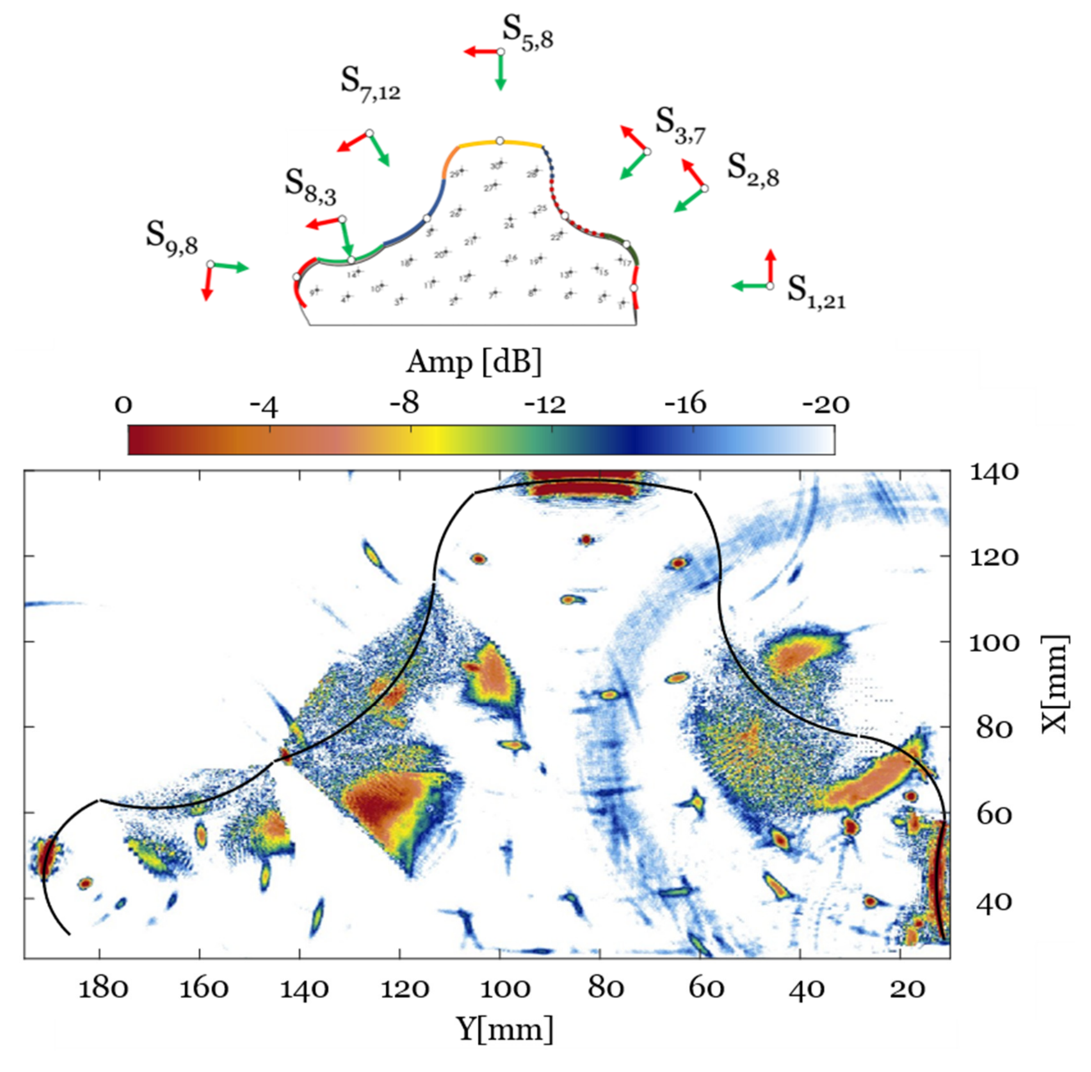

(Strategy 1 – poor scan plan)

Figure 4-7 gTFM of complex stainless-steel specimen when using a poor scan plan; schematic of the probe positions used to generate each image in the global summation

4.4.7 Complex specimen gTFM rendering – strategy 5

Lastly, the gTFM applied with all optimizations of strategy 5 is presented in Figure 4-11. In this image, even the artifacts caused by the flaws were suppressed. Also, the SDH indications, including number 18, were sharper when compared with strategy 4. This was achieved through the beamforming strategy, which improved the transmission through the concave surfaces. Directions of poor sensitivity were compensated by the delayed focusing sub-apertures.

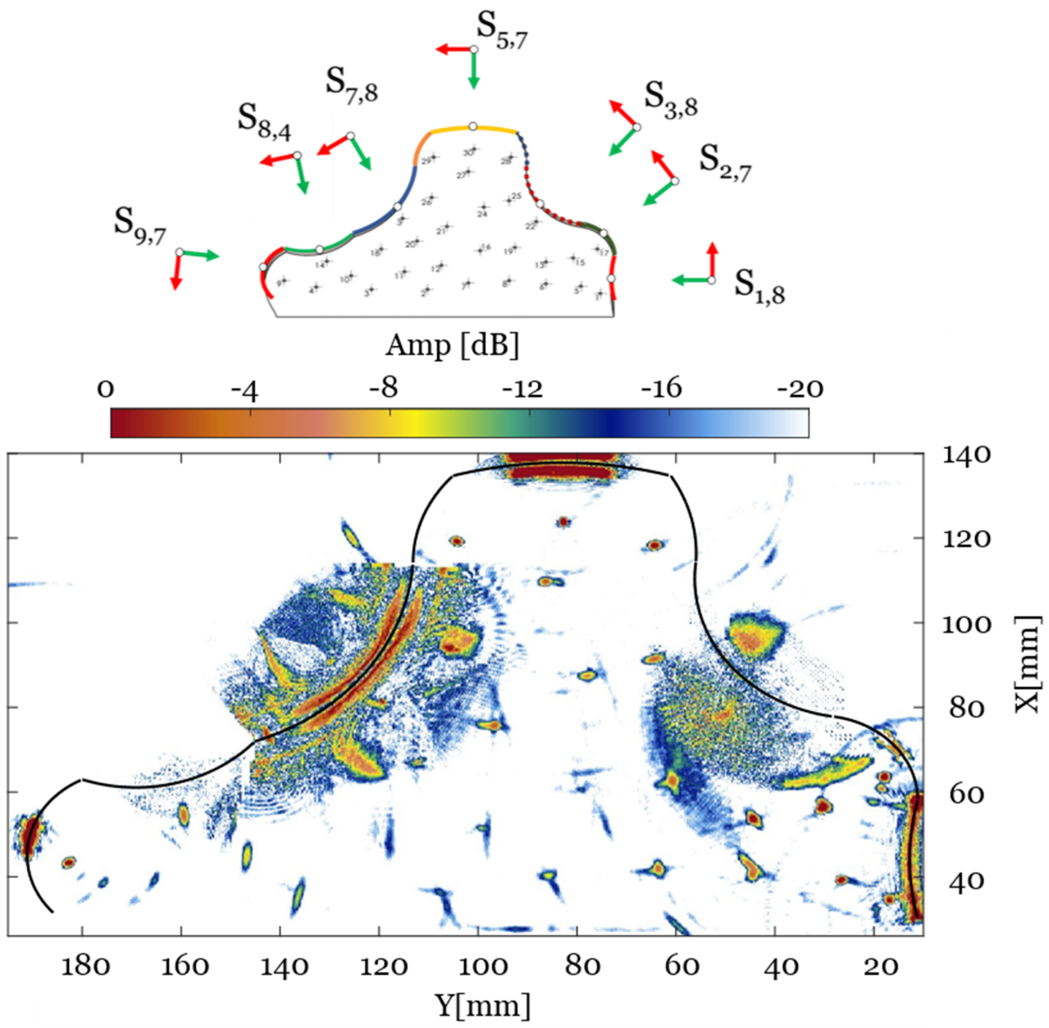

(Strategy 2 – constant path scan plan)

Figure 4-8 gTFM of complex stainless-steel specimen when using a constant standoff scan plan; schematic of the probe positions used to generate each image in the global summation

In practice, the beamforming process sharpened flaw indications by reinforcing the amplitude in directions in which the transmitted beam had higher sensitivity. Of note, avoiding the directions making little or no contribution to the focus sharpness also suppressed the artifacts. As a result, this latter gTFM qualitatively presents a clearer representation of the internal features of the complex specimen.

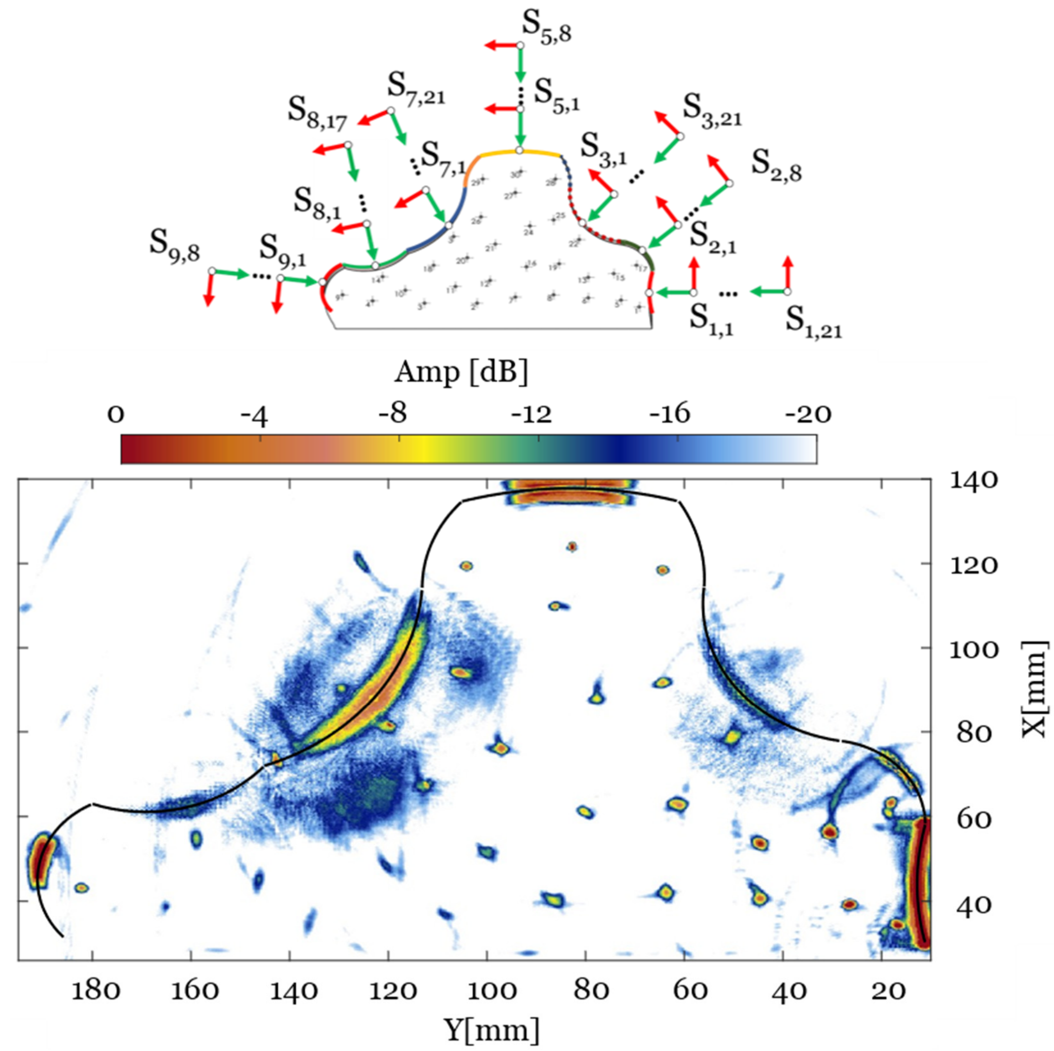

(Strategy 3 – full range scan plan)

Figure 4-9 gTFM of complex stainless-steel specimen when using a scan plan with a range of standoffs; schematic of the probe positions used to generate each image in the global summation

4.4.8 Complex specimen gTFM imaging quality

The imaging performance of the complex specimen using different scan plans is presented in Figure 4-12 through the CNR, API and position error metrics. It is important to note that where indications were covered by artifacts, the CNR was assumed to be zero and the API maximum.

In Figure 4-12(a), by accounting for all SDH in the complex profile, the mean CNR is presented for each strategy. This result confirms the visual conclusions seen in Figure 4-7 to Figure 4-11. An improvement of around 40% was observed in the CNR when strategies 3 to 5 were used. The mean CNR increased from 0.45 and 0.55 in strategies 1 and 2, to around 0.7 when strategies 3 to 5 were used.

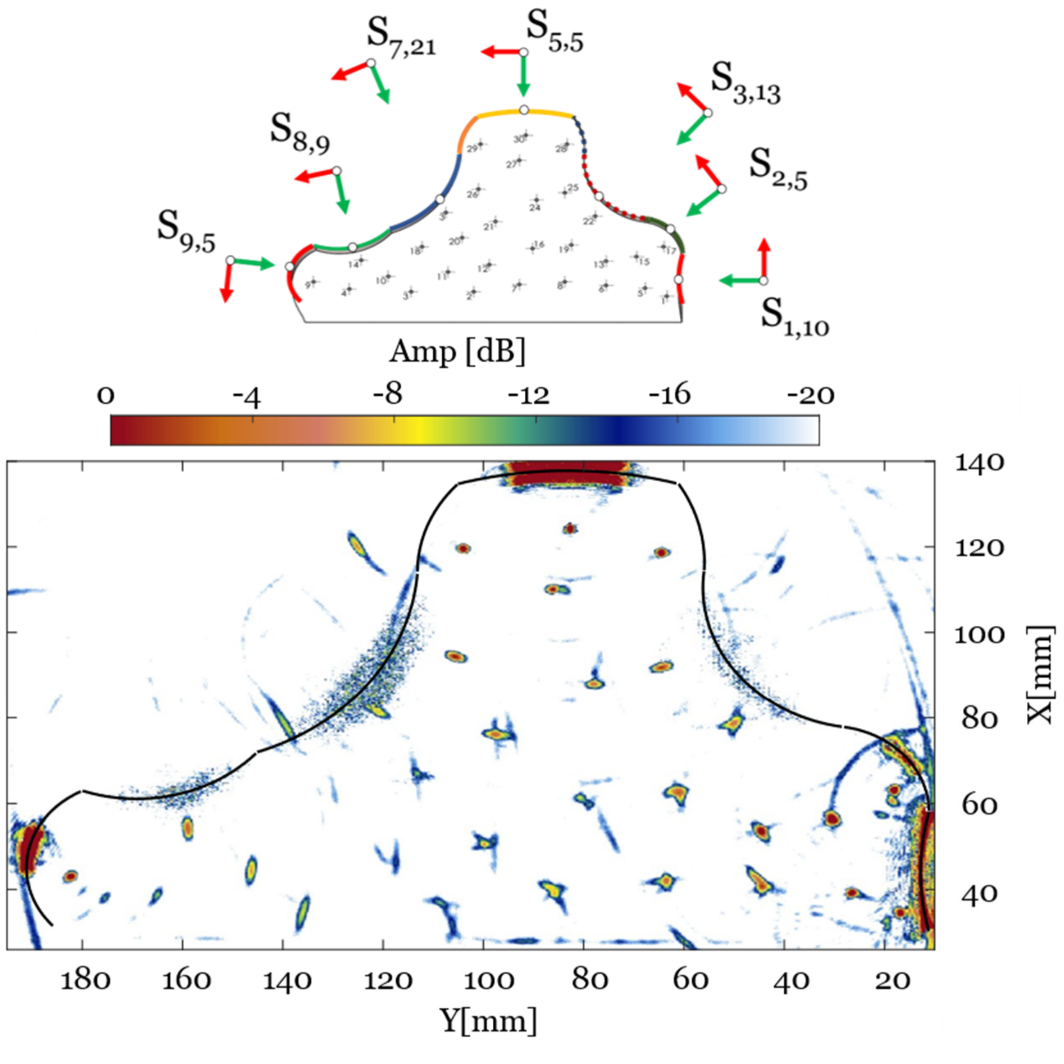

(Strategy 4 – PSOM scan plan)

Figure 4-10 gTFM of complex stainless-steel specimen when using a scan plan with optimized standoffs (PSOM); schematic of the probe positions used to generate each image in the global summation

Even though the CNR indicates that using strategy 3 might be a simpler and viable option than the optimized strategies, the following results show the gains brought about by the optimizations. In Figure 4-12(b), the mean API values demonstrate that the gTFM using strategy 5, shown in Figure 4-11, was indeed the sharpest. For strategy 3, the API was around 4.5, while for strategy 5, it was reduced to the minimum value of 3. The great performance of strategy 5 was also pointed out by the position error in Figure 4-12(c). Here, strategy 5 outperformed the other four strategies tested, with an average position error of only 0.1 mm, 70% smaller than the scan plan using strategy 3.

Another highlight of strategy 5 was the better coverage of SDH number 18. The graph in Figure 4-12(d) shows that strategy 3 presented a negative CNR of 0.2, an expected result given the presence of covering artifacts. Accordingly, the API was the worst for strategy 3. Meanwhile, using strategy 4, the PSOM ensured the maximum CNR and an API reduction of 50%. With an intermediary API, strategy 4 made the SDH indication clearly visible, but not very sharp. Finally, strategy 5 presented the lowest API, with a reduction of 80% when compared to strategy 4, but at the cost of losing 40% of the CNR. This reduction does not reduce the identification capacity and is due to the introduction of speckle noise from the extra three images in the summation.

Another drawback of using the "brute force" approach of strategy 3 is the required processing time and the amount of data generated. Table 4-4 shows the acquisition and the pre- and post-processing times taken in the experiments of this study. The total time to apply the gTFM using strategy 5 represented only 18% of the time spent in strategy 3. Using 104 probe positions not only requires more time in the acquisition, but also involves a huge computational cost for storing and processing many FMC into TFM images. Therefore, even though some pre-processing is needed to find the best scan plan, the digital twin model is the best option, avoiding the burden of several acquisitions.

Table 4-4 Inspection time from experimental results using different approaches

gTFM (strategy number)	Acquisition time [s]	Pre-processing time [s]	Post-processing time [s]	Total time [s] ([%])
Full range (3)	1560	0	1870	3430 (100.0)
PSOM (4)	105	330	126	561 (16.4)
PSOM+Beamforming (5)	105	330	180	615 (17.9)

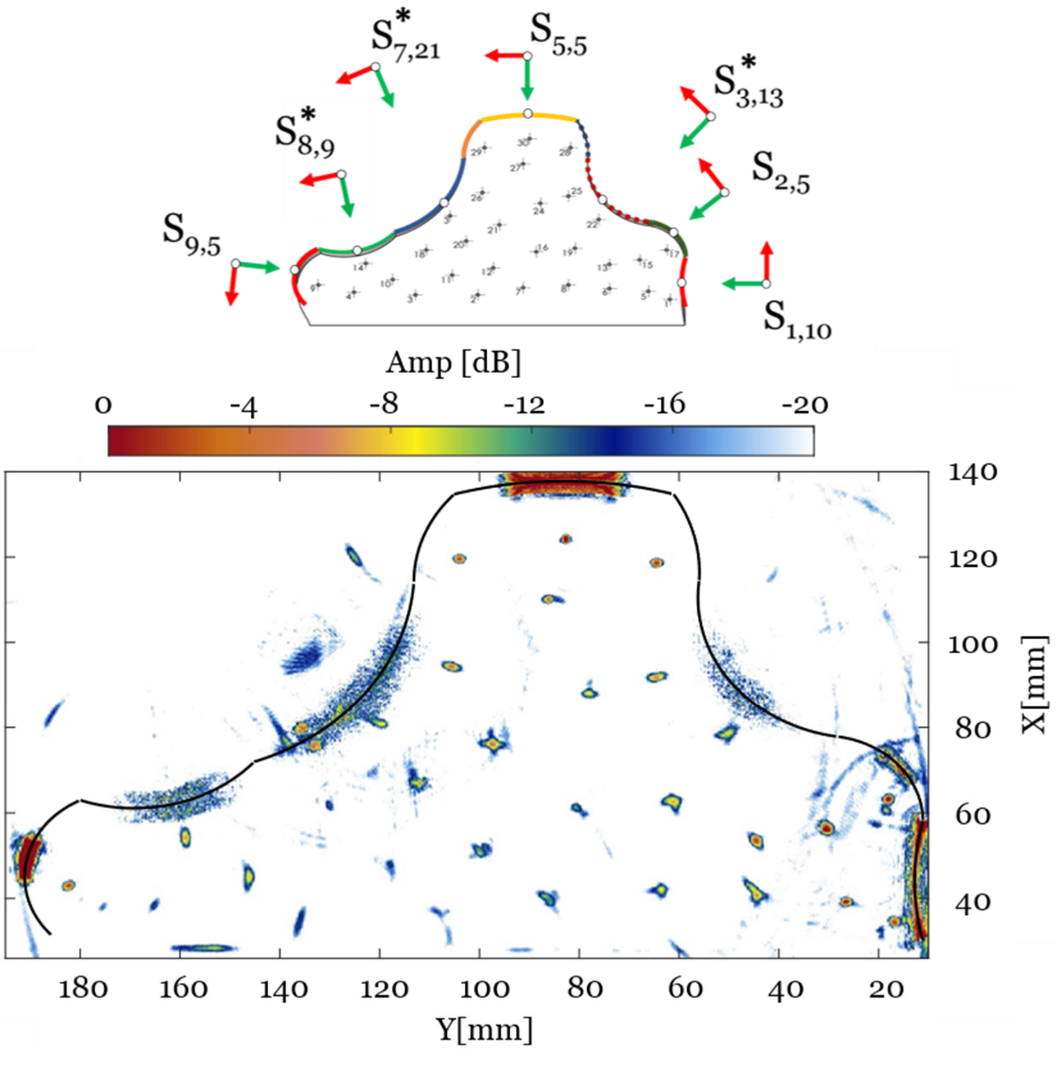

(Strategy 5 – PSOM scan plan with beamforming compensation)

Figure 4-11 gTFM of complex stainless-steel specimen when using a scan plan with optimized standoffs (PSOM) and beamforming strategy in post-processing; schematic of the probe positions used to generate each image in the global summation

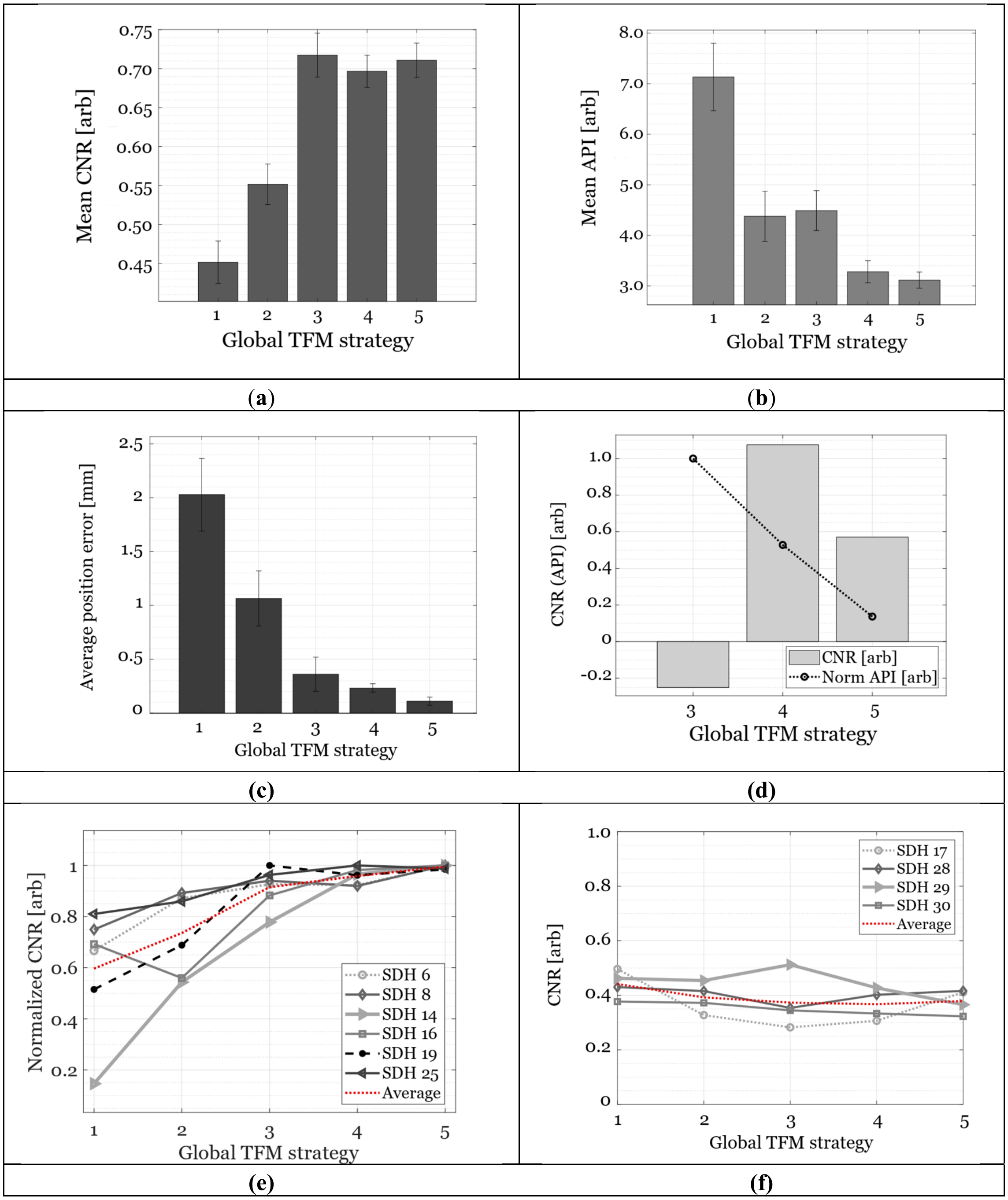

(a) (b)

(c) (d)

(e) (f)

Figure 4-12 Quantitative comparison of gTFM renderings using CNR, API, and position error as metrics. The strategy number is related to the gTFM images of the complex component presented before. **(a)** Mean contrast-to-noise ratio of all SDHs. **(b)** Mean API of all SDHs. **(c)** Average position error of all SDHs. **(d)** Comparison of CNR and API of SDH number 18 for different strategies. **(e)** Mean CNR of SDHs below concave curvatures. **(f)** Mean CNR of SDHs below convex curvatures

Lastly, Figure 4-12 (e) and (f) present the CNR of SDHs below concave and convex curvatures, respectively. This depicts the difference in gTFM performance below each type of curvature for each scan plan. First, in Figure 4-12 (e), there is a clear trend of the influence of the different scan plans on the imaging of SDHs below concave surfaces. By changing the scan plan, the performance was improved, reaching its best value in strategy 5. Meanwhile, Figure 4-12 (f) shows that the imaging of defects below convex surfaces is less influenced by the scan plan. This again points to the need for optimizations in the inspections below concave curvatures, as they represent the greatest challenge for the imaging process.

4.5 Conclusion

Industry 4.0 is quickly advancing towards smart manufacturing, with the entrenchment of robotic automation, digital twin, big data, and AI, all while being environmentally conscious. The present work placed the NDE into this context by demonstrating a gTFM approach that combines digital twin and robotic automation to ultrasonically inspect a mock-up of a critical aerospace component with a complex profile.

Different scan plan strategies were compared, from using no inspection design at all, to using a “brute force” approach, and ultimately, to an optimally designed scan plan. It can be concluded that the scan plan and optimizations greatly affect the gTFM images generated. By using no inspection design, strong reconstruction artifacts may occur, and the inspection is bound to be unreliable, while the optimized gTFM with a designed scan plan showed that it is possible to sharply image SDHs below concave and convex curvatures. A good coverage was achieved efficiently, with only 7 probe positions needed around the specimen. Moreover, the final gTFM image represents an image with easy interpretation as it depicts the complete cross-section, of the specimen with no stitching required.

However, the amplitude and shape of the indications still vary according to the surface profile above them. This means that for application in a real-life scenario, careful calibration is needed along with the gTFM method. Also, slight changes in the speed of sound must be dealt with during image processing, as they may happen in different directions, due to anisotropy and variations in the fluid temperature.

Future work should focus on improving the imaging algorithm, limiting the calculation to pixels inside the specimen and with paths with physical meaning. Also, research should focus on imaging flaws with complex profiles since their imaging would benefit from multidirectional scanning. Moreover, other imaging modes such as plane wave imaging, phase coherence imaging, and the use of other wave modes in reconstruction, should be tested.

4.6 Acknowledgment

This work was supported by the NSERC CREATE oN-DuTy program.

CHAPTER 5

INDUSTRIAL APPLICATION

5.1 Case study – PAUT of aerospace turbine disk forgings

In this chapter, the industrial deliverables of this research project are presented. Here, the results of the PAUT applied to the case study of aerospace turbine disk forgings are presented. By using the methods present in the literature and the novel approaches proposed along in this research, the feasibility study concludes with remarks on the findings and recommendations for the next steps.

5.1.1 Forging characterization

The industrial partner made two specimens available, one is at the pre-machining or sonic stage (5M) and the other has been kept as forged (5F) as shown in Figure 1-1. Also, the corresponding calibration blocks were accessible for this study. The first step was to find the wave propagation velocity and the physical properties of the Ni-alloy of the forged parts. This is important to accurately produce images through post-treatment and for realistic simulations.

First, the shear and longitudinal wave velocities were measured. An Olympus contact probe was used in a pulse-echo setup for the velocity measurement. For the control, a wave generator from Agilent and a Ritec amplifier were used to send and receive the ultrasonic pulse. The ultrasonic pulse transmitted had 5 cycles and was centered at 2.5 MHz. The distance traveled by the wave in the material was equal to a round-trip on a section of 38.05 mm in length. Finally, the velocity of propagation was calculated for the shear and longitudinal wave modes by dividing the traveled distance by the time of flight. Young's modulus and the Poisson coefficient for this material could be calculated by applying the measured velocities to equation 1.1. All these properties are presented in Table 5-1.

Table 5-1 Ni-alloy forged specimens' physical properties

Density [kg/m^3]	8256
Young's modulus [GPa]	222
Poisson ratio	0.3
Shear velocity [m/s]	3216
Longitudinal velocity [m/s]	6018±0.22

Another important characteristic measured from the specimen material was acoustic attenuation. Since the usual frequencies of inspection for this type of part range from 5 to 10 MHz, the attenuation was measured using a broadband probe with a centre frequency of 7.5 MHz. The probe was attached to a calibration block with known dimensions and made of the same Ni-alloy as the disc forgings. For the excitation, a plane wave with 5 cycles was generated and several reflections from the back wall were recorded. Figure 5-1 presents the resulting acoustic attenuation measured. For a central frequency of 7.5 MHz, the approximate value of attenuation is 1.7 dB/cm.

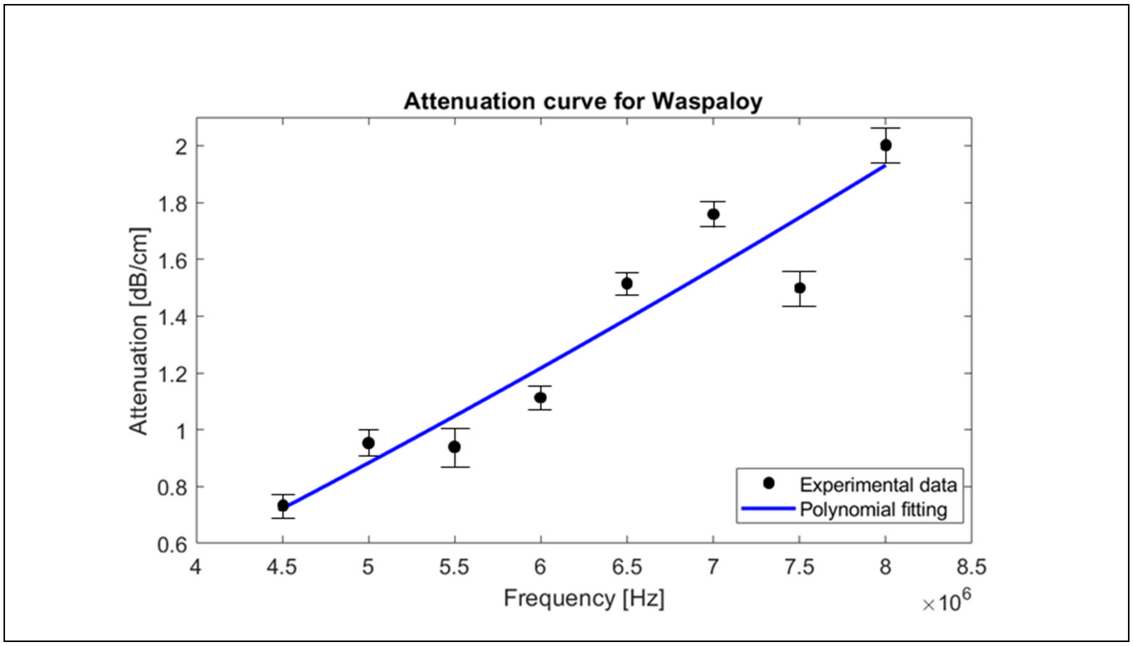

Figure 5-1 Experimental acoustic attenuation of Ni-alloy forged specimens

Finally, a surface roughness measurement was conducted on both the 5M and 5F parts. The objective was to quantify the difference in the surface roughness between the two parts and to apply this property in the simulation models. Figure 5-2 shows the experimental setup, where a Mitutoyo SJ-410 roughness measurement machine is used on the 5F part, along with the results. As expected, the as forged part presented a rougher surface finishing when compared to the machined part. This can be seen in the variations of the surface amplitude of the 5F part, which are up to 5 times higher than the roughness of its machined counterpart. In the latter case, good ultrasound penetration is expected, while the 5F may scatter some of the energy due to these surface irregularities.

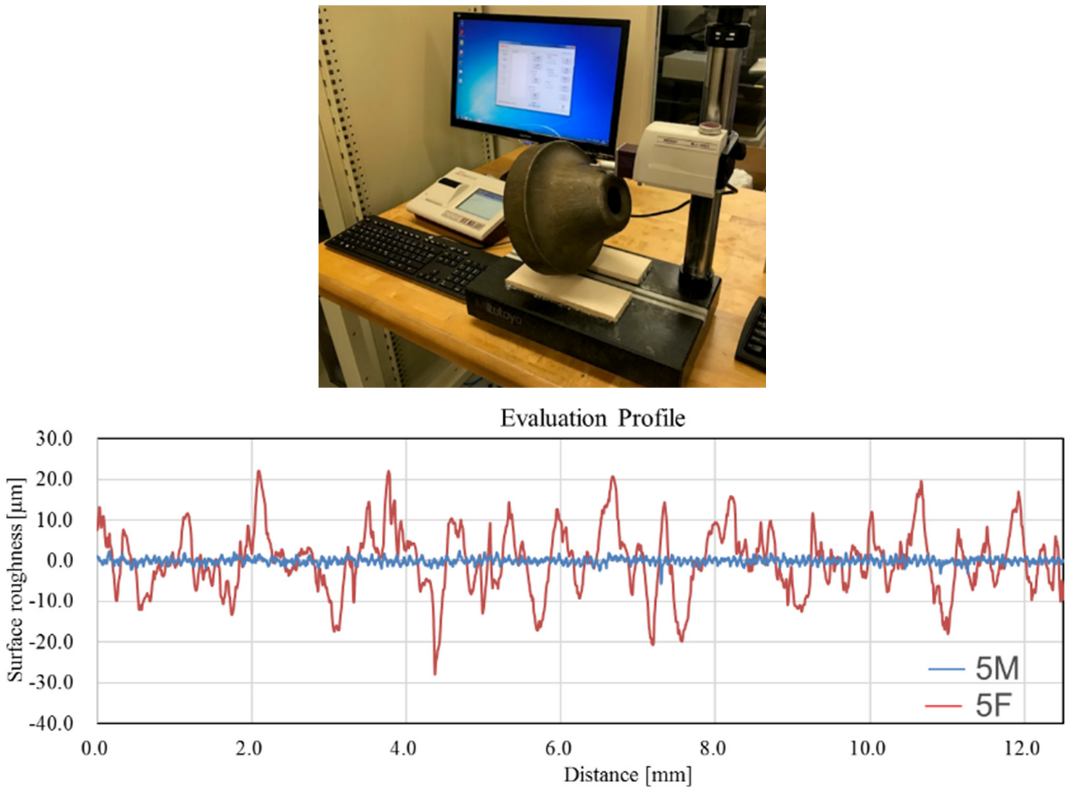

Figure 5-2 Surface roughness measurement and comparison between 5M and 5F forgings

5.1.2 UT and PAUT sensitivity

After characterizing the material properties, it was time to analyze the sensitivity of the ultrasonic inspection. The Ni-alloy presents a uniform microstructure, however, the high acoustic impedance reduces ultrasound penetration. As already mentioned, the standard testing sensitivity is set to a flat bottom hole reflector with 0.79 mm in diameter. Hence, the objective here was to verify the sensitivity to this artificial flaw using both standard UT and PAUT. The standard immersion UT was conducted on P&WC facilities using a 3-axis immersion table and a single-element, with 10 MHz central frequency, and a spherically focused probe connected to an emitter/receiver. As the 5M part is known to be flawless, the experiment focused on the evaluation of the calibration blocks, which dimensions are presented in Table 5-2. The C-Scan image of the set of blocks was constructed and is shown in Figure 5-3. Here, the images of the top-view cross-section of the calibration blocks are plotted. It was possible to analyze the sensitivity at different depths. It could be noted that the 10 MHz focused probe can detect flaws up to the depth of DET 7.

Table 5-2 Geometric parameters of P&WC calibration blocks

Calibration block reference DET [Detail]	A [mm]	B [mm]	C [mm]
1	1.27	5.08	6.35
2	1.905	5.08	6.985
3	2.54	5.08	7.62
4	3.81	5.588	9.398
5	12.7	2.54	15.24
6	25.4	2.54	27.94
7	38.1	2.54	40.64
8	50.8	3.81	54.61
9	63.5	3.81	67.31
10	76.2	3.81	80.01
11	88.9	3.81	92.71
12	101.6	3.81	105.41

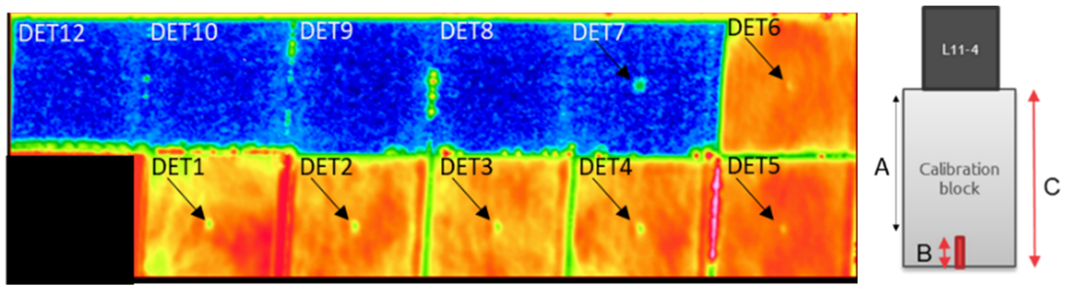

[redacted]

Figure 5-3 C-scan of calibration blocks (Top-view) generated using single-element UT

Afterward, the sensitivity of the UT inspection was analyzed in terms of the probe misalignment. To do so, CIVA® simulations were conducted varying the probe angular position relative to the FBH. And to ensure the reliability of the results, the measured material properties were applied to the model. Figure 5-4 shows the simulation scheme and the results. Here, an important loss of amplitude occurs with the increase of the misalignment angle. On the other hand, the large active aperture of the PAUT probe makes it less sensitive to such angular misalignments.

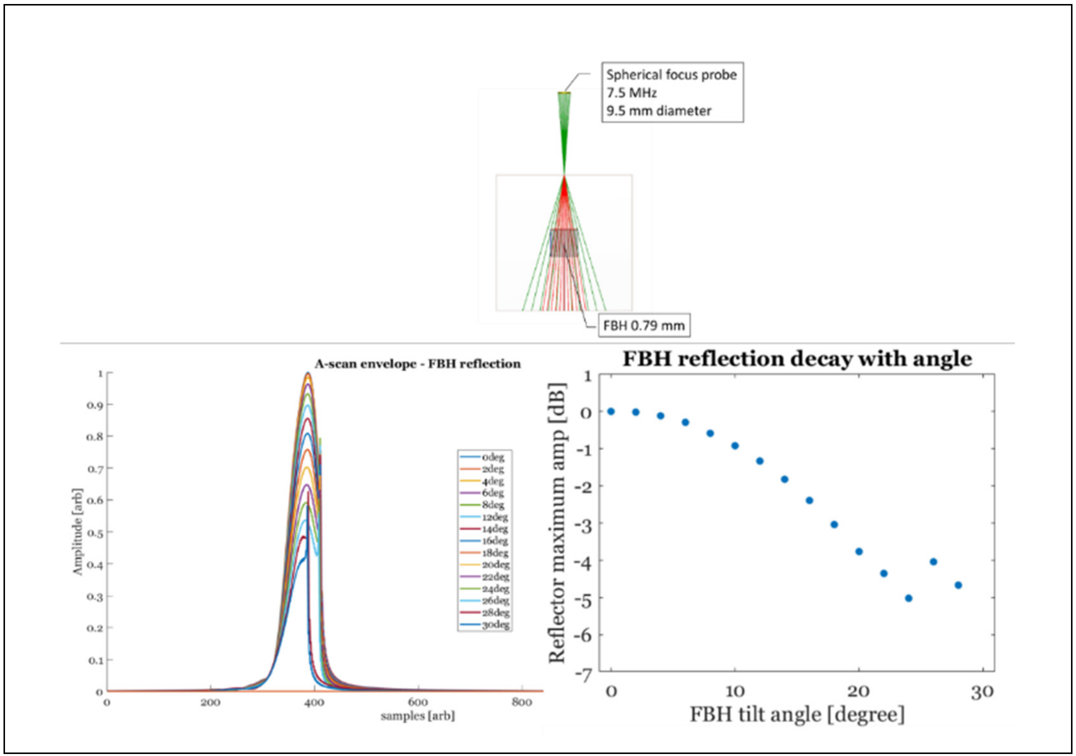

Figure 5-4 Sensitivity of the UT inspection in terms of probe misalignment

Moving forward, the PAUT inspection was also conducted on the blocks. To do so, a Verasonics® Vantage 64LE and the immersion tank available at the PulETS laboratory were used. The phased array probe used was an L11-4v medical probe. This probe has 128 elements, with 0.3mm of pitch, 5 mm elevation, and a central frequency of 6.25MHz. A thin layer of water was used as the coupling medium for the FMC acquisition of each block. Finally, the TFM images were generated considering only the Ni-alloy medium, since the layer of water was negligible, using the probe element coordinates and the longitudinal wave velocity in this medium.

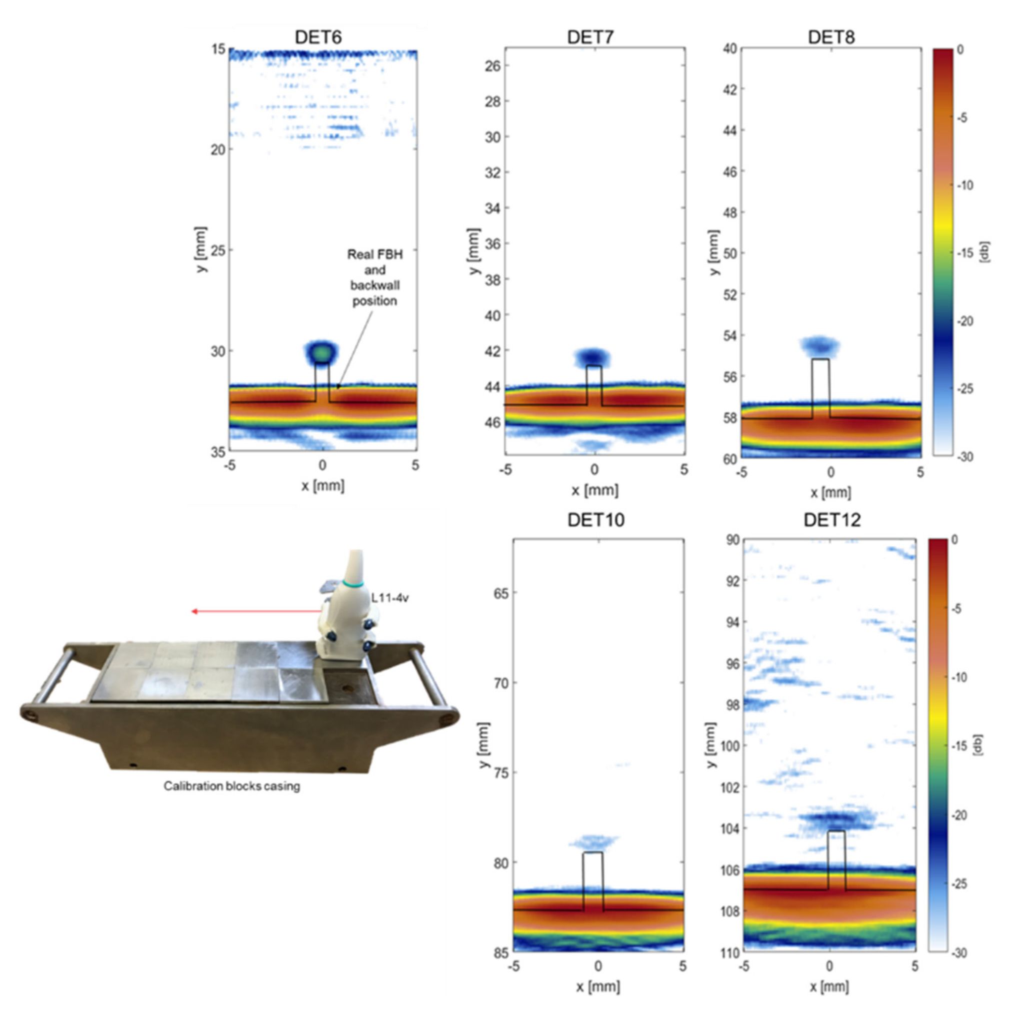

Figure 5-5 TFM reconstruction of calibration blocks (side-view) generated using PAUT

The TFM images of the calibration blocks from DET6 to DET12 are presented in Figure 5-5. Here, the images of the side-view cross-section of the calibration blocks are plotted. The black lines represent the real position of the backwall and FBH on the blocks. The indications of the backwall and the top of the flaws can be seen in the images. In this case, the lower frequency and broader band of the phased array probe allowed the reconstruction of the deepest flaws, positioned up to 104 mm from the probe. These results show that with the TFM, the PAUT could resolve the FBHs in the same manner as the standard UT. Even using a non-focused linear array, instead of a spherically focused probe designed for identification of this type of flaw.

In this context, another type of standard artificial flaw had its sensitivity studied, the side drilled hole (SDH). An equivalency study was conducted to allow the conversion of the sensitivity when this type of flaw was used. The FBH of 0.79 mm had its TFM image sensitivity placed as a benchmark. CIVA® simulations were conducted for SDHs with varying diameters. As a result, Figure 5-6 presents the TFM images for each artificial flaw and the graph showing the relationship between indication amplitude and SDH diameter.

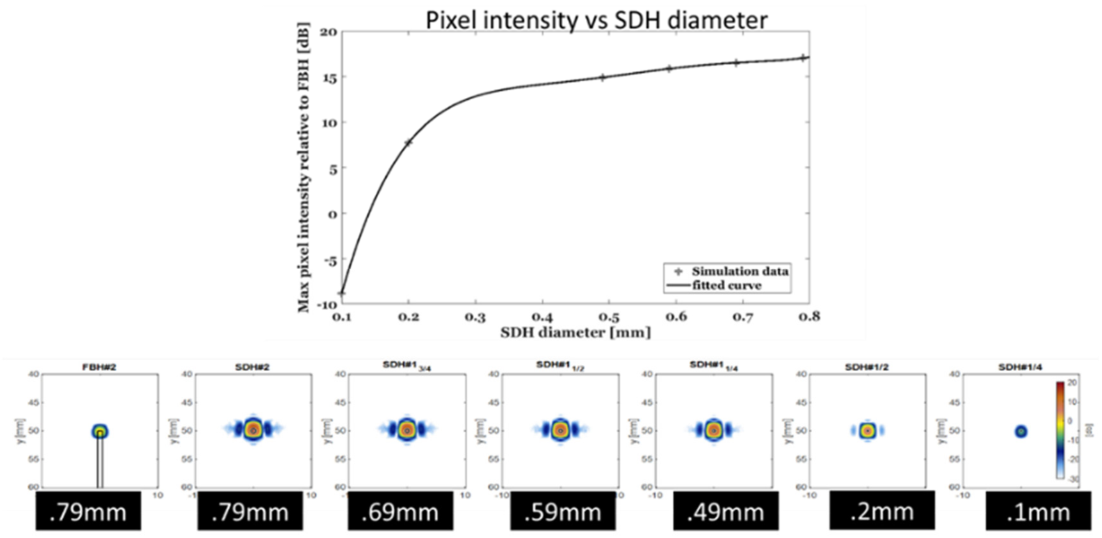

Figure 5-6 Equivalency between FBH with 0.79 mm diameter and SDHs of different diameters

5.1.3 PAUT bore inspection

Based on the geometry of the forgings, a novel approach to their inspection was proposed. A PAUT inspection through the bore of the parts, since the phased array probe, has a small profile and does not require a large standoff, different from the focused single-element probe. As shown in Figure 5-7 and Figure 5-8, FBHs with 0.79 mm diameter were machined in the walls opposite the bore of the 5M and 5F parts. Using a robotic arm TX-90 to control the probe position, several FMC were acquired along the bores of the parts using a Verasonics® Vantage 64LE. An Olympus probe 5L64I with 64 elements and 5MHz of central frequency was used in water immersion. After all acquisitions, the TFM images were post-processed and stitched into a single image using the superposition of equal pixels.

As can be seen in Figure 5-7, the front-wall indication from the bore is visible as well as the back wall from the outer diameter of the forging. Moreover, the indications of the FBHs can be observed, and as expected, with varying amplitude according to the depth. The double indication is due to the presence of a larger diameter hole in the base of each FBH.

In the same manner, Figure 5-8 presents the TFM image rendered from the 5F forging. Again, the indications of the FBHs are visible. However, not all are clear, because of their deeper position in the 5F which has a larger outer diameter. This is not a problem since these flaws are already beyond the expected depth limit for this inspection. Also, the smaller radius of the bore in the 5M does not allow for a water layer large enough to avoid the front-wall second reflection. This can be easily mitigated by an increase of the bore radius in manufacturing or the use of a probe in contact with the bore. In conclusion, it has been shown that the bore PAUT inspection can increase the sensitivity and probability of detection on these forgings, as it introduces an extra direction of incidence to the scan plan.

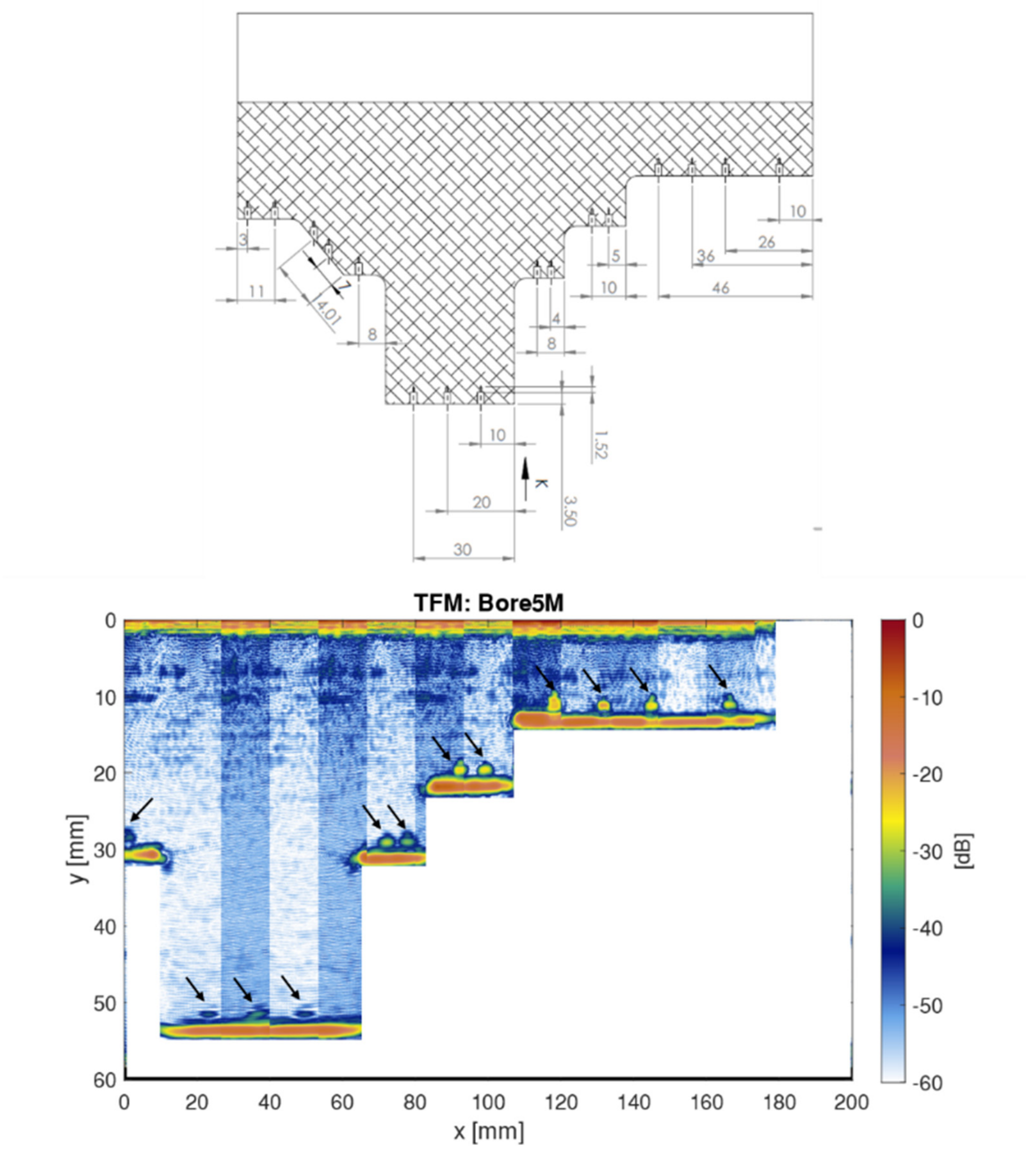

Figure 5-7 5M forging bore inspection design and resulting experimental TFM image

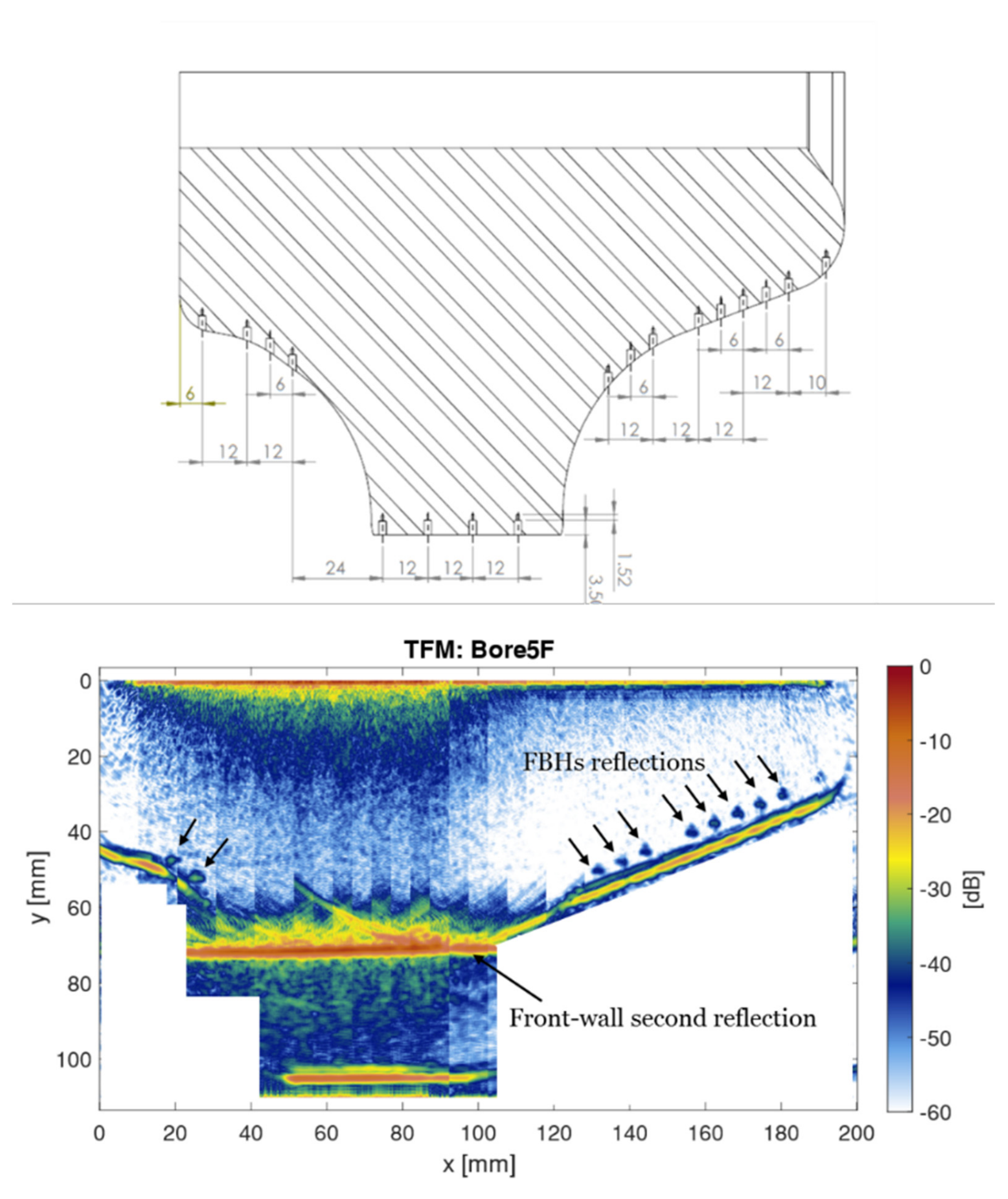

Figure 5-8 5F forging bore inspection design and resulting experimental TFM image

5.1.4 Real flaw evaluation

Another important step in the industrial application was the evaluation of the PAUT on the inspection of a real flaw. In a rare situation, P&WC identified the presence of an anomaly in a

5M part during its regular UT inspection. To better analyze this anomaly, a cube was extracted from the forging, as shown in Figure 5-9. In the same schematic, the PAUT inspection setup using an Olympus probe with 32 elements and 10MHz of central frequency is also shown. Again, the acquisition was done with a Verasonics® Vantage 64LE, and several FMC were acquired on different faces of the 5M cube. These acquisitions were done in a range of positions, between steps with 1mm separation, to allow a 3D reconstruction of the flaw.

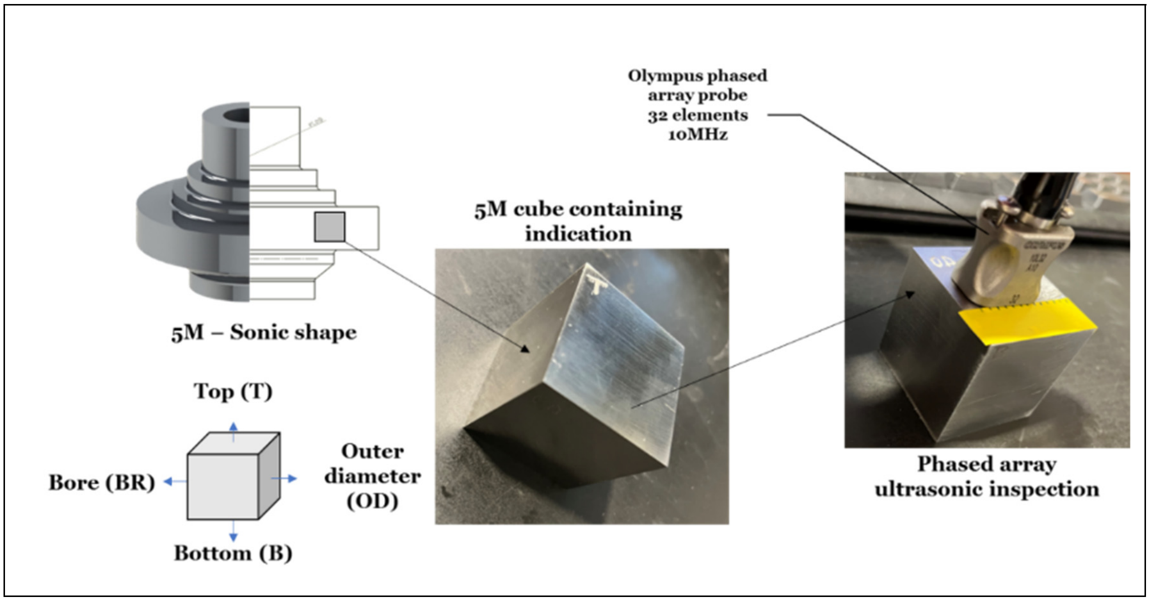
Olympus phased array probe 32 elements 10MHz
5M cube containing indication
5M – Sonic shape
Top (T)
Bore (BR)
Outer diameter (OD)
Bottom (B)
Phased array ultrasonic inspection
T

Figure 5-9 Schematic of real flaw inspection - 5M region with anomaly extraction – PAUT of the 5M cube

The first step in the 5M cube PAUT was the defect sizing calibration. For this purpose, a calibration block with FBH was imaged using TFM, and the flaw was sized through the 6dB drop method, as presented in Figure 5-10. Here, the 6dB drop measured the indication with 88% of size overestimation. Thus, this factor was also applied to the measurements of the real flaw.

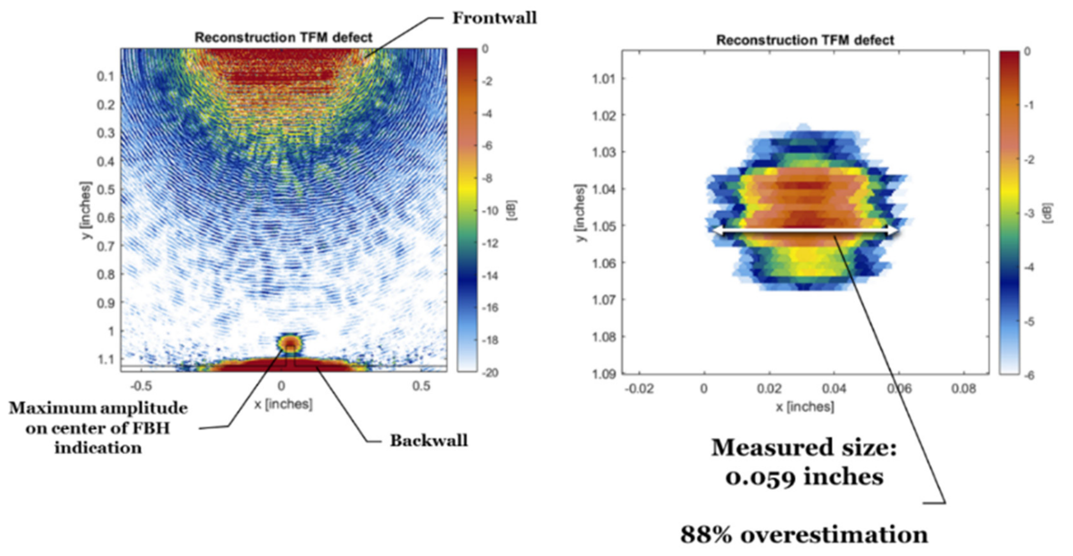

Figure 5-10 TFM image of calibration block for sizing error estimation

Afterward, the TFM images of the 5M cube were generated and stitched into a 3D rendering. Figure 5-11 and Figure 5-12 respectively show the renderings from acquisitions done on the outer diameter (OD) surface and the top surface (T) of the cube. These iso-surface images show all the voxels with amplitude up to 6dB below the amplitude of the calibration reflector.

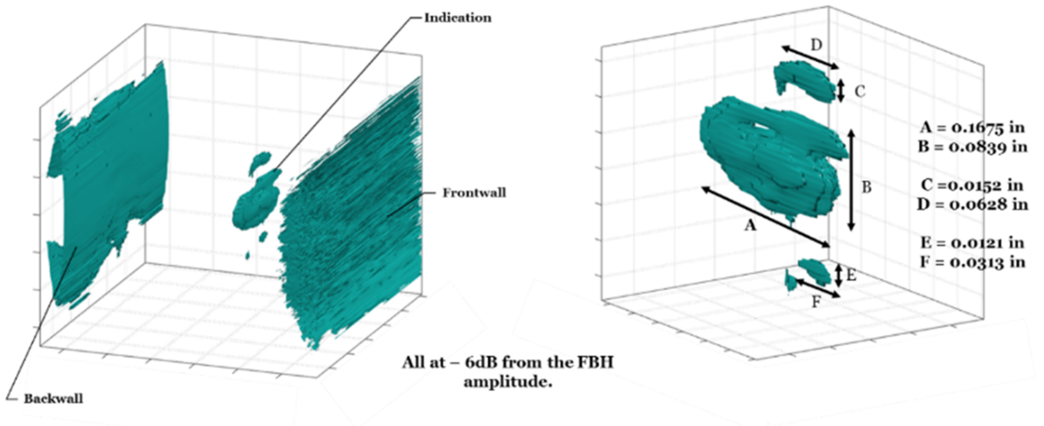
Indication
Frontwall
Backwall
All at – 6dB from the FBH amplitude.
D
C
B
A
E
F
A = 0.1675 in
B = 0.0839 in
C =0.0152 in
D = 0.0628 in
E = 0.0121 in
F = 0.0313 in

Figure 5-11 3D TFM rendering of the real flaw acquired through PAUT on the OD surface

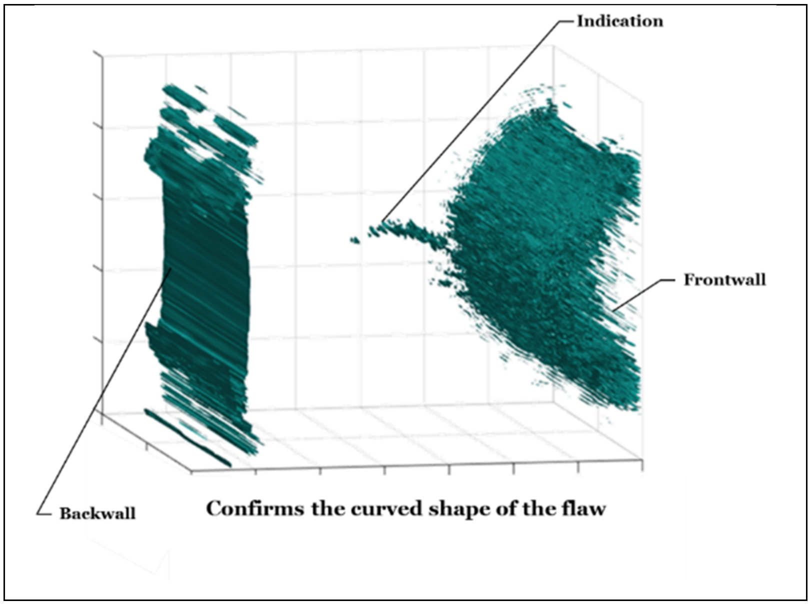

Figure 5-12 3D rendering of the real flaw acquired through PAUT on the T surface

The indications on the 3D renderings in Figure 5-11 and Figure 5-12 show that there is a region of planar discontinuities present in the cube. The high amplitude, comparable to the calibration reflector, points out a planar crack with a void section. It is important to note that in these images the specular reflections in the flaws' faces contribute the most to the image formation. Thus, it's only possible to infer an approximate sizing. Also, the thickness shown in the image is only related to the length of the ultrasonic pulse applied. With this, the dimensions from A to F are measured as shown in Figure 5-11. Finally, the acquisition from the top face was analyzed to confirm that the flaw is indeed a planar crack. This can be seen in the thin and curved shape of the indication shown by the image in Figure 5-12.

For comparison, the other two non-destructive evaluation modalities were conducted on the 5M cube. One was the CT scan image of the flaw, shown in Figure 5-13. In this case, the flaw can be identified as a thin line in the images, but with poor contrast. This is due to the nature of the Ni-alloy that does not allow good penetration of the x-rays, even in the small depth of the cube. The second NDE was the classic UT, presented in Figure 5-14. In this C-scan, the indication of the flaw can be seen clearer than in the CT scan, but not with a resolution as high as the one obtained with the PAUT.

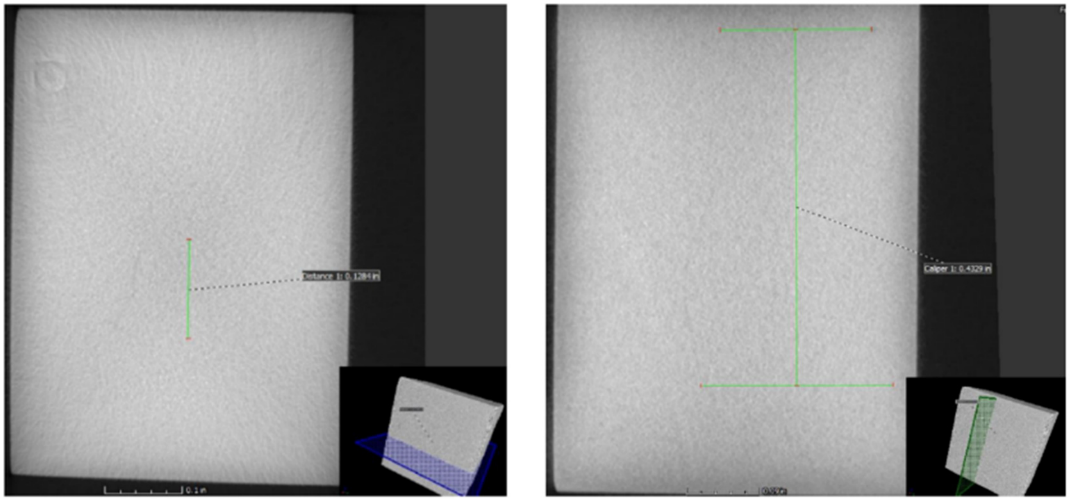
Distance 1: 0.1284 in
0.1 in
Caliper 1: 0.4329 in

(a) (b)

Figure 5-13 (a) CT scan image of the top surface showing the indication length of 0.1284 inches. (b) CT scan image of the outer diameter surface showing the indication height of 0.4329 inches

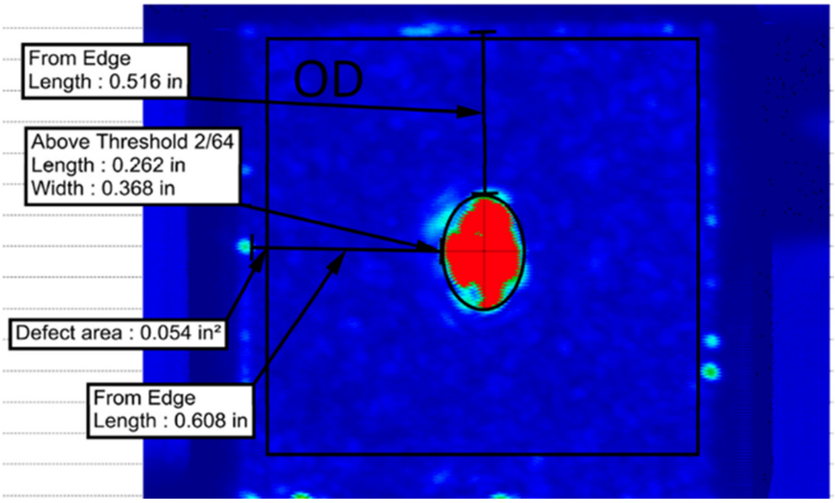

Figure 5-14 Classic UT C-scan of the outer diameter surface showing an indication with 0.262 inches in length and 0.368 inches in width

Now, to verify the precision and reliability of the NDE, destructive testing was conducted. As shown in Figure 5-15, twenty polishing steps of 0.01 inches were done to reveal the crack throughout using micrography. Also, the micrographs obtained in steps 1 and 20 are highlighted in Figure 5-15. The micrography reveals that the NDE assessment was correct, and a crack is indeed present in the specimen. The forging process caused this lack of fusion in the microstructure of the material. For brevity, only two micrographs are presented here, but through all the steps the crack appeared. Thus, it can be said that the crack was indeed planar and that the PAUT image created a faithful representation of the flaw. This is also true for the sizing capabilities, as the PAUT had the closest estimation of the size of all three methods. The error in dimension D is only 9% and in dimension, A is only 6%.

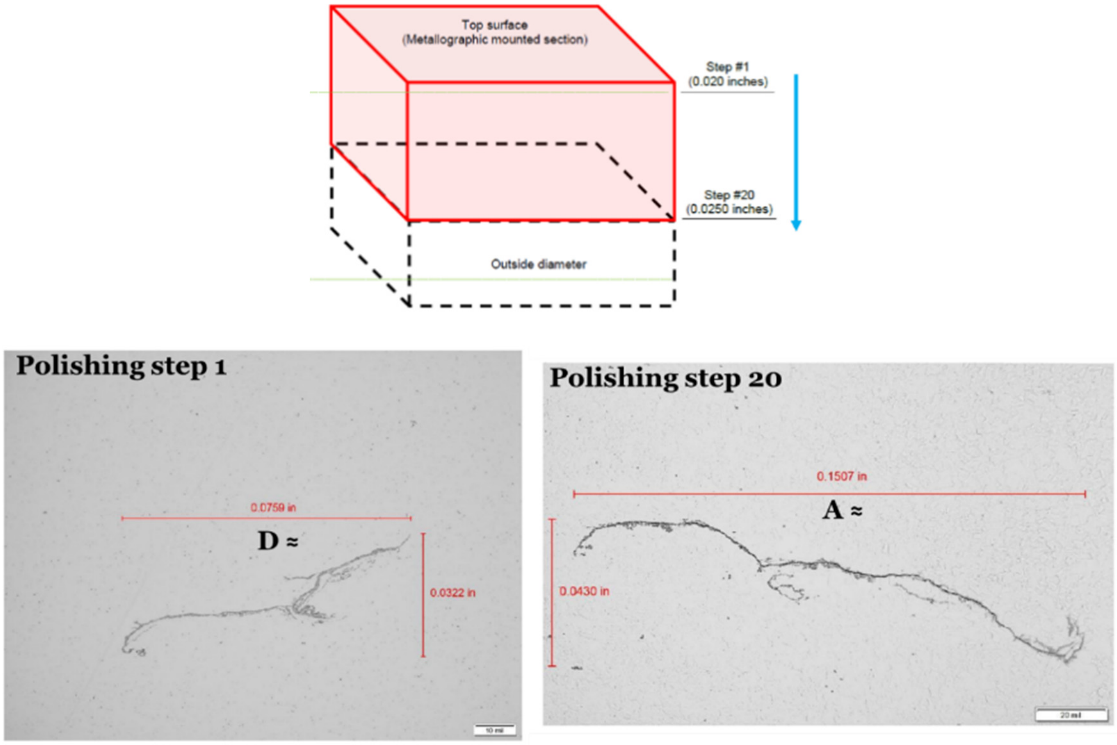
Top surface
(Metallographic mounted section)
Step #1
(0.020 inches)
Step #20
(0.0250 inches)
Outside diameter
Polishing step 1
0.0759 in
D ≈
0.0322 in
10 mil
Polishing step 20
0.1507 in
A ≈
0.0430 in
20 mil

Figure 5-15 Destructive testing of the 5M cube.
Polishing steps and micrography of the crack

5.1.5 Final feasibility experiment

Finally, this research project reached the maturity to propose a final feasibility experiment. As all the results showed so far, the PAUT, allied with the methods proposed by this research, could generate reliable images of flaws inside complex specimens. As shown in Figure 5-16, the proof-of-concept was validated by the imaging of the forging mock-up. By using a gTFM with an optimized scan plan plus a bore inspection, all the internal flaws could be correctly identified through the indications in the image. This gives a prediction that the performance on the actual forging will be similar or even better since the mock-up has a more complicated profile.

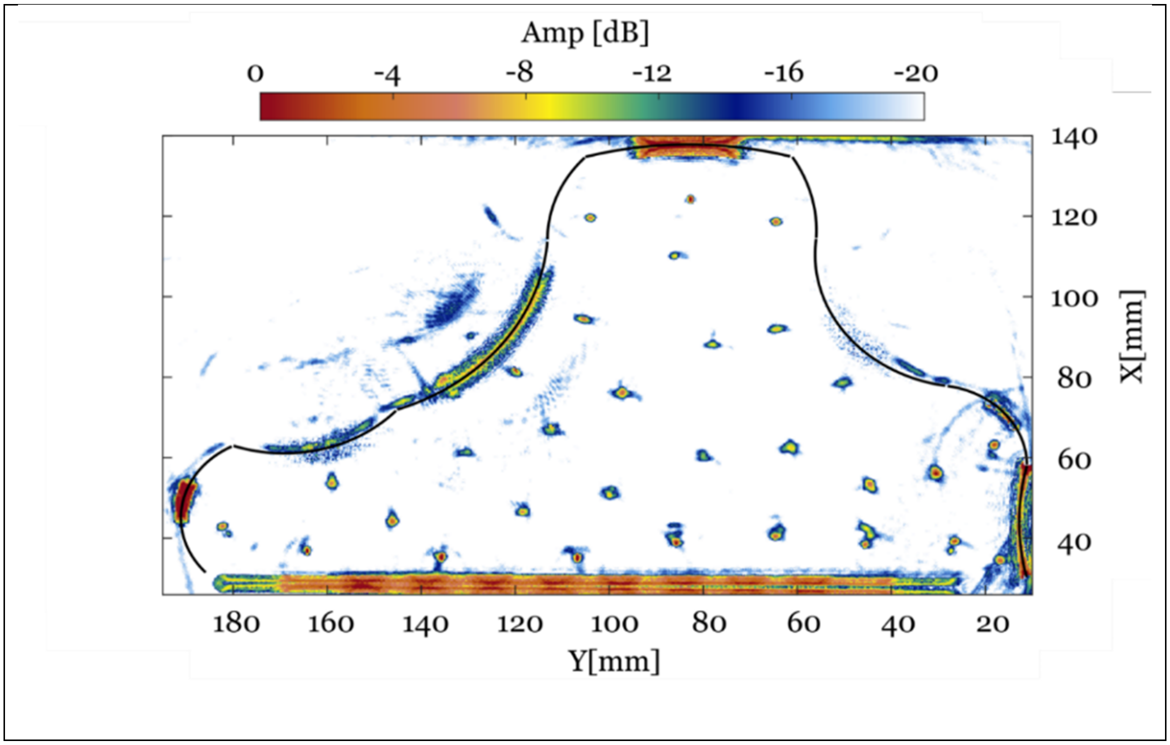

Figure 5-16 Proof-of-concept for as-forged inspection. gTFM image of the 5F forging mock-up

Thus, the last step is the analysis of the actual 5M and 5F forgings. So, a final feasibility experiment was designed for P&WC. The development started with a CIVA® simulation of the 5F model. This simulation was done to verify the sensitivity of the gTFM with a constant probe standoff on the actual forging. And, from the results select the points of interest, or where to place the defects on the real parts. Figure 5-17 presents the image of the 5F cross-section generated through the gTFM of the simulations. As expected, artifacts are present due to the non-optimization of the probe standoff. Apart from that, all indications of the defects were visible, which shows the good sensitivity of the inspection. And even more impressive, inspecting the part around all its profile generated images similar to a flat specimen. Where there is not much variation of amplitude between the indications. This must be because the profile has only two curved regions.

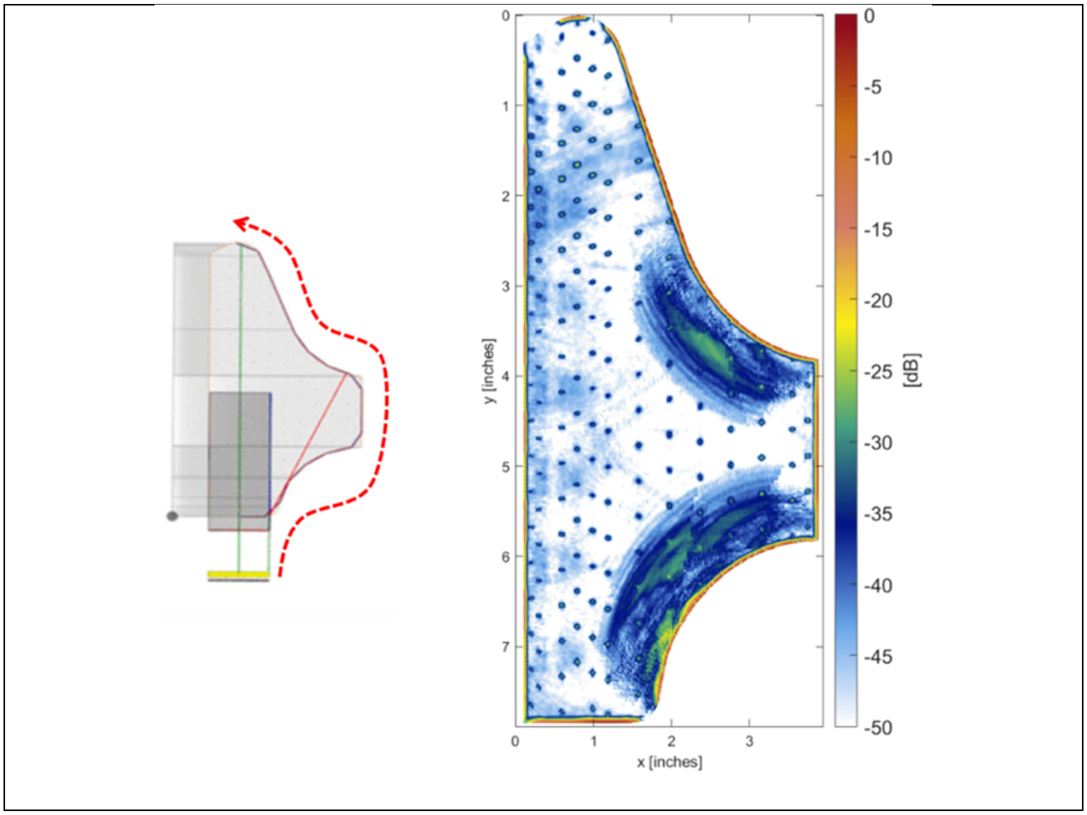

Figure 5-17 gTFM on 5F forging. Image generated from the data acquired in a CIVA® simulation

Thus, a different approach in the selection of the flaw locations was used. In this approach, the 5M was used as the reference for positioning. Having imagined that the 5M was encapsulated inside of the 5F, as shown in Figure 5-18, allowed for the design of the comparative study. First, the flaws were distributed to fill the 5M section, and then the 5M was positioned inside the 5F, so all the flaws would have an equal position. After that, the 5M and 5F parts were divided into two sections each. The idea is that in one section the overall sensitivity can be tested. So, several side-drilled holes of 1 mm in diameter were distributed along the cross-section. On the other hand, the remaining section can be used to verify the capabilities of the PAUT for resolving complex flaws. For this reason, angled notches, flat bottom holes, and a cluster of holes were introduced into the design. Finally, manufacturing these specimens will allow P&WC to directly compare the sensitivity of the UT of the 5M versus the PAUT of the 5F.

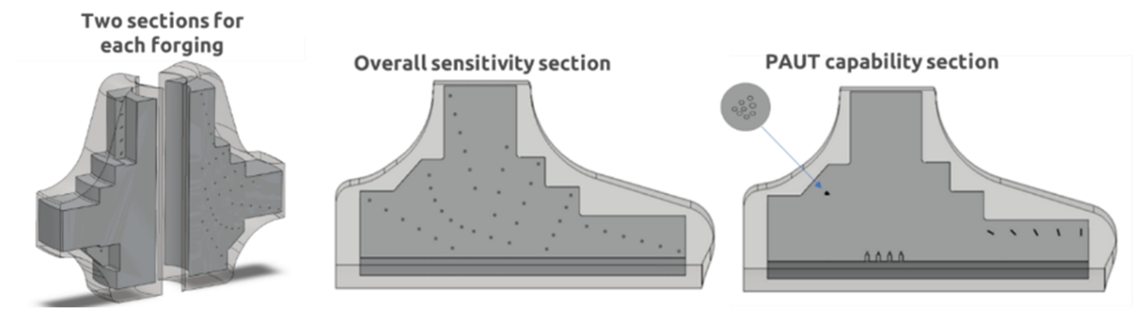
Two sections for each forging
Overall sensitivity section
PAUT capability section

Figure 5-18 Schematic of the 5M and 5F specimen preparation for the final feasibility experiment.

CONCLUSION

This work evaluated the PAUT capabilities applied to specimens with complex geometries in the context of the inspection of aerospace disk forgings. With three complementary novel research articles, this work not only contributed to the state-of-the-art in the imaging of subsurface flaws in engineering components with curved surface profiles. But also answered a demand from the aerospace industry on the possibility of improvement of a critical process. The big question was: is it feasible to inspect as-forged components to avoid the sonic machining step? While trying to answer this question, important findings were achieved in the field of PAUT of complex components, which can be summarized as:

- Strong reconstruction artifacts occur at certain combinations of probe standoff and surface profile.
- The performance of the phased array immersion inspection of curved parts can be optimized based on the probe standoff, using an optimization method (PSOM).
- A beamforming strategy can be applied to improve ultrasound transmission through concave surfaces, yielding a better TFM quality.
- A global TFM approach that combines digital twin and robotic automation can be used to PAUT complex components, rendering a cross-section image that correctly depicts all internal features.
- For the inspection of complex parts, the scan plan must be designed, as the image quality is greatly dependent on probe position and the surface's radius of curvature.

These conclusions came through the developed experimental studies. In the first, the TFM imaging of defects inside concave and convex sinusoidal parts was evaluated. FMC acquisitions were done at different standoffs and the results were compared with the developed PSOM algorithm. Then the PSOM capacity was verified through the good agreement of the predictions and the resulting TFM images. Nevertheless, it was noted that the ultrasound penetration was still reduced with certain surface profiles, and the image quality was reduced accordingly. In the second study, the FMC obtained from the concave specimens of the first study was used in the development of a beamforming strategy for ultrasound transmission optimization. When comparing the TFM images obtained with and without the beamforming, an improvement of up to 11 dB in SNR was observed. Even when using only 12 transmissions the TFM after the beamforming still surpassed the image quality of the non-optimized approach. Lastly, the third study combined both previous approaches in a contextualized study regarding the PAUT of an aerospace forging mock-up. A global TFM approach was proposed, combining digital twin and robotic automation to ensure the best PAUT imaging quality. From the comparison of different scan plans, it was observed that optimizations greatly affect the gTFM images generated. Strong reconstruction artifacts were observed when using poor scan plans, rendering unreliable inspection images. However, when the optimized gTFM was used, sharp images of the SDHs below concave and convex curvatures were generated, with good coverage and efficiently using only 7 probe positions.

In parallel to that, these PAUT approaches were applied to the case study of P&WC. Through simulations and experiments, the PAUT bore inspection was proposed and tested, appearing as a strong alternative to increase the sensitivity and probability of detection of the forgings' inspection. Moreover, as a proof of concept for the feasibility study, the gTFM was applied to the forging mock-up in combination with the bore inspection. The resulting image correctly revealed all the internal flaws through high contrast indications. This gives a prediction that the 5F inspection will have an even better performance, as its profile is simpler than the one from the mock-up. Hence, it can be concluded that the PAUT of the 5F forging is feasible using the developed methods, as they are a strong suit for the reliable inspection of complex specimens. However, it is still important to understand and evaluate the differences in sensitivity between the standard 5M inspection and a novel 5F inspection, so a new calibration standard is created. So, this project finally proposed an experimental design that allows P&WC to directly compare the sensitivity of the UT of the 5M versus the PAUT of the 5F.

Lastly, it can be said that the broad introduction of the PAUT into the aerospace industry is not only necessary but also inevitable. As was shown by the evaluation of a real flaw in the 5M forging, the PAUT surpassed the CT scanning and the classical UT in terms of performance.

The error in sizing was minimal and the representation of the flaw was much clearer when using the TFM algorithm. Hence, it can be said that such a gain in sensitivity and ease of interpretation of the results cannot be overlooked by the industry.

RECOMMENDATIONS

Follow-up research of this study must focus on some aspects observed during the project. For example, the amplitude and shape of the indications coming from the flaws varied according to the surface profile, meaning that calibration tools must be investigated. Also, different flaw shapes and compositions, such as inclusions, must have their imaging sensitivity evaluated. In terms of the PSOM, more surface profiles, composed of combinations of concave and convex, or sharp edges should be tested to verify the limits of the algorithm.

Furthermore, the slight changes in the speed of sound between different directions of wave incidence proved to be a point of attention in the application of the gTFM. Therefore, the development of automated methods capable of correcting these wave velocity variations, only based on the data or image, can be an interesting subject of research. More on the improvement of the gTFM, the focus should be put on limiting the calculation to pixels that contribute to the image of the specimen's cross-section. Finally, compressive sensing and sparse arrays should be investigated as an option to reduce the amount of data and processing required by the gTFM inspection of complex parts.

LIST OF BIBLIOGRAPHICAL REFERENCES

Brown, R. H., Dobson, J., Pierce, S. G., Dutton, B., & Collison, I. (2017). Quantifying performance of ultrasonic immersion inspection using phased arrays for curvilinear disc forgings. Dans *AIP Conference Proceedings* (Vol. 1806, pp. 040004). AIP Publishing LLC.

Camacho, J., Atehortua, D., Cruza, J. F., Brizuela, J., & Ealo, J. (2018). Ultrasonic crack evaluation by phase coherence processing and TFM and its application to online monitoring in fatigue tests. *NDT & E International, 93*, 164-174. doi: https://doi.org/10.1016/j.ndteint.2017.10.007. Repéré à https://www.sciencedirect.com/science/article/pii/S0963869516303073

Chabot, A., Laroche, N., Carcreff, E., Rauch, M., & Hascoët, J. Y. (2020). Towards defect monitoring for metallic additive manufacturing components using phased array ultrasonic testing. *Journal of Intelligent Manufacturing, 31*(5), 1191-1201. doi: 10.1007/s10845-019-01505-9. Repéré à https://doi.org/10.1007/s10845-019-01505-9

Chatillon, S., Cattiaux, G., Serre, M., & Roy, O. (2000). Ultrasonic non-destructive testing of pieces of complex geometry with a flexible phased array transducer. *Ultrasonics, 38*(1), 131-134. doi: https://doi.org/10.1016/S0041-624X(99)00181-X. Repéré à http://www.sciencedirect.com/science/article/pii/S0041624X9900181X

Cheeke, J. D. N. (2012). Fundamentals and Applications of Ultrasonic Waves. *CRC Press., (2nd ed.)*. doi: https://doi.org/10.1201/b12260

Chiao, R. Y., & Thomas, L. J. (1994). Analytic evaluation of sampled aperture ultrasonic imaging techniques for NDE. *IEEE Transactions on Ultrasonics, Ferroelectrics, and Frequency Control, 41*(4), 484-493. doi: 10.1109/58.294109

Cruza, J. F., Camacho, J., Mateos, R., & Fritsch, C. (2019). A new beamforming method and hardware architecture for real time two way dynamic depth focusing. *Ultrasonics, 99*, 105965. doi: https://doi.org/10.1016/j.ultras.2019.105965. Repéré à http://www.sciencedirect.com/science/article/pii/S0041624X18306516

Drinkwater, B. W., & Wilcox, P. D. (2006). Ultrasonic arrays for non-destructive evaluation: A review. *NDT & E International, 39*(7), 525-541. doi: https://doi.org/10.1016/j.ndteint.2006.03.006. Repéré à https://www.sciencedirect.com/science/article/pii/S0963869506000272

Holmes, C., Drinkwater, B. W., & Wilcox, P. D. (2005). Post-processing of the full matrix of ultrasonic transmit–receive array data for non-destructive evaluation. *NDT & E International, 38*(8), 701-711.

Honarvar, F., & Varvani-Farahani, A. (2020). A review of ultrasonic testing applications in additive manufacturing: Defect evaluation, material characterization, and process control. *Ultrasonics, 108*, 106227. doi: https://doi.org/10.1016/j.ultras.2020.106227. Repéré à http://www.sciencedirect.com/science/article/pii/S0041624X20301669

Hopkins, D., Brassard, M., Neau, G., Noiret, J.-N., Johnson, W., & Le Ber, L. (2013). Surface-Adaptive Ultrasound (SAUL) for phased-array inspection of composite specimens with curved edges and complex geometry. Dans *AIP Conference Proceedings* (Vol. 1511, pp. 809-816). American Institute of Physics.

Howard, P., Klaassen, R., Kurkcu, N., Barshinger, J., Chalek, C., Nieters, E., . . . deFromont, F. (2007). Phased array ultrasonic inspection of titanium forgings. Dans *AIP Conference Proceedings* (Vol. 894, pp. 854-861). American Institute of Physics.

Hoyle, E., Sutcliffe, M., Charlton, P., & Rees, J. (2018). Virtual source aperture imaging with auto-focusing of unknown complex geometry through dual layered media. *NDT & E International, 98*, 55-62. doi: https://doi.org/10.1016/j.ndteint.2018.04.005. Repéré à https://www.sciencedirect.com/science/article/pii/S0963869517306874

Hunter, A. J., Drinkwater, B. W., & Wilcox, P. D. (2010). Autofocusing ultrasonic imagery for non-destructive testing and evaluation of specimens with complicated geometries. *NDT & E International, 43*(2), 78-85.

Ilovitsh, A., Ilovitsh, T., & Ferrara, K. W. (2019). Multiplexed ultrasound beam summation for side lobe reduction. *Scientific Reports, 9*(1), 13961. doi: 10.1038/s41598-019-50317-7. Repéré à https://doi.org/10.1038/s41598-019-50317-7

Kerr, W., Pierce, S. G., & Rowe, P. (2016). Investigation of synthetic aperture methods in ultrasound surface imaging using elementary surface types. *Ultrasonics, 72*, 165-176. doi: https://doi.org/10.1016/j.ultras.2016.08.007. Repéré à https://www.sciencedirect.com/science/article/pii/S0041624X16301408

Lane, C. J. (2014). The inspection of curved components using flexible ultrasonic arrays and shape sensing fibres. *Case Studies in Nondestructive Testing and Evaluation, 1*, 13-18.

Le Jeune, L., Robert, S., Lopez Villaverde, E., & Prada, C. (2016). Plane Wave Imaging for ultrasonic non-destructive testing: Generalization to multimodal imaging. *Ultrasonics, 64*, 128-138. doi: 10.1016/j.ultras.2015.08.008

Le Jeune, L., Robert, S., & Prada, C. (2016). Plane wave imaging for ultrasonic inspection of irregular structures with high frame rates. Dans *AIP Conference Proceedings* (Vol. 1706, pp. 020010). AIP Publishing LLC.

Lingvall, F., Olofsson, T., & Stepinski, T. (2003). Synthetic aperture imaging using sources with finite aperture: deconvolution of the spatial impulse response. *J Acoust Soc Am, 114*(1), 225-234. doi: 10.1121/1.1575746

Long, R., Russell, J., & Cawley, P. (2012). Ultrasonic phased array inspection using full matrix capture. *Insight-Non-Destructive Testing and Condition Monitoring, 54*(7), 380-385.

Mahaut, S., Roy, O., Beroni, C., & Rotter, B. (2002). Development of phased array techniques to improve characterization of defect located in a component of complex geometry. *Ultrasonics, 40*(1), 165-169. doi: https://doi.org/10.1016/S0041-624X(02)00131-2. Repéré à http://www.sciencedirect.com/science/article/pii/S0041624X02001312

Malkin, R. E., Franklin, A. C., Bevan, R. L. T., Kikura, H., & Drinkwater, B. W. (2018). Surface reconstruction accuracy using ultrasonic arrays: Application to non-destructive testing. *NDT & E International, 96*, 26-34. doi: https://doi.org/10.1016/j.ndteint.2018.03.004. Repéré à http://www.sciencedirect.com/science/article/pii/S0963869517306941

Mansur Rodrigues Filho, J. F., & Bélanger, P. (2021). Probe Standoff Optimization Method for Phased Array Ultrasonic TFM Imaging of Curved Parts. *Sensors, 21*(19). doi: 10.3390/s21196665

Mansur Rodrigues Filho, J. F., & Bélanger, P. (2022). A Beamforming Strategy to Improve the Ultrasonic Phased Array Inspection Below Concave Surfaces. *Canadian Institute For Non-Destructive Evaluation (CINDE) Journal, 43*(1), 10-13.

Margetan, F. J., Umbach, J., Roberts, R., Friedl, J., Degtyar, A., Keller, M., Hassan, W., Brasche, L., Klassen A., Wasan, H., and Kinney, A. (2007). INSPECTION DEVELOPMENT FOR TITANIUM FORGINGS. *U.S. Department of Transportation Federal Aviation Administration (FAA),* (DOT/FAA/AR-05/46). doi: This document is available to the U.S. public through the National Technical Information Service (NTIS), Springfield, VA 22161.

Matuda, M. Y., Buiochi, F., & Adamowski, J. C. (2019). Experimental analysis of surface detection methods for two-medium imaging with a linear ultrasonic array. *Ultrasonics, 94*, 50-59. doi: https://doi.org/10.1016/j.ultras.2018.12.004. Repéré à http://www.sciencedirect.com/science/article/pii/S0041624X18305766

McKee, J. G., Bevan, R. L. T., Wilcox, P. D., & Malkin, R. E. (2020). Volumetric imaging through a doubly-curved surface using a 2D phased array. *NDT & E International, 113*, 102260. doi: https://doi.org/10.1016/j.ndteint.2020.102260. Repéré à https://www.sciencedirect.com/science/article/pii/S0963869519302488

McNab, A., & Stumpf, I. (1986). Monolithic phased array for the transmission of ultrasound in NDT ultrasonics. *Ultrasonics, 24*, 148-155.

Mei, Y., Jin, H., Yu, B., Wu, E., & Yang, K. (2021). Visual geometry Group-UNet: Deep learning ultrasonic image reconstruction for curved parts. *J Acoust Soc Am, 149*(5), 2997-3009. doi: 10.1121/10.0004827. Repéré à https://doi.org/10.1121/10.0004827

Mei, Y. J., Jin, H. R., Yu, B., Wu, E. Y., Li, L. Q., & Yang, K. J. (2021). Robot-Assisted Track-Scan Imaging Approach with Multiple Incident Angles for Complexly Structured Parts. *Journal of Testing and Evaluation, 49*(1), 675-689. doi: 10.1520/Jte20190908. Repéré à <Go to ISI>://WOS:000599154100043

Olympus, N. (2004). Introduction to phased array ultrasonic technology applications. *D Tech Guideline", Olympus NDT.*

Oralkan, O., Ergun, A. S., Johnson, J. A., Karaman, M., Demirci, U., Kaviani, K., . . . Khuri-Yakub, B. T. (2002). Capacitive micromachined ultrasonic transducers: next-generation arrays for acoustic imaging? *IEEE Transactions on Ultrasonics, Ferroelectrics, and Frequency Control, 49*(11), 1596-1610. doi: 10.1109/TUFFC.2002.1049742

Patterson, M. S., & Foster, F. S. (1983). The Improvement and Quantitative Assessment of B-Mode Images Produced by an Annular Array/Cone Hybrid. *Ultrasonic Imaging, 5*(3), 195-213. doi: 10.1177/016173468300500301. Repéré à https://doi.org/10.1177/016173468300500301

Pompei, F. J., & Wooh, S.-C. (2002). Phased array element shapes for suppressing grating lobes. *J Acoust Soc Am, 111*(5), 2040-2048. doi: 10.1121/1.1460924. Repéré à https://asa.scitation.org/doi/abs/10.1121/1.1460924

Rachev, R. K., Wilcox, P. D., Velichko, A., & McAughey, K. L. (2020). Plane Wave Imaging Techniques for Immersion Testing of Components With Nonplanar Surfaces. *IEEE Transactions on Ultrasonics, Ferroelectrics, and Frequency Control, 67*(7), 1303-1316. doi: 10.1109/TUFFC.2020.2969083

Robert, S., Calmon, P., Calvo, M., Jeune, L. L., & Iakovleva, E. (2015). Surface estimation methods with phased-arrays for adaptive ultrasonic imaging in complex components. *AIP Conference Proceedings, 1650*(1), 1657-1666. doi: 10.1063/1.4914787. Repéré à https://aip.scitation.org/doi/abs/10.1063/1.4914787

Robert, S., Casula, O., Roy, O., & Neau, G. (2013). Real-time nondestructive testing of composite aeronautical structures with a self-adaptive ultrasonic technique. *Measurement Science and Technology, 24*(7), 074011.

Russell, J., Long, R., & Cawley, P. (2010). Development of a membrane coupled conformable phased array inspection capability. Dans *AIP Conference Proceedings* (Vol. 1211, pp. 831-838). American Institute of Physics.

Schmerr, L. (2015). *Fundamentals of Ultrasonic Phased Arrays* (Vol. 215). doi: 10.1007/978-3-319-07272-2

Simonetti, F., & Fox, M. (2019). Experimental methods for ultrasonic testing of complex-shaped parts encased in ice. *NDT & E International, 103*, 1-11. doi: https://doi.org/10.1016/j.ndteint.2019.01.008. Repéré à http://www.sciencedirect.com/science/article/pii/S0963869518306376

Sutcliffe, M., Weston, M., Charlton, P., Donne, K., Wright, B., & Cooper, I. (2013). Full matrix capture with time-efficient auto-focusing of unknown geometry through dual-layered media. *Insight - Non-Destructive Testing and Condition Monitoring, 55*(6), 297-301. doi: 10.1784/insi.2012.55.6.297. Repéré à https://www.ingentaconnect.com/content/bindt/insight/2013/00000055/00000006/art00004
https://doi.org/10.1784/insi.2012.55.6.297

Sutcliffe, M., Weston, M., Dutton, B., Cooper, I., & Donne, K. (2012). Real-time full matrix capture with auto-focusing of known geometry through dual layered media. Dans *Proceedings of the NDT 2012 Conference in British Institute of Nondestructive Testing*.

Zhang, J., Drinkwater, B. W., & Wilcox, P. D. (2014). Efficient immersion imaging of components with nonplanar surfaces. *IEEE Transactions on Ultrasonics, Ferroelectrics, and Frequency Control, 61*(8), 1284-1295.

Zimermann, R., Mohseni, E., Lines, D., Vithanage, R. K. W., MacLeod, C. N., Pierce, S. G., . . . Ding, J. (2021). Multi-layer ultrasonic imaging of as-built Wire + Arc Additive Manufactured components. *Additive Manufacturing, 48*, 102398. doi: https://doi.org/10.1016/j.addma.2021.102398. Repéré à https://www.sciencedirect.com/science/article/pii/S2214860421005510